

NNT : 2017SACL022

THESE DE DOCTORAT
DE
L'UNIVERSITE PARIS-SACLAY
PREPAREE A
"CENTRALE-SUPELEC"

ECOLE DOCTORALE N° 579
Sciences mécanique et énergétiques, matériaux et géosciences

Spécialité de doctorat : Génie des procédés

Par

Mme Huan DU

Observation et modélisation de la croissance de *Postia placenta* :
de l'échelle discrète de la colonie à l'échelle macroscopique

Thèse présentée et soutenue à Châtenay-Malabry, le 28 mars 2017 :

Composition du Jury :

M. COURNÈDE Paul-Henry	Professeur, CentraleSupélec	Président
M. TURNER Ian	Professeur, QUT, Australie	Rapporteur
M. ROUGER Frédéric	Directeur de recherche, FCBA	Rapporteur
M. DUCHIRON Francis	Professeur, URCA	Examinateur
M. DUMONT Yves	Directeur de recherche, CIRAD AMAP	Examinateur
M. BESSERER Arnaud	Maître de conférences, Université de Lorraine	Invité
M. PERRÉ Patrick	Professeur, CentraleSupélec	Directeur de thèse
M. AYOZ Méhdi	Maître de conférences, CentraleSupélec	Co-encadrant de thèse
M. LV Pin	Ingénieur-recherche, CentraleSupélec	Co-encadrant de thèse

Remerciement

Tout d'abord je voudrais remercier l'ensemble des membres du jury. Je voudrais remercier Ian Turner et Frédéric Rouger d'avoir accepté de relire cette thèse et d'en avoir été rapporteurs. Je tiens à remercier Paul-Henry Cournède d'avoir accepté d'être président du jury. Je remercie également tous les autres membres du jury, Francis Duchiron, Yves Dumont et Arnaud Besserer, d'avoir accepté d'assister à la présentation de ce travail. Je voudrais tout particulièrement remercier Arnaud Besserer qui nous a proposé la souche de champignons et nous a appris la méthode de culture pour ce travail.

Je tiens à exprimer mes plus vifs remerciements à Patrick Perré qui fut pour moi un directeur de thèse attentif. Je lui suis reconnaissante de m'avoir aiguillée dans la recherche et de m'avoir fait bénéficier tout au long de ce travail de ses nombreuses compétences, de son efficacité et de sa rigueur intellectuelle. Ils ont été et resteront des moteurs de mon travail de chercheur. J'ai été extrêmement sensible à ses qualités humaines, d'écoute et de compréhension. En particulier, je le remercie de sa patience pendant mes efforts d'expression et de compréhension de la langue française. Enfin, ses nombreuses relectures et corrections de cette thèse ont été très appréciables. Pour tout cela merci.

Je remercie aussi Mehdi Ayouz et Pin Lv, mes deux co-encadrants, de m'avoir beaucoup aidée pendant ma thèse sur la modélisation et l'expérimentation et d'avoir consacré beaucoup de temps pour discuter et améliorer les détails de ce travail, notamment en début de thèse.

Je remercie Cyril Breton d'avoir consacré du temps pour m'apprendre à me servir du fluorochrome et du microscope confocal à balayage laser qui ont beaucoup servi à la partie d'expérimentation dans ce travail.

Je remercie également Jean Trubuil et Thierry Martin d'avoir fabriqué les boîtes de culture

pour l'expérimentation.

Je remercie tous les collègues du laboratoire LGPM pour la bonne ambiance de travail et également pour les nombreux bons moments passés ensemble lors des pauses café. Grâce à eux, je trouve que c'est agréable de travailler et de vivre en France. Entre autres Magali, Marietta, Angéla, Arnaud, Aude, Mathilde, Catherine...

Je remercie tous mes amis chinois pour m'avoir accompagnée pendant la vie en France, pour avoir été présents pour moi et pour les nombreux bons moments où nous avons fêté les fêtes ensemble. Entre autres Zeyin, Wangshu, Meng, Jing, Wenjing...

Je tiens à remercier China Scholarship Council (CSC) de m'avoir proposée une bourse qui m'a permis de suivre mes études en France.

Enfin, les mots les plus simples étant les plus forts, j'adresse toute mon affection à ma famille, et en particulier à mes parents qui m'ont toujours supportée et été derrière moi.

*à mes parents,
et à tous ceux que je ne nomme pas, mais qui se reconnaîtront.*

Table des matières

List of symbols	11
List of abbreviation	15
1 Introduction	17
1.1 Background	17
1.2 Objective and strategy	18
1.3 Outline	20
2 Literature review	23
2.1 Wood	24
2.1.1 Wood structure and composition	24
2.1.2 Wood material	25
2.2 Wood decay fungi	27
2.2.1 Morphology	27
2.2.2 Physiology	28
2.2.3 Wood decay types	30
2.3 Visualization of mycelial growth using CLSM	31
2.3.1 Principle of CLSM	32
2.3.2 Fluorescent dyes	34
2.3.3 Imaging capabilities	35
2.3.4 Application of CLSM	35
2.4 Mathematical modeling of fungal growth	37
2.4.1 Colony-scale models	39
2.4.1.1 Discrete models	39
2.4.1.2 Continuous models	44
2.4.2 Macroscale models	46
2.4.3 Conclusion	50

3	Experimental observation of the growth of <i>Postia placenta</i>	53
3.1	Introduction	54
3.2	Materials and methods	56
3.2.1	Materials	56
3.2.2	Methods	56
3.2.2.1	Inoculation and culture	56
3.2.2.2	Fluorescence staining	57
3.2.2.3	Confocal observation	57
3.2.2.4	Measurement and analysis	58
3.3	Results and discussion	61
3.4	Conclusion	70
3.5	Supporting Information	73
4	Discrete model of mycelial growth in complex environment	79
4.1	Introduction	80
4.2	Fungal growth behaviors	82
4.3	Implementation of growth rules into lattice	85
4.3.1	Hyphal elongation	85
4.3.2	Branching	89
4.3.3	Anastomosis	90
4.3.4	Tropism and obstacle	90
4.3.5	Simulation	91
4.4	Calibration from growth observation	92
4.4.1	Initial field	92
4.4.2	Parameter defined directly from experimental observation	93
4.4.3	Parameters determined by inverse analysis	94
4.4.4	Validation on macroscopic profiles	97
4.5	Potential in complex environment	100
4.5.1	Obstacles in mycelial growth environment	100
4.5.2	Other complex environments	101
4.6	Conclusion	102
4.7	Supporting Information	104
5	Continuous model of the fungal growth in porous media	107
5.1	Introduction	108
5.2	Identification of the continuous model based on the discrete model	110
5.2.1	Radial biomass density calculated from the discrete model	110

5.2.2	Continuous model at the local scale	111
5.2.3	Determination of D and S	113
5.3	2D simulation of fungal growth using the continuous model	114
5.3.1	Comparison of fungal growth in various media	114
5.3.2	Simulation of fungal growth in extended domains	117
5.4	Deriving the macroscale model	120
5.4.1	Spatial averaging of the local fields	120
5.4.2	Identification of the macroscale model	122
5.5	Conclusion	123
6	Conclusion and perspectives	127

List of symbols

Normal symbols

B	Local-scale normalized biomass density (Continuous variable)
c_s	Coefficient of thigmotropism intensity
C	Criterion
D	Local-scale diffusion coefficient
\bar{D}_h	Average diameter of hyphae
D_l, γ, γ'	Parameters governing local-scale diffusion coefficient
D_m, γ_m, γ'_m	Parameters governing macroscale diffusion coefficient
i	Tip number
k	Variable index
k_{active}	Proportion of active tips
k_{lag}	Ratio of emerged branch numbers per hypha during the lag phase to that during the exponential phase
l	Length
P	Probability
P_{active}	Probability of activation
P_{dir}	Probability of the occurrence of a small directional change of tips
r	Radius
R	Rate

s	Offset length
S	Local-scale source term
t	Time
x, y, z	Coordinates
w	Width
\vec{n}	Vector
\vec{S}	Thigmotropism
\vec{T}	Unidirectional tropism
\vec{T}_{tot}	Total tropism
δ	Grid/lattice spacing
ϵ	Porosity
ϵ_l	Projection error of the measured branching length
ϵ_θ	Projection error of the measured branching angle
θ	Angle
λ, κ, κ'	Parameters governing local-scale source term
$\lambda_m, \kappa_m, \kappa'_m$	Parameters governing macroscale source term
ρ	Radial density of fungal biomass
τ	Time stepping
ν	Coefficient of hyphal reaction rate to tropisms
ϕ	Column density of fungal biomass
φ_{br}	New emerged branch number per hypha
ω	Random number
Ω	Domain
$\partial\Omega$	Boundary/Interface of domain Ω

Superscripts

a	Apical
l	Lateral
x	Along x direction
y	Along y direction

Subscripts

a	Relating to anastomosis
ap	Relating to active tips
ad	Relating to apical dominance
b	Relating to branches
g	Relating to the projection of a vector on the tangent plane
h	Relating to hyphae
i, j	Variable indices
n	Relating to the unit vector normal to a surface
$occupy$	Occupation of a node in the lattice
p	Relating to tips
r	Real
α	Relating to the pore phase
β	Relating to the solid phase

Operators and functions

$1_A(\omega)$	Indicator function which has the value 1 if $\omega \in A$
f	Probability density function (PDF)
F	Weighted cumulative distribution function
F_Γ	Corrected gamma cumulative distribution

$g_s(\mu, \sigma)$	PDF of Gaussian distribution with parameters μ (mean) and σ (standard deviation)
$g_\gamma(\alpha, \beta)$	PDF of gamma distribution with the scale parameter (α) and rate parameter (β)
N, n	Number of
Δ	Interval/Difference of
$\langle \rangle$	Average of/Macroscale
$\lfloor \rfloor$	Floor function mapping the real number to the largest previous integer
$\ \ $	Euclidean norm of

List of abbreviation

1D, 2D, 3D	One-, two- and three-dimensional
AB, LB	Apical, lateral branch
BC	Boundary condition
CA	Cellular automata
CLSM	Confocal laser scanning microscopy
LOC	Local lateral branching mechanism
MES	Mean squared error
MIP	Maximum intensity projection
ML	Middle lamella
NA	Network automata
OSB	Oriented strand board
PMT	Photomultiplier tube
<i>pts</i>	Points
PW	Primary wall
R1, R2, R3	Region 1, 2, 3
RD	Reaction-diffusion
RH	Relative humidity

RSS	Residual sum of squares
S1, S2, S3	Outer, middle, inner layer of the secondary wall
WML	Wood mass loss

Chapter1

Introduction

1.1 Background

Wood has been an important construction material utilized in the building and shipbuilding industries for many centuries, due to its excellent mechanical properties, such as hardness, lightness and sustainability. Nowadays, wood and wood-based products are still commonly used and the opportunities for the materials to gain market share is likely to increase. Indeed, they offer excellent solutions for the new trends in building designs : the requirements for good thermal performance and the use of renewable materials, resulting in a low carbon footprint in the life cycle of buildings [1, 2]. Because of the good thermal performance as well as the simple manufacturing processes, the energy consumption is reduced not only in the construction stage but also in the use stage. However, as a bio-based material, wood is easily degraded by organisms, such as insects [3], fungi [4], and bacteria [5]. Among these organisms, fungi are the primary cause of the wood decomposition, as they are very efficient in activating decay mechanisms and capable of surviving in complex environments owing to the highly-branched networks. They can also develop protective mechanisms against adverse conditions, like the generation of chlamydospore. In the forest ecosystems, wood decay fungi play an essential role in degradation of organic matter and cycling of the nutrient elements, and therefore it is critical in the global carbon balance. On the other hand, the fungal decay in lumber structures is of major concern in relation to the building service life as well as to human safety. They degrade the main supporting components, such as cellulose and lignin, and hence increase the chance of mechanical failure. Fig. 1.1 shows some examples of fungal decay on wood in buildings. Every year an enormous amount of wood and wood-based products, including those in storage as well as in service, are destroyed by fungal decay. Especially, throughout Eu-

Europe and North America, the brown rot fungi are the most common and destructive within buildings due to their rapid wood decay mechanisms [4].



FIGURE 1.1 – Examples of fungal decay on wood in buildings [6, 7].

Whether to protect wood against bio-degradation or to predict the service life of lumber structures, it is fundamental to investigate the fungal growth mechanisms. A great amount of research has been performed on fungal morphogenesis, decay mechanisms, impact of environmental factors, etc. Recently, great attention was paid to mathematical modeling. Such modeling tools are likely to supplement costly and tedious experimental studies and are absolutely required for service life to be accounted from the design stage. Mathematical modeling has played a significant part in expanding the understanding of the growth and function of the fungal mycelium. For example, the capacity of simulating and predicting the fungal growth in different conditions provides an efficient tool to understand fungal morphology in different conditions, to protect wood against biotic factors and to predict the service life of lumber structures.

1.2 Objective and strategy

This thesis proposes an original upscaling strategy to derive an efficient tool for modeling fungal decay in wood-based materials. As reported by [8], the aim of mathematical mode-

ling is to reduce a complex biology system to a simpler mathematical description which can be used to investigate and identify the key characteristics of complex biological phenomena. To simplify the biological system into a formulation of reasonable complexity, it is essential to determine what has to be included and what can be omitted, which depends on the specific biological issues to be addressed. In our work, we are interested in the morphology and the distribution of hyphal density as a function of time. Therefore, the main growth mechanisms should be included and the growth parameters should be calibrated. Thus, an experimental observation was performed to determine and quantify these parameters. All these steps allowed a discrete model to be imagined, which is able to generate the mycelial network and was precisely validated by experimental observation. Finally, a continuous model was derived to perform the transition of modeling fungal growth in porous media from the local scale (free-growth conditions) to the macro-scale (equivalent medium of a locally heterogeneous medium).

As mentioned above, this work uses experimental microscopic observations to propose a modeling of fungal growth at three successive scales : i) discrete mycelial network in homogeneous media at the colony scale, ii) continuous mycelial growth in free-growth conditions and iii) continuous fungal growth in porous media at the macro-scale. The detailed strategy of this work is shown in Fig. 1.2, while Table 1.1 proposes some representative images along with this modeling strategy. In this work, the complexity of modeling gradually shifts from an explicit description of growth mechanisms in the discrete model to an implicit account of these mechanisms, but inside a complex geometry for the continuous model. Since it is essential to establish an approach to model the simplest case of mycelial growth to explore its basic growth characteristics, we focused on the growth of a single strain of mycelium in a homogeneous environment. *Postia placenta* was selected as the fungus of interest according to the European standards (CEN/TS15083-1 [9]). It is one of the most common brown rot fungi found in wood that is currently in service [10, 11, 12]. The genome of this species was sequenced and its secretome was analyzed [13]. Furthermore, the decay mechanisms and the impact of environmental factors on its growth rate have been also studied [14, 15, 16]. However, there are no publications reporting the visualization of mycelial structures and quantitative measurement of the growth characteristics of *Postia placenta*. Thus, a laboratory experimental study of the growth of *Postia placenta* was conducted as a basis for experimental inputs of our modeling work. The temporal evolution of a colony on an agar medium was observed using confocal laser scanning microscopy (CLSM). The growth parameters and statistical properties quantified in the observation were used to calibrate and validate our discrete model, the second

step of the work, the structuring step of our modeling approach. A lattice-based approach was chosen in this discrete model which incorporated the main growth behaviors of mycelia observed in the experiment as well as those described in the literature. The validated model was able to reproduce the intricate coupling between spatial invasion and network densification. In addition, this model also has the potential to account for different environmental factors by embedding tropisms and/or by modifying the growth statistics, such as elongation and branching. The third step consists in deriving a continuous model for simulating the fungal growth in a porous medium. Two successive upscaling steps were included : i) to derive an equivalent continuous formulation from the radial biomass density simulated by the discrete model and ii) to derive an equivalent macroscale model by inverse analysis of the averaged fields simulated at the local scale of the heterogeneous medium.

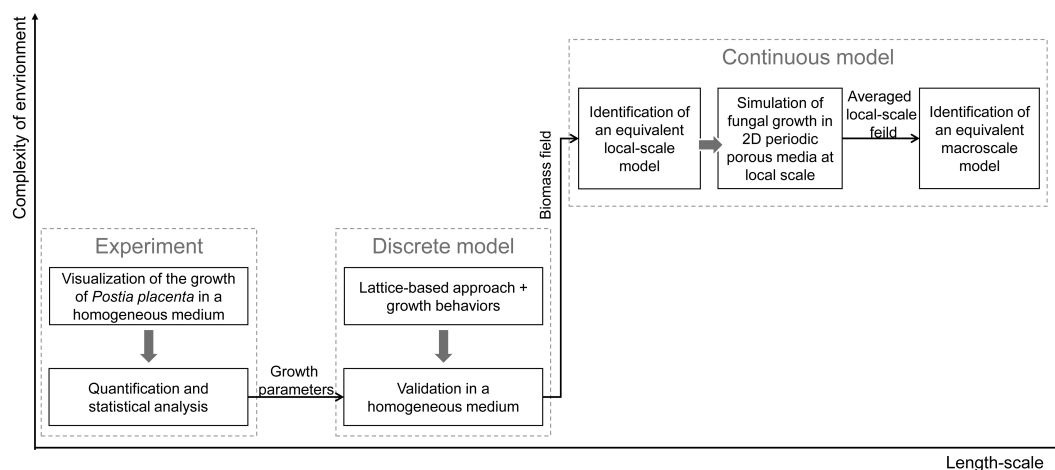


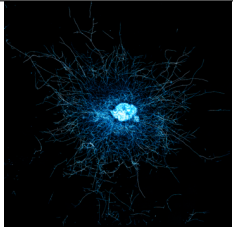
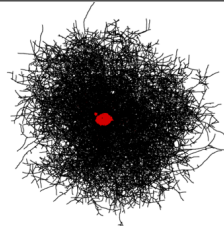
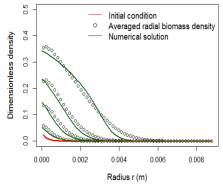
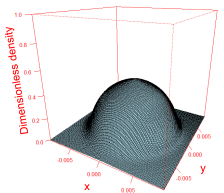

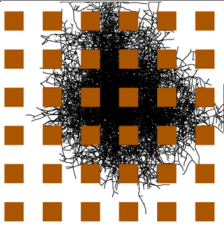

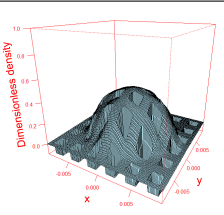


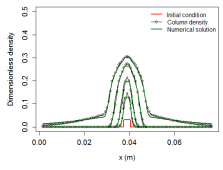

FIGURE 1.2 – Strategy of the thesis work.

1.3 Outline

This thesis is structured in four parts following the strategy mentioned above :

- **Chapter 2** describes the basic concept of wood and wood-decay fungi. The visualization technique to observe mycelia using confocal laser scanning microscopy, is introduced as well as its applications in the research of mycology. In addition, the mathematical models on fungal growth are reviewed.

TABLE 1.1 – Graphic summary of the thesis work.

	Experiment	Discrete model	Continuous model	
			1D	2D
Local scale in homogeneous media				
Local scale in porous media				
Macro-scale in porous media				

- In **Chapter 3**, the experimental study of the growth of *Postia placenta* is presented. A colony of *Postia placenta* was visualized using CLSM during 17 days. The morphological characteristics, such as tip extension rate, branching angle and segment length (the length between two adjacent branch/anastomosis sites along one hypha), were measured and analyzed. These experimental results were used to calibrate and validate the discrete model depicted in Chapter 4.
- **Chapter 4** presents the discrete model developed to mimic the temporal evolution of a mycelial network, which explicitly incorporated the main growth behaviors of hyphae, including hyphal elongation, branching and anastomosis. Different growth conditions were reproduced via tropisms which influenced the tip growth direction, especially the thigmotropism which provides the potential to simulate the mycelial growth in structurally heterogeneous media. The validation of this model was implemented through the experimental data from Chapter 3.
- **Chapter 5** proposes a continuous model capable of simulating the spatial development of fungi in porous media at the macro-scale. This model consists of a reaction

diffusion (RD) system and was derived by two successive upscaling steps from the results of the validated discrete model. The first step was to identify an equivalent RD equation from the radial biomass density of a mycelial network as simulated by the validated discrete model. Then, this equation was used to simulate the fungal growth in 2D periodic porous media. The computed local fields were averaged to obtain macroscopic biomass density fields, which were used to derive an equivalent macroscopic formulation (RD model and relevant parameters) for different morphologies of periodic porous media.

- **Chapter 6** presents the conclusion of this work and proposes the possible future work.

Chapter2

Literature review

This chapter starts with the basic concepts of wood anatomy and fungal decay, which are required as basic knowledge of this thesis work. After this general information, the remaining sections are devoted to the applications of confocal laser scanning microscopy (CLSM) and mathematical modeling of fungal growth, the two main families of scientific tools used in this work.

In section 2.1, the anatomical structure of wood is depicted as well as the wood-based products in the building industry. Then, the morphology of wood-decay fungi and the impact of environmental factors on their growth is described in section 2.2, where three wood rot types and the corresponding fungi are presented as well. A brief introduction of the principle of CLSM and its application in the research of mycology is given in section 2.3 namely to assess fungal growth. Finally, a state-of-the-art of mathematical modeling on fungal growth, especially at the local scale and the macro-scale, is presented in section 2.4.

2.1 Wood

2.1.1 Wood structure and composition

Wood is a porous and fibrous structural tissue found in the stems and roots of trees. It can be classified into two categories, softwoods and hardwoods. Softwoods, from gymnosperm trees, have a relatively homogeneous structure, which consists primarily of tracheids and uniseriate xylem rays. The tracheids insure two main function of plant stems : mechanical support and water diffusion. On the contrary, hardwoods, from angiosperm trees, have a more complex structure. The dominant feature separating hardwoods from softwoods is the presence of vessels that act as water conducting elements, while fibers and fiber-tracheids play the role of mechanical strength and support [17].

As this work deals with brown rot fungi which are predominantly associated with gymnosperms like Norway spruce [18], the anatomical part will be devoted on the structure of gymnosperms. As a consequence of seasonal changes in growth, the tree produces wood with a high porosity and the wood cells with thin walls (earlywood, more efficient for sap ascent) at the beginning of the vegetative period, whereas latewood is denser and with a thicker wall, more efficient for mechanical support (Fig. 2.1(a)). Most of the cells either in earlywood or latewood are tracheids (90 – 95%) which have the shape of small elongated tubes [19]. The average length of a Scandinavian softwood (Norway spruce) tracheid is approximately 2 – 5 mm and its width is 20 – 40 μm [20, 21]. The hollow void inside them is called the lumen which contains the living cell before lignification and serves for water transport in wood. The sap flow between two adjacent cells is achieved through a system of bordered pits.

The wood cell wall is composed of three main layers that consist of different ratios of cellulose, hemicelluloses and lignin [21] (Fig. 2.1(b)). Hemicelluloses are branched macromolecules that play an important role in connecting cellulose fibrils together. Finally, lignin forms the matrix of this natural nano-structured composite. The primary (P) wall is the proper cell wall which is a thin layer and contains a large amount of lignin. A much thicker secondary wall, subdivided into three layers, S1, S2 and S3, is added to the primary wall during lignification which marks the death of that living cell. The S1 layer is adjacent to the primary wall with a thickness of 0.1 – 0.2 μm and contains cellulose microfibril of which orientation is more or less perpendicular to the cell axis (70° – 90°) [23]. The S2 layer is much thicker (ca. 1 μm in earlywood and ca. 5 μm in latewood) and forms

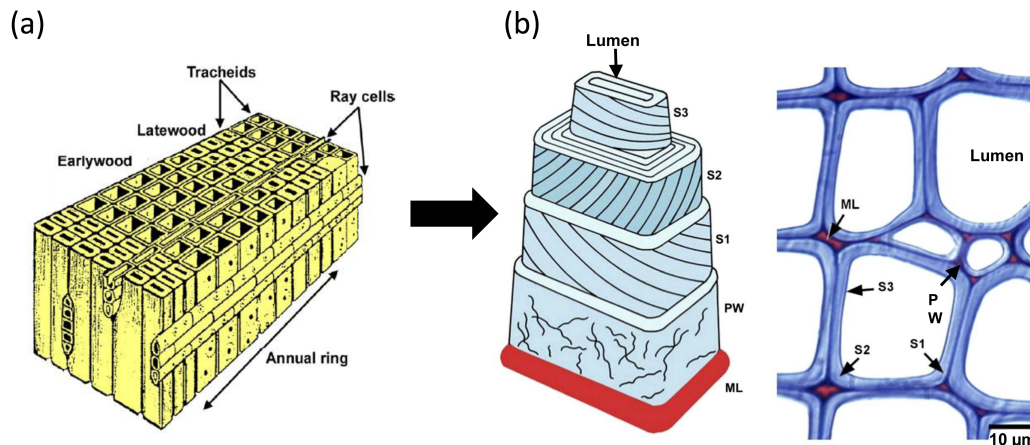


FIGURE 2.1 – Schematic illustration of (a) the anatomical pattern of softwood [20], and (b) cell wall with five layers : the middle lamella (ML), the primary wall (PW), the three-layer secondary wall (outer (S1), middle (S2) and inner layer (S3)), and the lumen [22].

the main portion of the cell wall. It consists of cellulose microfibrils, linked by branched hemicelluloses and lignin, that spiral around the axis of the cell ($0^\circ - 30^\circ$) and contributes mostly to the mechanical strength in the longitudinal direction. In the thin layer of S3, the microfibrils orientation to the cell axis is $60^\circ - 90^\circ$ [24]. The walls of adjacent cells are bonded through a layer rich in lignin called the middle lamella (ML).

2.1.2 Wood material

As a building material, wood cumulates several advantages. From an ecological point of view, wood is the perfect example of a sustainable product : it is renewable and carries the lowest carbon footprint of any comparable building material. Moreover, no high-energy fossil fuels are required to produce wood, unlike other common building materials such as aluminum, brick, steel or plastic. In terms of construction, wood is remarkably rigid and strong, both for tensile and compression loading, in relation to its density. Since wood is highly machinable, it can be processed into many wood-based materials, shapes and sizes to fit practically any construction need. In addition, among the structural materials, wood presents the best thermal properties and presents interesting acoustic properties. Thus, due to this unique combination of properties, wood and wood-based products are used in various applications, such as framing, flooring, wall coverings, ceilings and furniture.

Depending on the application, wood material in the building industry can be classified into ordinary lumber/timber and engineered wood (Fig. 2.2). The lumber and timber are simply produced from logs by sawing and are distinguished by their dimensions. Pieces of wood that are smaller than 5 inches (12.7 cm) wide by 5 inches thick (regardless of length) are generally referred to as lumber, while those over 5 inches wide by 5 inches thick (regardless of length) are named as timber. Furthermore, any timber pieces that exceed 8 inches (20.3cm) wide by 8 inches thick are referred to as beams. As timber pieces are larger in dimension, they are often used to construct the frames of large structures such as buildings and bridges. Engineered wood belongs to the family of wood-based products. They are produced by a deconstruction of wood in more or less small parts (veneers, chips, particles, fibers etc.) that are processed together to form a new material, generally via an adhesive. Common examples of engineered wood include :

- **Plywood** is made from three or more thin layers of wood veneer glued together to form a thicker and flat sheet which has a wide range of applications, such as flooring, beams, wall cladding and furniture. Comparing with lumber or timber, plywood is more flexible in manufacturing and presents an excellent dimensional stability as a result of the cross-orientation of veneers.
- **Glued laminated timber (i.e., glulam)** is a type of structural engineered wood product composed of wood laminations that are bonded together with durable, moisture-resistant adhesives. Glulam has greater strength and stiffness than comparably sized dimensional timber. Moreover, due to its composition, glulam can be manufactured from a variety of smaller trees and allows more design flexibility than traditional timber construction.
- **Oriented strand board (OSB)** is formed by adding adhesives and compressing layers of wood strands in specific orientations and is commonly used for load-bearing applications due to its high mechanical properties.
- **Fiberboard** is made of wood fibers in different fashion to obtain different densities. The common use of low-density fiberboard is the insulation of sound and heat, while the denser ones are heavily used in the furniture industry.

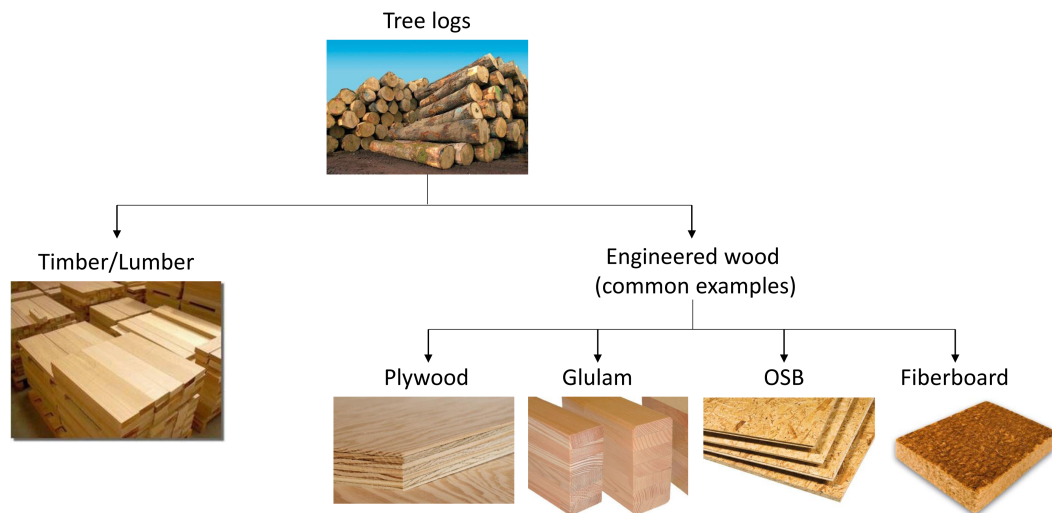


FIGURE 2.2 – The two major categories of wood-based construction products manufactured from tree logs : timber/lumber and engineered wood.

2.2 Wood decay fungi

2.2.1 Morphology

Wood decay fungi are a group of multi-cellular fungi that digest damp wood. Their vegetative part, the mycelium (Fig. 2.3 (a)), is a dense network consisting of filamentous structures called hyphae (Fig. 2.3 (b)). Fungal hyphae are essentially tubular in shape, surrounded by a rigid wall that separates the fungus from the external environment. Depending on the type of fungus, hyphae can be one large multi-nucleated cell devoid of inner cross-walls called septa (e.g., zygomycete hyphae) or can have septa between individual cells (e.g., ascomycete and basidiomycete hyphae) [25]. Generally, septa are perforated by pores allowing ribosomes, mitochondria and sometimes nuclei to flow between cells. According to the type of hyphae, their diameter reaches from $0.1 - 0.4 \mu\text{m}$ for the microhyphae (e.g., *Phellinus pini*) to $60 \mu\text{m}$ for the vessel hyphae in the mycelial strand (cord) (e.g., *Serpula lacrymans*), with an average for vegetative hyphae of about $2 - 7 \mu\text{m}$ [4].

Hyphae typically emerge from germinating spores, other reproductive structures (e.g., sclerotia) or hyphal fragments. With few exceptions, hyphae elongate strictly by apical deposition of wall skeletal polysaccharides, especially chitin and β -glucans [26]. This extension occurs as new materials added to the cell wall at the extreme apex and is driven

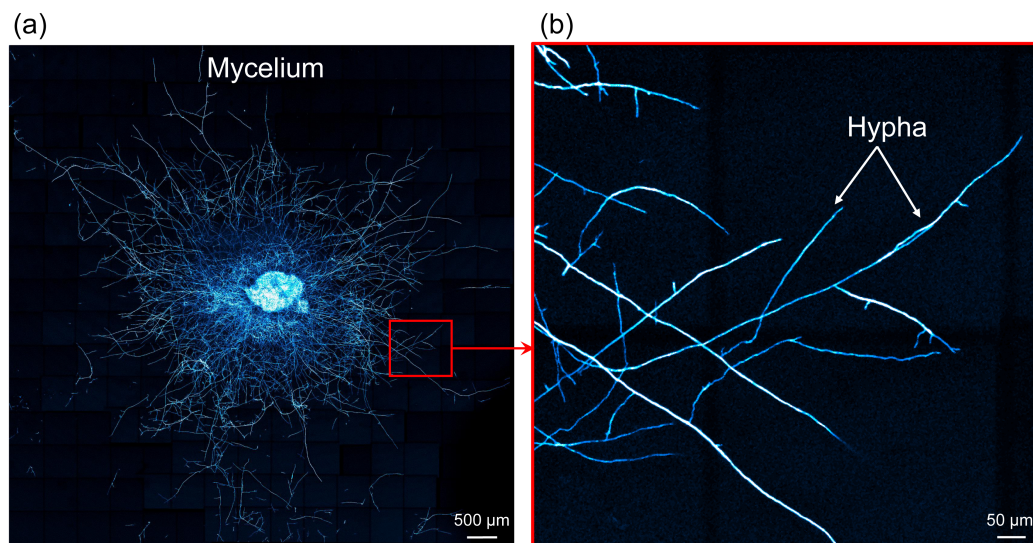


FIGURE 2.3 – The mycelium of the filamentous fungi, *Postia placenta*, formed by tubular cells (i.e., hyphae) with an averaged diameter of $3\ \mu\text{m}$. The images were visualized using confocal laser scanning microscopy.

by turgor pressure. This hyphal morphogenesis is linked with the existence of a special structure called Spitzenkörper which is found at the apex of hyphae of ascomycetes and basidiomycetes and plays a crucial role in the growth and orientation of hyphal tips. It is described as a complex, multicomponent structure dominated by vesicles which are bubble-like objects storing and transporting substance for the formation of the cell walls [27].

Additional important features of hyphal morphogenesis include branching formation [28] and anastomosis (i.e., hyphal fusion) [29]. Due to branching, new hyphae emerge from preexistent ones to form the network structure of the mycelium and increase its surface area. Hyphal fusion is a mechanism in which two hyphae fuse and exchange cytoplasmic contents. It appears to be important for intra-hyphal communication, translocation of water and nutrients, and general homeostasis within a colony [30].

2.2.2 Physiology

The growth of wood decay fungi as well as their damage to wood are influenced by various physical, chemical and biological factors, such as nutrients, water, air, temperature,

pH value, light, electrical fields, physical contact and interaction with other organisms [4, 31, 32, 33, 34]. The most important and common factors, such as nutrients, moisture content, temperature, oxygen and pH value are discussed below :

- **Nutrients**

Wood fungi are heterotrophic and hence need a source of carbon from organic material. Regarding nutrients, wood-decay fungi digest and absorb carbon from the complex, main components of the woody cell wall, cellulose, hemicelluloses and/or lignin. It is widely accepted that fungi growing in low-nutrient conditions adopt an 'exploratory' phase during which new emerged branches are largely suppressed [35].

- **Moisture content**

Water is used for the uptake of nutrients, transport within the mycelium and as a solvent for metabolism. The critical limit of water activity for fungal growth on wood is around 75 – 80% (which is also the ambient air humidity in equilibrium conditions) and the growth is more rapidly at higher humidity [36]. However, there is evidence indicating that too much water does prevent fungal development as demonstrated by the conservation of organic matter in permanently saturated environments like lake sediment [37].

- **Temperature**

Generally, the minimum temperature for survival of wood-decay fungi is at 0 C° because no liquid water is available below the freezing point, while the maximum temperature for mycelial growth and wood damage is often at 40 – 50 C° due to the denaturation of the enzymes by heat. The optimum lies between 20 – 40 C° depending on species ([4] and references therein).

- **Oxygen**

Wood-decay fungi are aerobic organisms and therefore need oxygen. Fungal activity is therefore affected by the composition of the surrounding gaseous phase. Usually wood decay decreases at low O_2 and high CO_2 content. Nevertheless, some wood-degrading basidiomycetes, (one of two large phyla, together with ascomycetes, that constitute the "higher fungi"), are tolerant of a high CO_2 content, since they grow well at 70% CO_2 [38].

- **pH**

The pH value influences germination of spores, mycelial growth and enzyme activity for wood degradation. The optimum for wood-decay fungi is often in a slightly

acidic environment of pH 5 – 6 [39]. Basidiomycetes have an optimum span of pH 4 – 6 and a total range about 2.5 – 9. Ascomycetes may tolerate more alkaline substrates to about pH 11.

2.2.3 Wood decay types

Wood-decay fungi are typically classified into three types : white rot, brown rot and soft rot [4]. They are nominated after the outward appearance of the decayed wood and essentially distinguished by the different decay mechanisms. Wood attacked by white rot fungi takes on a fibrous appearance and tends to go slightly lighter in color. As shown in Fig. 2.4(a)(b), these fungi can either degrade cellulose, hemicelluloses and lignin at the same time and at a similar rate, or decompose lignin faster than the other two components [40, 41]. Brown rot and soft rot fungi are chemically similar as both of them decompose cellulose and hemicelluloses with little lignin attack. However, their decay pattern to the wood cell wall is different. Typically, brown rot fungi grow inside the cell lumen and they are in close contact with the S3 layer of the wood cell wall. The ectoenzymes produced by brown rot fungi are diffused into the S2 layer (the thickest layer that consists mainly of cellulose and hemicelluloses) and cause rapid degradation of this layer without decomposing the highly lignified middle lamella and S3 layer [42] (Fig. 2.4(c)). Due to the rapid decomposition of cellulose, the wood dimensions are significantly reduced. The wood cracks into crumbly cubes because of shrinkage and the remaining modified lignin gives the decayed wood a "brown" color. Unlike brown rot, soft rot causes a spongy texture on the wood surface. The distinguishing feature of soft rot fungi is that they grow mainly inside the wood cell wall. Around the penetration hyphae, cavities are formed and developed with the apical growth of these hyphae, which breaks down the secondary wall gradually as shown in Fig. 2.4(d). The decay features of these three types of wood decay fungi are summarized in Table 2.1.

Among these wood decay fungi, brown rot fungi are typically associated with gymnosperm trees (e.g., conifers), which is the major source of timber used in construction in the Northern hemisphere [18]. In this region, a large part of wood in service is destroyed due to brown rot fungi. The present work is focused on this type and for simplicity, a species of brown rot fungi, *Postia placenta*, was selected.

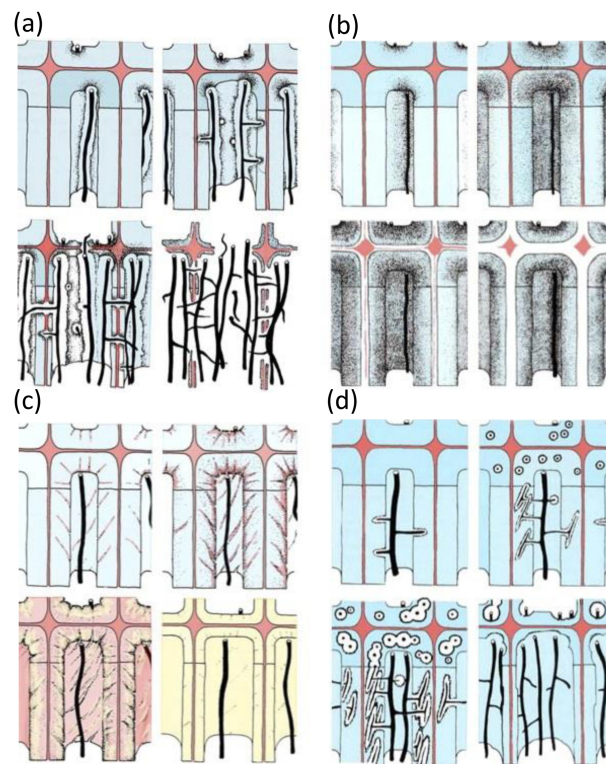


FIGURE 2.4 – Schematic showing micro-morphological features of different decay types. (a) Simultaneous rot by *Fomes fomentarius*, a white rot fungus : degradations occur in the vicinity of abundant hyphae growing with the lumen and the cell wall is progressively degraded from the lumen outwards. (b) Selective delignification by *Heterobasidion annosum*, a white rot fungus : low molecular weight substances (shown as dots) diffuse into the secondary wall from hyphae growing in the lumen to degrade hemicellulose and lignin within the secondary wall as well as ML, but remaining cellulose intact. (c) Brown rot by *Fomitopsis pinicola* : low molecular weight substances are secreted by hyphae growing on the S3 layer and diffuse radially into the cell wall to degrade hemicellulose and cellulose in the secondary wall. S3 and ML remain intact due to the involvement of abundant lignin. (d) Soft rot by *Kretzschmaria deusta* : decay hyphae diffuse into the secondary wall with parallel orientation to that of the cellulose microfibrils in the S2 layer. Cavities are formed by these decay hyphae and the secondary wall is nearly completely broken down [41].

2.3 Visualization of mycelial growth using CLSM

Visualization and observation of mycelia has been performed using different devices accessible at the laboratory scale. The common techniques include optical microscopy [44, 45, 46] and electron microscopy [47, 48]. Classical optical microscopy permits rapid observation of many staining specimens with moderate preparation, but is constrained by

TABLE 2.1 – Decay patterns of the three types of wood decay fungi [43].

	Brown rot	White rot		Soft rot
		Simultaneous rot	Selective delignification	
Host	Especially in coniferous trees	Broad-leaved trees, but seldom in conifers	Broad-leaved trees and conifers	Extensive decay in living broad-leaved trees
Fungi	Basidiomycetes	Basidiomycetes and Ascomycetes	Basidiomycetes and Ascomycetes	Ascomycetes
Degradation	Cellulose and hemicellulose	Cellulose, lignin and hemicellulose	First lignin and hemicellulose, later cellulose	Cellulose and hemicellulose ; lignin slightly
Consistency	Fragile, powdery, brown ; cracks and clefts	Brittle	Fibrous (stringy)	Brittle
Strength	Drastic reduction of bending and impact strength	Brittle	Less drastic than in brown rot	Between brown and white rot

sample thickness and provides only two-dimensional information. Electron microscopy has a large field depth able to produce images free of focus blur, but samples need to be dehydrated, resulting in inactivating living samples and preventing time-laps observations. Alternatively, confocal laser scanning microscopy (CLSM) enables non-destructive methods to observe fungal growth and realize three-dimensional imaging at a high resolution. In order to visualize and analyze the mycelial growth on a solid medium, the CLSM was applied in our work.

2.3.1 Principle of CLSM

CLSM is a powerful tool for generating 2D and 3D images (stack of confocal images) with high resolution in using fluorescence in photonics imaging. The key feature of CLSM is its ability to produce blur-free images of thick specimens at various depths. The principle

for this kind of microscopy was built by Marvin Minsky in 1955 and then it took another thirty years to be developed as a standard technique toward the end of the 1980s [49].

Fig. 2.5(a) is a simplified schematic showing the structure of CLSM and how CLSM works. One or more laser beams of a specific wavelength are directed through a dichroic mirror to the laser scanning mirrors, and then they are focused by a series of objective lens to a small diffraction-limited spot at the focal plane in the specimen. The fluorescence (at a wavelength longer than the illumination light) emitted by the illuminated spot is filtered by the pinhole and an emission filter, and finally is detected by a photomultiplier tube (PMT). The decisive design feature of a CLSM compared with a conventional microscope is the confocal aperture called a pinhole arranged in a plane conjugate to the object plane of the microscope. As a result, only the light coming from the confocal plane can be detected by PMT (Fig. 2.5(b)). When the diameter of the pinhole is sufficiently small, the light detected looks like a point. The illuminated spot in the specimen and the observed point are situated in conjugate planes, which is called a confocal beam path. Thus, only one point in the specimen is detected and the entire image is visualized point by point by a scanning process. The functions of the principal optical components are depicted as follows :

- **Laser system**

The advantage of the laser instead of a source of white light is to provide a more specific monochromatic light with high intensity and is easy to control in terms of filtering. The lasers used in Zeiss LSM700 CLSM (which we applied in our experiment) are solid-state lasers with wavelengths of 405 nm, 445 nm, 488 nm, 555 nm and 639 nm, respectively.

- **Dichroic mirror**

A Dichroic mirror spectrally separates light by transmitting and reflecting light as a function of wavelength. Typically, it allows a certain range of colors to be transmitted and reflects the others. In the CLSM, it is used to separate the emitted light from the excited light.

- **Laser scanning mirrors**

As a result of its principle, a CLSM realized a point-to-point scanning of the specimen in the $x - y$ plane. This is ensured by two orthogonal mirrors with accurate motion to control the x and y movements of the laser beam.

- **Pinhole**

The pinhole is used to reject the light coming from the specimen points outside the focal plane before the detection. By varying the pinhole diameter, the degree of confocality can be adapted to practical requirements. Generally, the size of the pinhole is automatically adjusted by CLSM to the optimal width according to the objective used. However, we can artificially regulate its size in the special case (e.g., weak signals can be offset by enlarging the opening to collect more light).

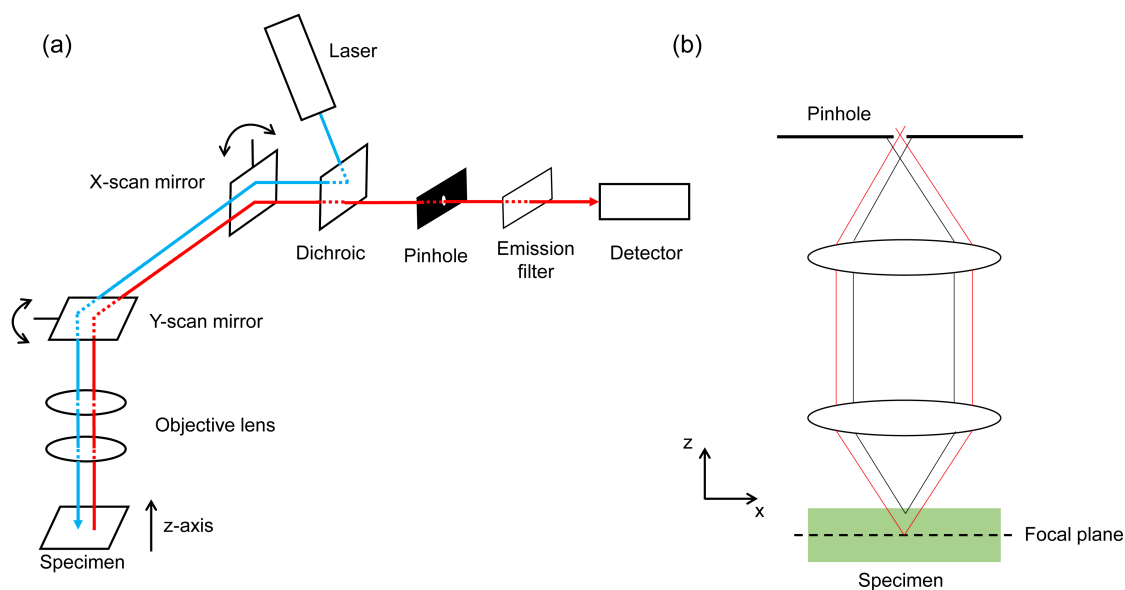


FIGURE 2.5 – (a) Schematic of principle of CLSM; the blue lines denote the laser beams and the red lines represent the fluorescence emitted by the specimen. (b) Placed in the conjugate plane, the pinhole eliminates the light coming from any specimen point outside the focal plane.

2.3.2 Fluorescent dyes

CLSM uses fluorescence emitted by the specimen to generate images. Some samples, like wood, possess the intrinsic fluorescence, called auto-fluorescence, which can be directly observed using CLSM by choosing the best laser lengthwise. In the absence of sufficient auto-fluorescence, the sample should be labeled by fluorescent dyes or expressed by fluorescent proteins. Each fluorescent dye responds to a special excitation wavelength and emits a corresponding emission wavelength. Some dyes can be used as vital dyes and others may inhibit or be toxic to the living specimen. Note that some high concentration of vital dyes also can influence the growth of living specimen. Furthermore, while staining, the concentration of dyes influences directly the quality of images. Overall, in order

to realize successful imaging, a fluorescent dye should be carefully selected in consideration of its excitation and emission spectra, quantum efficiency, tendency to photo-bleach as well as the organelle stained and its impact to the living specimen.

2.3.3 Imaging capabilities

With a CLSM, it is possible to image a thin optical slice in good contrast out of a thick depth (up to $100\mu\text{m}$), known as optical sectioning. CLSM allows an automatic collection of a series of optical sections at pre-chosen intervals along the z-axis. The interval between successive optical sections can be different of the optical section thickness (larger or smaller) depending on the visualization requirement. The optical sections recorded at different z-planes of the specimen can be reconstructed to a 3D image. The quality of this image depends on the thickness of the slice and the spacing between successive slices.

Moreover, if the scan rate is sufficiently fast regarding the phenomena to be observed, a time series of images can be recorded to realize the observation of the dynamic changes of the living specimens. If necessary, reducing the image size and changing the scan mode can reduce significantly the scan rate. Again, CLSM can automatically scan the specimen with the same frequency in a pre-chosen period of time. When the frequency reaches a sufficiently high rate (at least 30 frames per second), a real-time imaging can be achieved. In addition, the fluorescent dyes have a selectivity on staining organelles, such as cell walls, membrane and nuclei. Due to a special multichannel PMT in CLSM, of which each channel can possess different laser sources and detect different fluorescent signals, it is possible to distinguish different parts of the specimen.

2.3.4 Application of CLSM

Due to the numerous capabilities of CLSM mentioned above, it is widely applied in fungal research for visualization of their shape, size, morphology and internal structure. One of the common applications is to investigate the growth behaviors of hyphae and help understand the mechanisms by using various vital fluorescent dyes ([50, 51] and references therein). For example, the vital fluorescent dyes combined with membranes are widely used in investigating the patterns and the dynamics of hyphal growth behaviors, like the distribution of the vacuoles, the migration of Spitzenkörper and the movement of the mito-

chondrial during hyphal elongation, branching formation and hyphal fusion [52, 53, 54]. Fig. 2.6(a) shows the flow of organelles of the stained hyphae to a non-stained hypha during hyphal fusion. Cell wall stains allowed the relationship between branch sites and hyphal septa to be observed [28]. The cytoskeleton has been also a major subject yielding new information on the spatial and temporal organization of microtubules in growing hyphae and in relation to cell wall formation [55, 56] (Fig. 2.6(b)).

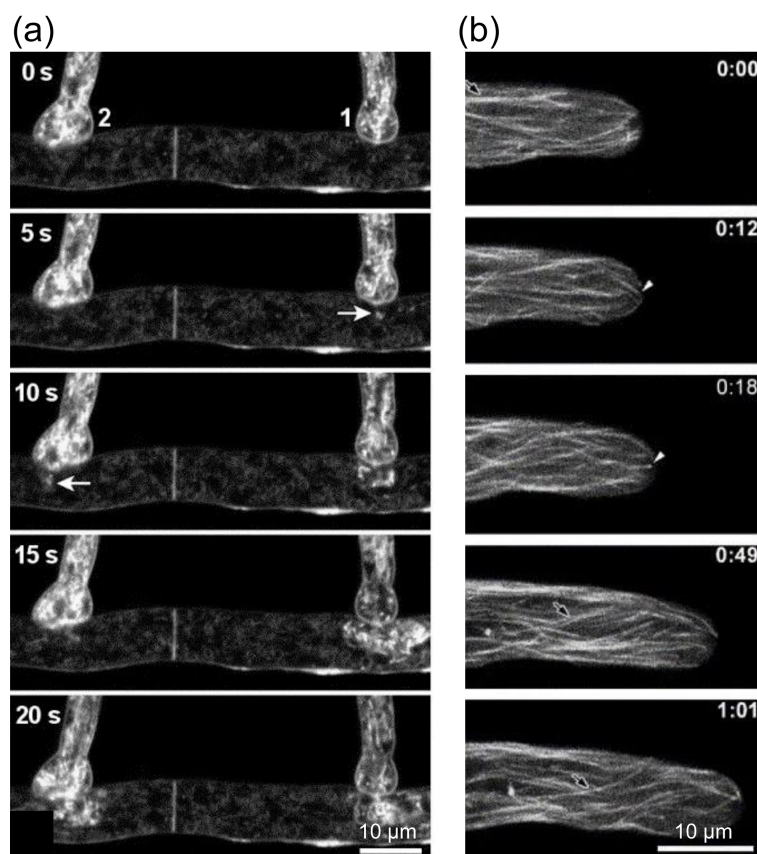


FIGURE 2.6 – Examples of the investigation on hyphal growth dynamics in using CLSM with vital fluorescent dyes : (a) Tip-to-side hyphal fusion between hyphae of two mycelia differentially stained with FM1-43 to investigate the flow of organelles between the two hyphae [54]; (b) Microtubular cytoskeleton in growing hyphal tip labeled with GFP [55].

Advanced imaging capabilities, like 3D reconstruction and Multichannel technique, make it possible to observe the fungal growth within biological materials as well, like plant roots or wood, and quantify the hyphal growth characteristics. M. Schubert (2014) developed the 3D filamentous growth of *Physisporinus vitreus* in Norway spruce wood by application of two channels with different excited lights and separating the signals respectively

emitted by labelled hyphae and wood [57] (Fig. 2.7(a)). The visualization of arbuscular mycorrhizal fungal structures in living roots have been realized in using CLSM as well as the quantification of their surface area and volume [58, 59] (Fig. 2.7(b)).

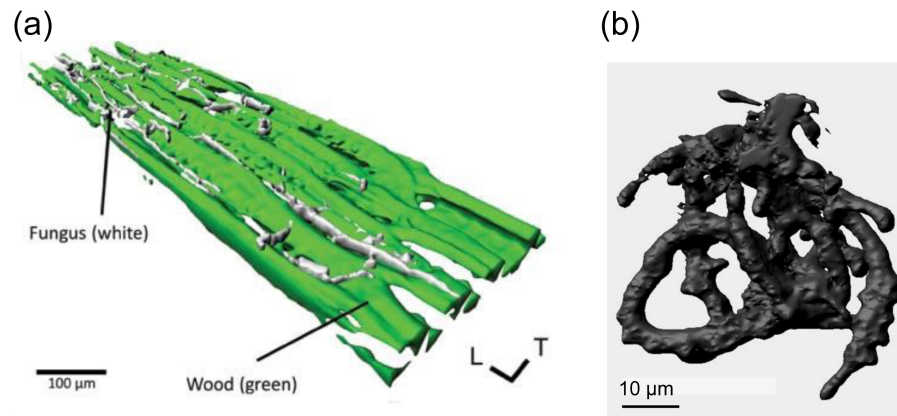


FIGURE 2.7 – Examples of the 3D reconstruction of hyphae in using CLSM : (a) Transverse section of Norway spruce heartwood (green) colonized by hyphae (white) of *Physisporinus vitreus* [57]; (b) Paris-type coil of *Scutellospora calospora* in *Lilium sp.* [58].

2.4 Mathematical modeling of fungal growth

Mathematical modeling is a powerful tool to investigate mycelial growth, which is complementary to the costly and tedious experimental studies. It is a description of a system using mathematical concepts and languages. The objective of a mathematical model is to reduce a complex (biological) system into a simpler model, able to reproduce, or even better predict, partly the real system. A recurrent question regarding modeling is to dose (carefully consider) the degree of simplification : too complex, a model is difficult to solve and needs to be fed by many parameters, too simple, the model is no longer capable of relevant predictions or realistic simulations. Indeed, the gap is often huge from a cognitive model to an operational model. Fungi are in general very difficult to study in their natural habitats by using experimental methods alone due to their complex growth mechanisms and the extremes of spatial scales. Although fungal hypha is only a few microns in diameter, the indeterminate growth habit of the mycelium can produce massive organisms (one colony of *Armillaria gallica* covers over 15 hectares of forest [60]). As a complementary and efficient tool to laboratory experiments, mathematical modeling is capable of mimicking and forecasting the behaviors of mycelial growth on various scales and give

a deeper insight into the intricate interactions between fungi and their environment.

In general, three scales are classified in modeling mycelial fungi : micro-scale, colony scale and macro-scale. The development of hyphal tips is the main focus in the research at the microscale (Fig. 2.8(a)), ranging from simple geometrical models [61, 62] to sophisticated mechanical ones ([63] and references therein). In geometrical models, the increase in the wall area of an advancing hyphal tip is balanced with the incorporation of wall building material without specifying the details of underlying biological processes. Besides, mechanical models aim at capturing the tip growth through a proper description of the physical stresses and strains experienced by the growing hypha. The colony-scale models produce centimeter-colony (Fig. 2.8(b)) by considering the development of fungal hyphae via both discrete [64, 65, 66, 67, 68] and continuous modeling approaches [69, 70, 71]. The discrete models focus on the behaviors of individual hypha and the morphology of mycelial networks, while the spatial distribution of hyphae is represented by the continuous ones depending on various environmental factors. At the macro-scale, the interaction of fungi with their environment is the main objective of modeling. Examples include the modeling of fungal crop pathogens [72, 73], the production of fungal biomass by consumption of nutrients [74], the transmission of the fungal infection [75] and the fungal decay in bio-based materials [76]. As we are interested in models on mycelial growth and fungal decay in wood which describes at the macro-scale the global damage assessment, some examples of the colony-scale and the macroscale modeling approaches are presented below.

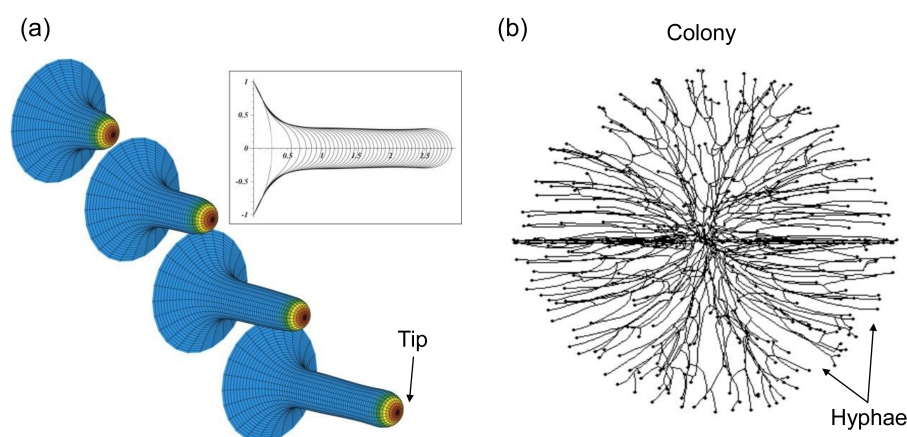


FIGURE 2.8 – Difference between modeling at the (a) microscale, which models the growth of the hyphal tip [63], and (b) at the colony scale, which models the mycelial network [77].

2.4.1 Colony-scale models

2.4.1.1 Discrete models

In discrete models, individual hypha is identified to mimic mycelial networks in incorporating hyphal growth behaviors. Two sub-groups can be further divided : lattice-based and lattice-free models. The former approach arranges the mycelium in a predetermined lattice, while in the latter one, a collection of connected line segments constitute the mycelium. Both approaches have advantages and disadvantages. The lattice-based approach restricts the topology of the network by the lattice, so that the mycelium constructed possesses a regular geometry which may fail to sufficiently capture the complex behavior exhibited, like the representation of mycelial growth in response to various tropisms. However, the regular geometry makes this approach more efficient, computationally, in comparison with lattice-free modeling because there are a finite number of orientations adopted and a finite number of rules governing the development of the biomass structures. Except for shortage in computational efficiency, the lattice-free models apply global growth rules of hyphae rather than the underlying mechanisms of hyphal growth, resulting in difficulties in testing hypotheses concerning changes of growth dynamics. The advantage of lattice-free models is the production of lively morphology indistinguishable from the real mycelium due to the non-constrained orientations of the line segments. Some models in adopting the two approaches are presented below.

Lattice-based models

In the lattice-based models, a regular lattice is used as the geometrical basis for developing mycelial network by formulating a series of stochastic rules applied on the nodes of the lattice. Ermentrout and Edelstein-Keshet (1993) [64] used a cellular automata (CA) method to develop a “solidification” model on a square-lattice to produce fungal growth patterns. The basic rule was that once a node was occupied, it remained occupied. This was also called a “bond” model. The growth mechanisms were tip splitting as a means of growth and cross-linking as a way to limit over-growth. Despite the simple growth mechanisms, a variety of networks were constructed capturing fractal-like structure of mycelium in uniform growth conditions (Fig. 2.9).

Another CA model (i.e., a hybrid CA model) was developed by Boswell *et al.* (2007) [65]. Its key feature was the simultaneous use of a combination of “cell” models (which

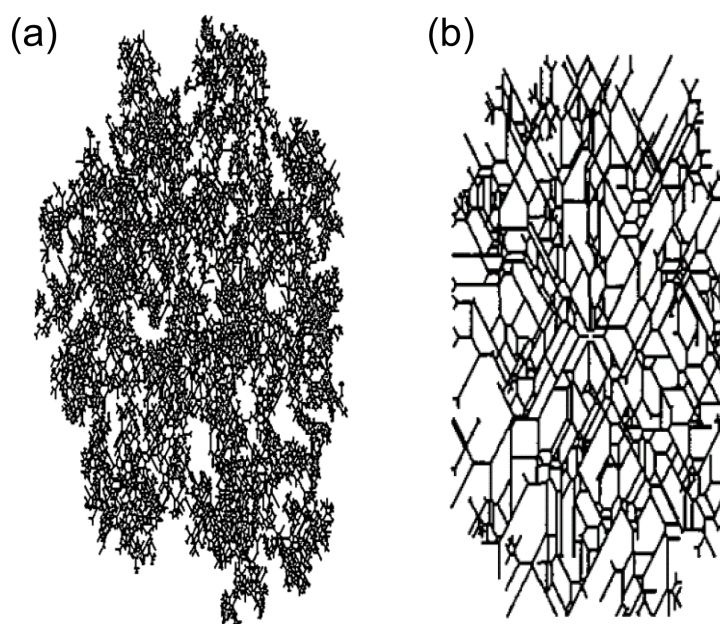


FIGURE 2.9 – Mycelial networks constructed in uniform growth conditions by Ermentrout and Edelstein-Keshet (1993) [64] : the probability of tip splitting and of tip inactivation is higher in (a) than in (b).

were used for modeling substrate and hyphal tips) and “bond” models (which were used for modeling hyphae). The mycelium was modeled using a triangular lattice embedded in a hexagonal lattice used to model the substrate distributions. More complex growth mechanisms were incorporated into the model in considering nutrient translocation and the relationship between nutrients concentration and hyphal growth. This enabled simulation of the growth of hyphal networks in response to heterogeneous environments. Some examples of mycelial growth in various environments are shown in Fig. 2.10.

Smith *et al.* (2011) adopted a novel approach *network automata* (NA) to describe the distribution of resources within the mycelial network [78]. In contrast to CA, in which the state of each node in the lattice evolved according to its own state and that of its neighborhood, in the NA, the connections in network were updated at each time step. Such an approach was particularly suitable in coupling the topological network to a dynamic process occurring upon the network.

The models presented above were all bi-dimensional, which generated mycelial networks on a $x - y$ plane. The three-dimensional (3D) models were also developed using a lattice-

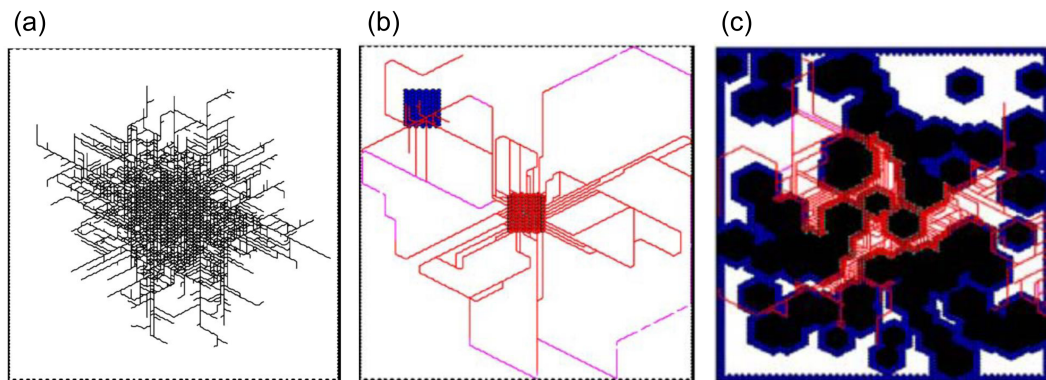


FIGURE 2.10 – Simulations of mycelial growth (in black or in red) in various environments in Boswell *et al.* (2003) [71] : (a) homogeneous environment, (b) with located food sources (blue), and (c) soil-like environment.

based approach. For example, a 3D version of the hybrid CA model was constructed by Boswell (2008) [79] in focusing on the formation of mycelia in soil-like systems using a face-centered cubic (FCC) lattice (Fig. 2.11). Another 3D model, developed by Coradin *et al.* (2011) [66], simulated the growth of the aerial hyphae to further understand the role of filamentous fungi in solid state fermentation processes.

Lattice-free models

The first attempt to develop a lattice-free model for branching networks was conducted by Cohen (1967) [80]. The networks consisted of unit segments via a set of simple growth and branching rules. Filamentous fungi were considered as one of the applications of this model, which created a template for the construction of numerous models afterwards.

Based on this model, Yang *et al.* (1992,1992a) developed a hybrid model that generated an explicit network of mycelial microorganisms in incorporating apical growth, septation and branching [81, 82]. Part of the rules governing branching and hyphal tip extension were based on fundamental cellular and physical mechanisms. The result of this model corresponded closely to the observation in experiments.

A related approach was adopted by Meskauskas *et al.* (2004,2004a) [67, 77] to develop a Neighbor-Sensing model which brought together the basic essentials of hyphal growth kinetics into a vector-based model. This model considered the impact of various tropisms, including negative autotropism, galvanotropism and gravitropism, to hyphal growth and

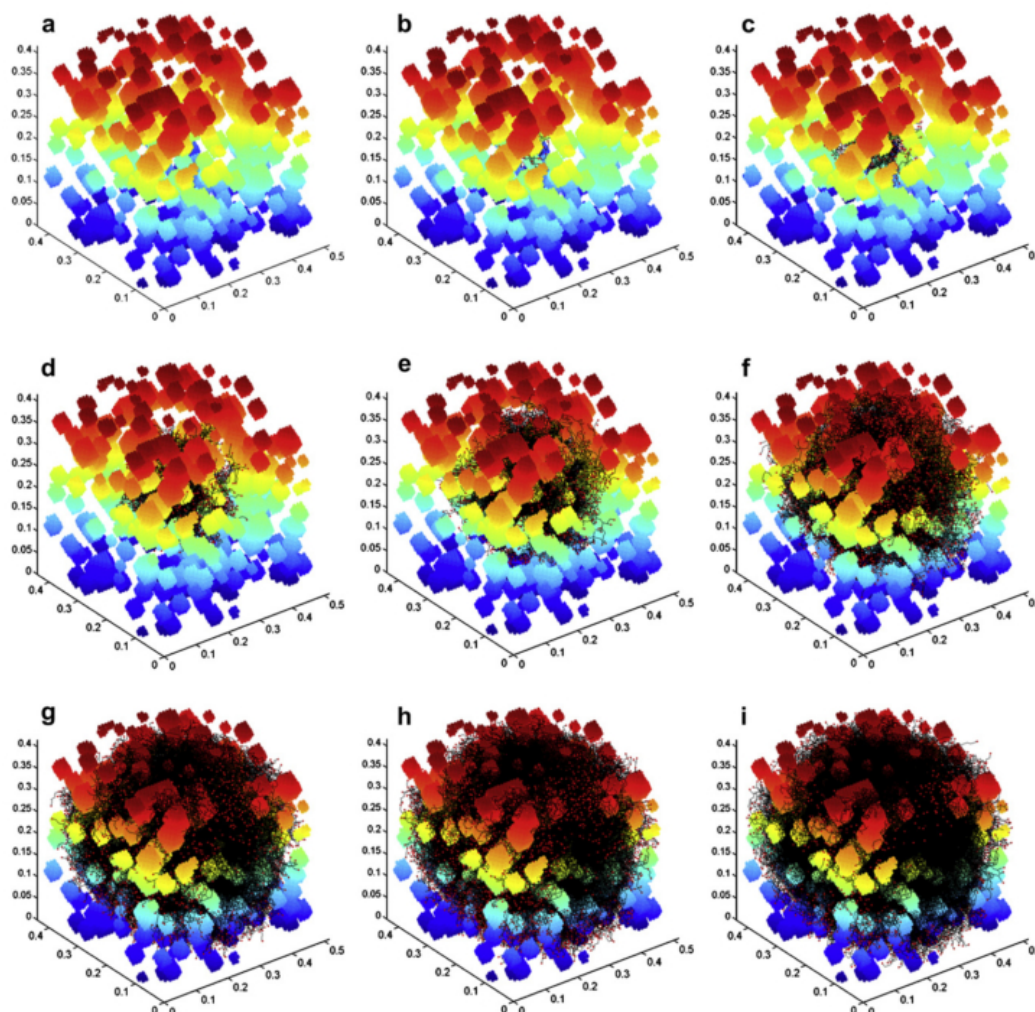


FIGURE 2.11 – The evolution of the mycelial network (black) expanded in a soil-like environment with time : (a) $t = 0$, (b) $t = 0.05$, (c) $t = 0.1$, (d) $t = 0.15$, (e) $t = 0.2$, (f) $t = 0.25$, (g) $t = 0.3$, (h) $t = 0.35$, and (i) $t = 0.4$ day. The 'soil particles' were colored according to their z-coordinate (Boswell (2008) [79]).

could simulate various morphology of mycelium as well as complex fungal fruit body shapes in 3D space (Fig. 2.12).

Another lattice-free model was developed by Carver and Boswell (2008) [83] in incorporating anastomosis and the interconnected nature of mycelium. During each timestep, every tip could extend a fixed distance with a probability that increased with the internal substrate concentration and in a direction normally-distributed from its previous orientation. Hopkins and Boswell (2012) [68] extended this model to allow the simulation of

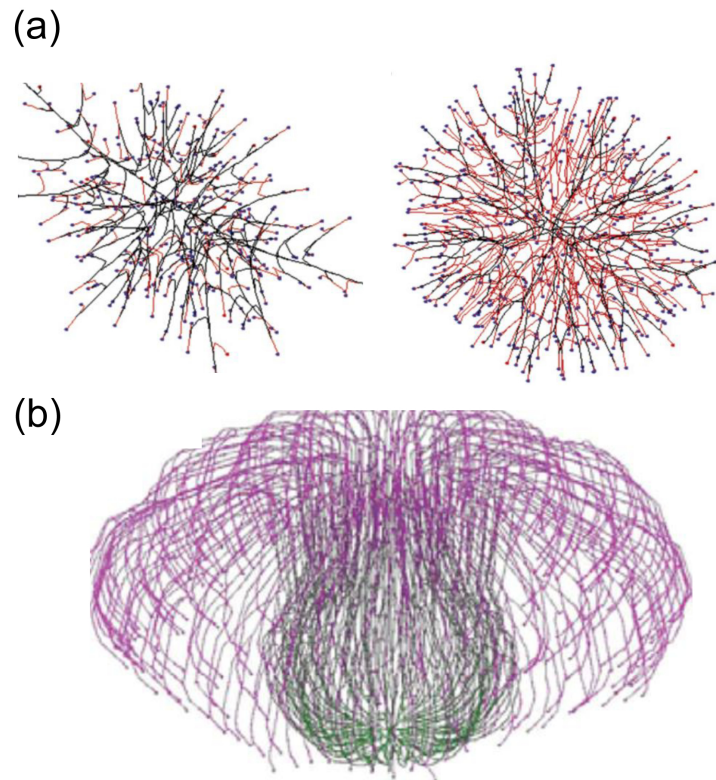


FIGURE 2.12 – Examples of (a) hyphal growth patterns and (b) fungal fruit body shape in the Neighbor-Sensing model developed by Meskauskas *et al.* (2004,2004a) [67].

planar growth in arbitrary nutritional conditions (Fig. 2.13). An important advance was the application of a biased circular random walk to model tip orientation in response to the tropisms that existed in the growth environment. In using this process, the manner in which the bias of the reorientation of hyphal tips can be easily calibrated so that the mycelial growth in a range of conditions could be simulated.

In addition to the models mentioned above, Fuhr *et al.* (2011) developed a lattice-free model aiming at investigating fungal growth in wood [84] (Fig. 2.14). An important part of the model was to construct a simplified wood structure which was a network of tracheids connected by bordered pits (nutrient source). The complex fungal growth was reduced to a pit-to-pit growth. The model enabled the analysis of the effects of microscopic parameters, such as the degradation rate and degree of opening of pits, on macroscopic system properties as well such as penetration depth of the fungus, biomass, distribution of destroyed pits in early- and late-wood and the alteration of the permeability.

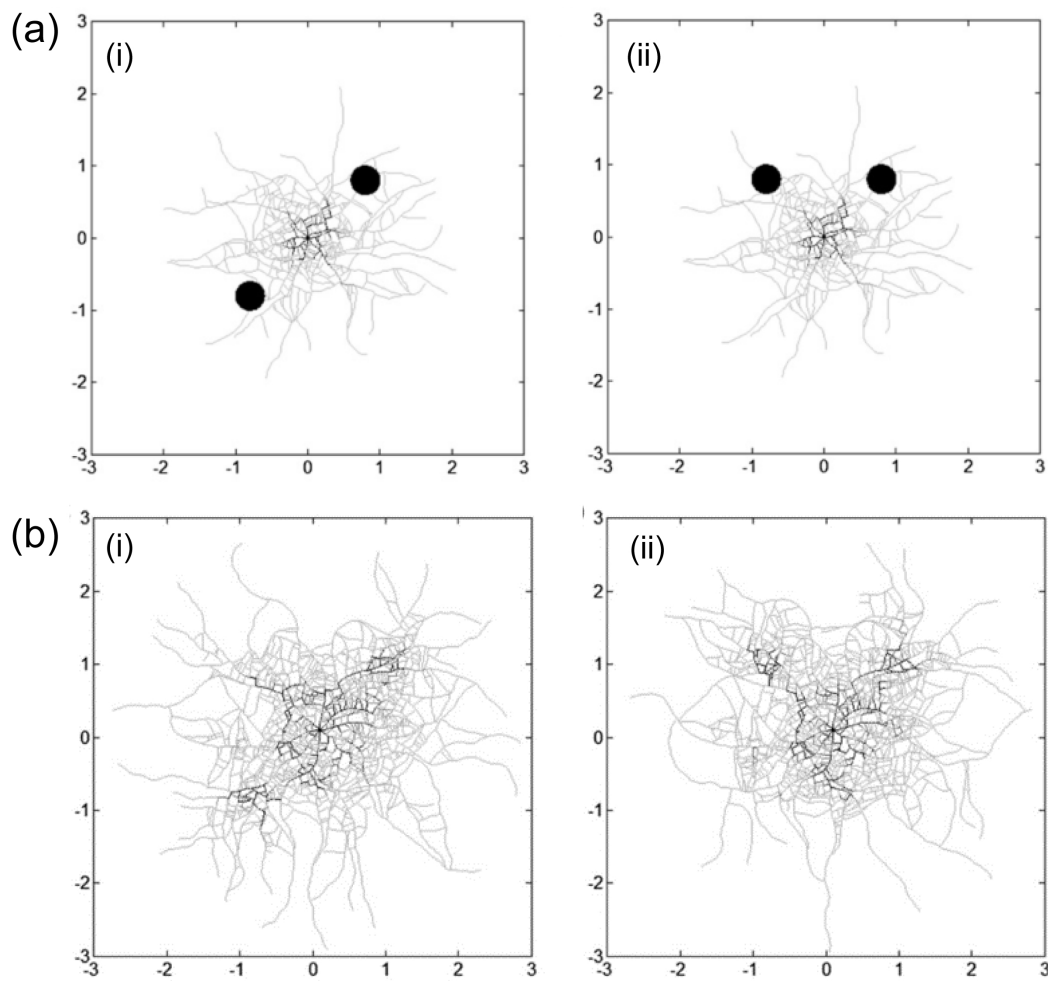


FIGURE 2.13 – Example of planar growth of mycelium in Hopkins and Boswell (2012) [68] : (a) Initial setup for two instances (i) and (ii); darker line segments denote higher internal substrate concentration and circles denote supplementary resource sites. (b) Final mycelial structures after a further 2-day growth.

2.4.1.2 Continuous models

The continuous approach is ideal when modeling dense mycelia, such as growth in Petri dishes or on the surfaces of solid substrates. In continuous models, mycelium is viewed in some sense as an average of the individual components, such as biomass density and tip density. Sets of differential equations were derived to represent the interaction of fungal biomass with the growth conditions. In a series of papers, reaction advection models were derived to link the microscopic behavior of hyphae to the behavior of the fungal colony [69, 85, 86]. The variables of these partial differential equations denoted hyphal density,

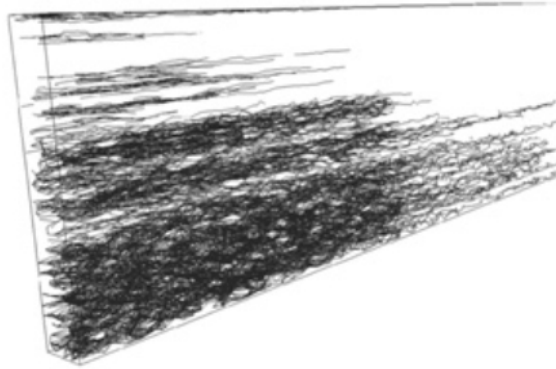


FIGURE 2.14 – Example of hyphal growth in wood simulated by the model in Fuhr *et al.* (2011) [84].

hyphal tip density and substrate concentration. However, in the 2D advection process, the orientation of the tips and the hyphae should be explicitly defined, which augments the mathematical complexity especially in heterogeneous media.

An advanced approach was developed by Davidson (1998) and, Davidson and Olsson (2000) for the development of the fungal mycelium in nutritionally heterogeneous environments [70, 87]. In these models, movement of hyphae is represented by diffusion rather than by advection. The biomass density, the external substrate concentration and the internal substrate concentration were modeled to investigate the interaction of the mycelium with its environment. Both passive and active translocation was considered via reaction-diffusion equations.

More recently, Boswell *et al.* (2002,2003) derived a fungal growth model by combining the work mentioned above [88, 71]. The model in Boswell *et al.* (2003) consists of five variables : active hyphal density $m(\mathbf{x}, t)$; inactive hyphal density $m'(\mathbf{x}, t)$; hyphal tip density $p(\mathbf{x}, t)$; internal substrate concentration $s_i(\mathbf{x}, t)$; and external substrate concentration $s_e(\mathbf{x}, t)$. The interactions between the components of the model are given by a system of advection-diffusion equations, which were obtained through standard mass conservation laws :

$$\frac{\partial m}{\partial t} = |D_p s_i \nabla p + v s_i p \nabla m| - d_a m, \quad (2.1a)$$

change in active hyphae = new hyphae created by tip movement - hyphal inactivation,

$$\frac{\partial m'}{\partial t} = d_a m - d_i m', \quad (2.1b)$$

change in inactive hyphae = hyphal inactivation - hyphal collapse,

$$\frac{\partial p}{\partial t} = \nabla \cdot (D_p s_i \nabla p + v s_i p \nabla m) + b s_i m - f m p, \quad (2.1c)$$

change in hyphal tips = random and directed tip movement + branching - anastomosis,

$$\frac{\partial s_i}{\partial t} = \nabla \cdot (D_i m \nabla s_i - D_a m s_i \nabla p) + c_1 s_i s_e - c_2 |D_p s_i \nabla p + v s_i p \nabla m| - c_4 |D_a m s_i \nabla p|, \quad (2.1d)$$

change in internal substrate = diffusion and active translocation + uptake - growth costs of hyphal extension-active translocation cost,

$$\frac{\partial s_e}{\partial t} = D_e \nabla^2 s_e - c_3 s_i s_e, \quad (2.1e)$$

change in external substrate = diffusion of external substrate - uptake.

$$(2.1f)$$

where D_i , D_a , D_e and D_p denote respectively the coefficient of internal substrate diffusion, internal substrate active translocation, external substrate diffusion and tip diffusion per unit substrate; v , b , f , d_i and d_a represent tip rate, branching rate, anastomosis rate, hyphal degradation rate and hyphal inactivation rate; c_1 , c_2 , c_3 and c_4 are the rate of internal substrate acquisition through uptake, cost of hyphal extension, rate of external substrate depletion through uptake and translocation costs, respectively. The model was calibrated by an experiment of the growth of *Rhizoctonia solani* and some simulated results are shown in Fig. 2.15. Furthermore, based on this model, Boswell (2012) has investigated the competition between two fungal colonies growing into a nutrient-free domain, depending on numerous factors produced by the interaction of the two colonies [89].

2.4.2 Macroscale models

Non-spatial models (0D models) are widely used in simulating the fungal damage of wood and wood-based products. Various models have been established to reflect the influence

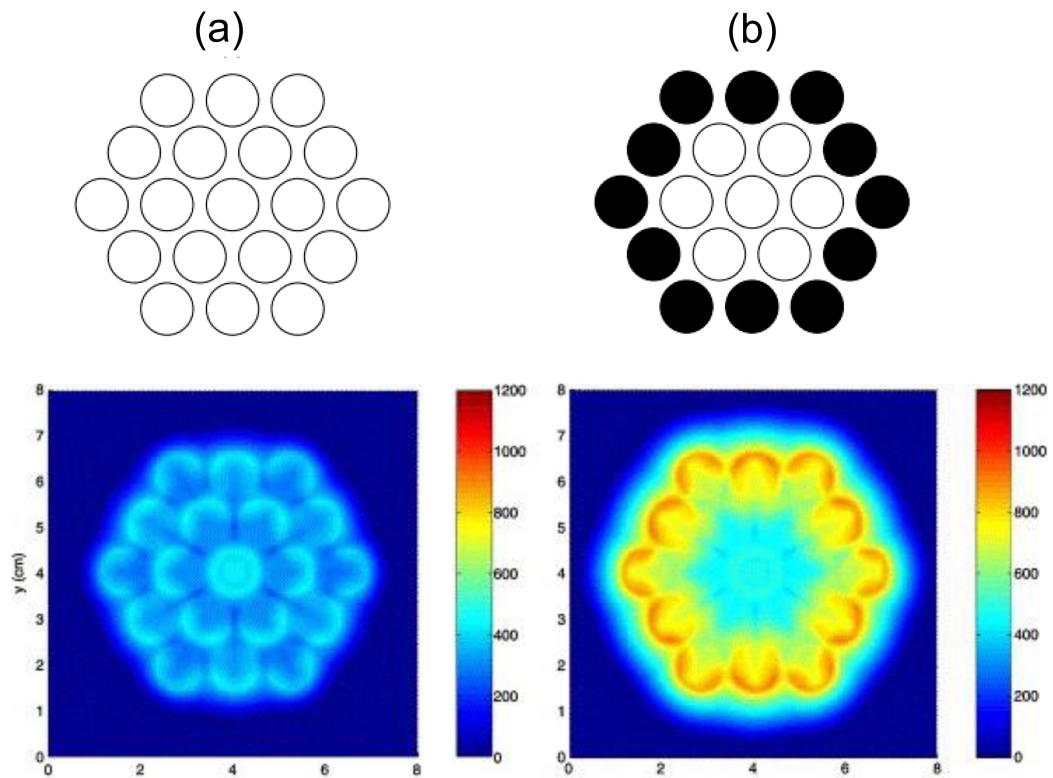


FIGURE 2.15 – Hyphal density (cm hyphae cm^{-2}) distributed in two different tessellations modeled by Boswell *et al.* (2003) [71]. (The black and white discs respectively denote droplets made from glucose-supplemented and unsupplemented agar.)

of fungal decay on the performance of wood under different environmental conditions.

A basic model for timber decay above ground was derived from the field test data to simulate the progress of fungal decay depth in a timber element as shown in Fig. 2.16 [90]. The decay depth was approximated by an idealized bilinear relationship characterized by the decay rate and the duration of a decay lag. The decay rate was assumed to be the product of different factors accounting for the effects of material, construction and environmental conditions, and the decay lag was a function of the decay rate.

Another common approach (i.e., the dose-response model) was proposed for modeling the service life of wooden specimens decayed by brown, white and rot fungi [91, 92]. This approach describes the change on an organism caused by differing levels of doses to a stress effect after a certain exposure time. These models were established on the basis of field tests carried out at different sites in Europe over 3 – 8 years. The daily dose was

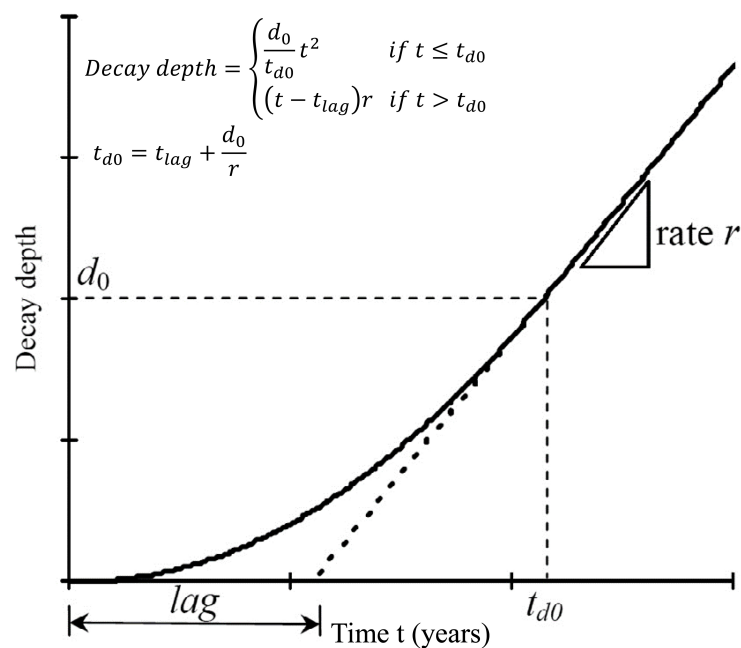


FIGURE 2.16 – Progress of fungal decay depth with time used as the basic model for timber decay in Wang *et al.* (2008) [90].

a function of daily average moisture content and daily average temperature, and the total dose was simply the cumulative sum of the daily dose. The response to the total dose was the mean decay rating. Fig. 2.17 shows the sigmoid curves depicting the logistic regression functions between the dose parameters and the different types of fungal decay rating.

Viitanen *et al.* (2010) [93] used also the dose-response relationship to develop an empirical model for decay of Scots pine and Norway spruce by a brown rot fungus *Coniophora puteana*. This model was based on laboratory test data (i.e., the small samples under constant conditions). The mass loss of wood (WML) caused by fungal decay was expressed as a function of the relative humidity (RH), the temperature (T) and time (t) (Eq. 2.2). One simulated result is shown in Fig. 2.18.

$$WML(RH, T, t) = -42.9t - 2.3T - 0.035RH + 0.14T \cdot t + 0.024T \cdot RH + 0.45RH \cdot t \quad (2.2)$$

Non-spatial growth models can reproduce the decay for different species of wood and wood-decay fungi during a long time period under various climatic conditions as long as the experimental test data exist. However, as the essential decay mechanism is not ta-

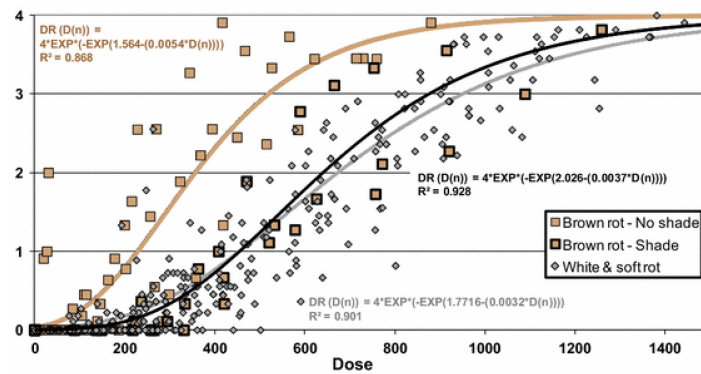


FIGURE 2.17 – Relationship between dose and mean decay rating fitted by field tests data in Bri-schke and Meyer-Veltrup (2015) [92]. The dots represent the field tests data of different softwood species dominated either by brown rot decay and exposed shaded or non-shaded or dominated by white and soft rot decay ; each dot denotes the mean decay rating for one exposure site at a certain exposure time.

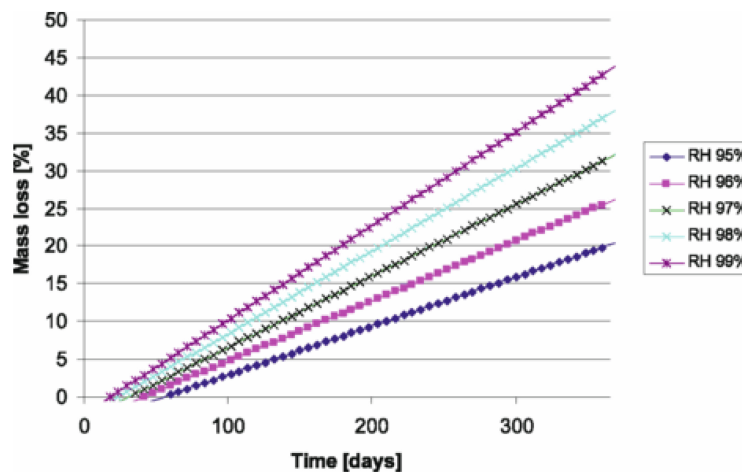


FIGURE 2.18 – The evolution of wood mass loss by fungal decay at different ambient air humidity conditions by Viitanen *et al.* (2010) [93]. Samples are small untreated pine sapwood decayed by *Coniophora puteana* at a constant temperature of 15°C.

ken into consideration, a comprehensive learning database is necessary for each species of fungi and type of wood (the decay in preservative-treated wood is different from the decay in nature wood). This is a constraint in view of the great cost in time for all the measurement.

In consulting the model constructed by Cunniffe and Gilligan (2008) [75], we noticed that the scaling from the mechanistic interpretation of mycelial growth to the macroscale

transmission fungal infection in plants could be realized via a spatial fungal growth model combined with an epidemiological model. A simple reaction diffusion system was used to simulate the spread of mycelial in 1D space depending on the level of nutrients (Fig. 2.19(A)). The cumulative probability of infection of a target host was expressed as a function of the nutrient and the spatial fungal biomass (Fig. 2.19(B)).

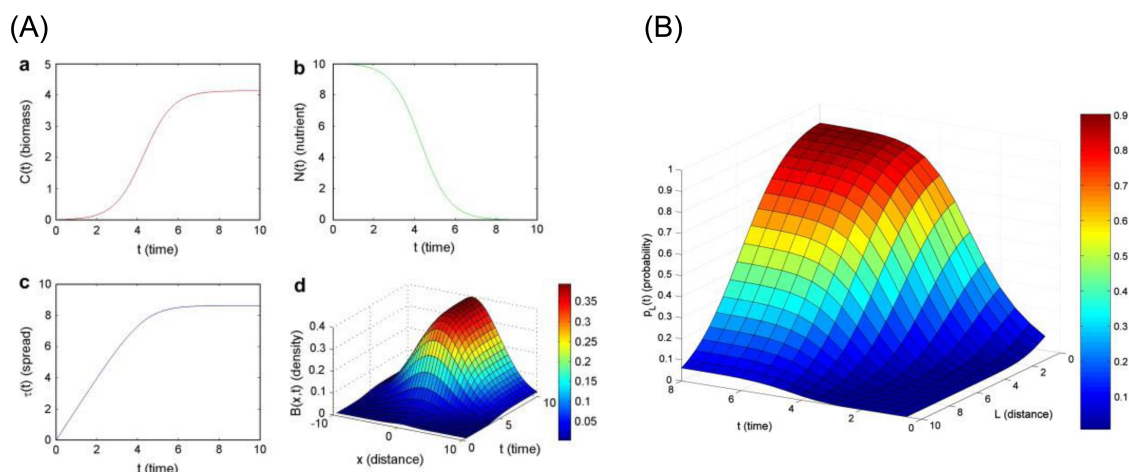


FIGURE 2.19 – 1D spatial fungal growth and the probability of fungal infection modeled by Cunniffe and Gilligan (2008) [75]. (A) (a) Total biomass, (b) level of nutrient, (c) spatial extent of colony and (d) profile of biomass density in 1D space; (B) the probability of infection as a function of initial distance of the fungal inoculum from the host and time.

Although it is still a major challenge to link information across scales, the modeling at the local scale can provide a link between the microscopic behaviors of hyphae and large-scale form of fungal distribution and function. In particular, the discrete models presented explicitly the growth dynamics of hyphae, while the continuous approach can be the key to realize the transition from the local scale to the macro-scale.

2.4.3 Conclusion

In this chapter, we presented a survey of the two main families of scientific tools used for investigating the fungal growth : experimental observation and mathematical modeling. Among the visualization tools, CLSM is an excellent technique for the observation of living fungal specimens with certain thickness in comparing with conventional optical microscopy and electron microscopy. It has been widely used to observe the morphology,

size, internal structure and growth mechanisms of fungi via various fluorescent staining techniques. Nevertheless, there are no publications of a systematic study on quantification of the morphological characteristics of *Postia placenta* at the microscopic scale. In view of the necessity of the growth parameters needed in our fungal growth model, the first step of this thesis work focused on the observation and measurement of the growth parameters of *Postia placenta* in using CLSM.

In terms of fungal growth modeling, the models at two scales have been respectively presented : spatial growth at the colony scale and global development at the macro-scale. Two approaches have been presented at the colony scale : discrete and continuous modeling. The discrete models are divided into two categories, lattice-based and lattice-free modeling. The former possesses a high computational efficiency but constraint the geometrical morphology of the generated mycelium by the lattice. On the contrary, realistic mycelial networks can be obtained with the latter approach, at the price of high computational costs. Alternatively, the mycelium can be also viewed as continuous variables and simulated using partial differential equations. The early models were based on reaction-advection equations. However, in multi-dimensional space, the advection process requires the development direction to be known at each point, which limits the prediction ability of the code and/or augments the mathematical complexity especially in heterogeneous media. Thus, the recent models applied diffusion process instead of the advection one to model the movement of hyphae. At the macro-scale, non-spatial models are widely used in assessing the fungal damage of wood and wood-based products under different environmental conditions. These models were established based on a comprehensive database for each species of fungi and type of wood but not the essential fungal decay mechanisms, leading to a great constraint by the experimental data.

In this work, after the first step of fungal observation, a discrete model has been developed to model the fungal growth at the colony scale using the lattice-based approach. A new algorithm developed for this model eliminates any geometrical restriction of the lattice directions. Therefore, it is able to generate realistic mycelial networks yet keeping the simplicity of lattice models, namely in accounting for complex geometrical shapes. Thanks to experimental observation, the model parameters have been precisely defined via a blend of direct calibration and inverse analysis. By accounting for elongation, branching and anastomosis, it is able to reproduce the intricate coupling between spatial invasion and network densification. Moreover, the tropism mechanism has been also incorporated, which permits the simulation of mycelial growth in complex environments. Then, a

continuous model of fungal development under free growth conditions was derived from the radius biomass density obtained from the validated discrete model. This continuous model was established based on a reaction-diffusion equation, which captured well the front-like progression of hyphal movement. A transition from local-scale to macroscale development of fungi in periodic porous media has been realized via this continuous model. The 1D macroscopic field was averaged from the local field simulated in 2D porous media and was used to derive the macroscale model. In summary, the macroscale model, which was developed step by step from the small-scale hyphal growth mechanisms, possesses a potential of modeling the macroscale development of fungal biomass in porous media.

Chapter3

Experimental observation of the growth of *Postia placenta*

*This chapter describes a method for visualizing the expansion of a colony of *Postia placenta* by staining with a vital fluorescent dye under CLSM. A series of confocal images were obtained during seventeen days for quantification of the morphological characteristics. The growth parameters, which were used to calibrate the discrete model described in Chapter 4, were determined here by statistical analysis. In section 3.2, the materials, including the strain of fungus, the substrate and the culture dish were introduced as well as the methods concerning the culture, the confocal observation and the measurement. Then, the results of the observation and the measurement are shown and discussed in section 3.3. The values of the growth parameters serving the discrete model are listed at the end of the section 3.3.*

•*This work is published in PLOS ONE [94].*

Morphological Characterization and Quantification of the Mycelial Growth of the Brown-rot Fungus *Postia placenta* for Modeling Purposes

Huan Du¹, Pin Lv¹, Mehdi Ayouz¹, Arnaud Besserer², Patrick Perré^{1*}

¹ LGPM, CentraleSupélec, Université Paris-Saclay, 92290, Châtenay-malabry, France

² ENSTIB/LERMAB, University of Lorraine, 88000, Epinal, France

* patrick.perre@centralesupelec.fr

Abstract

Continuous observation was performed using confocal laser scanning microscopy to visualize the three-dimensional microscopic growth of the brown-rot fungus, *Postia placenta*, for seventeen days. The morphological characterization of *Postia placenta* was quantitatively determined, including the tip extension rate, branch angle and segment length, (hyphal length between two adjacent branch sites). A voxel method has been developed to measure the growth of the biomass. Additionally, the tip extension rate distribution, the branch angle distribution and the segment length distribution, which quantified the hyphal growth characteristics, were evaluated. Statistical analysis revealed that the extension rate of tips was randomly distributed in space. The branch angle distribution did not change with the development of the colony, however, the segment length distribution did vary with the development of the colony. The experimental data will be incorporated into a lattice-based model simulating the growth of *Postia placenta*.

3.1 Introduction

Wood is a traditional constructive material in many parts of the world due to its solidity, lightness and sustainability. Nowadays, wood and wood-based products, such as insulating panels, are commonly used to address the two main trends in building designs : the requirements for thermal performance and the use of renewable materials. Nevertheless, wood is easily bio-degraded by insects, fungi and bacteria, resulting in the damage of

lumber structures and the reduction of building service life. Fungi are the primary causes of wood degradation, among which, the most destructive ones are brown rot fungi due to their rapid decaying mechanisms. Throughout Europe and North America, they are the most common wood decay fungi within buildings [4]. Recently, mathematical modeling has aroused great attention in the study of fungi [84, 95], which can forecast the behaviors of mycelial growth under different environmental conditions. Such modeling tools are likely to supplement costly and tedious experimental studies and are indeed absolutely required for service life to be accounted from the design stage. Our team is currently developing a model of fungal growth based on the statistical reproduction of hyphal development. Our assumption is that the same mechanisms will be valid in wood and wood-based products, provided the porous geometry and the nutrients are accounted for via tropisms and/or modification of the growth statistics, such as elongation. Therefore, the first step of our modeling approach, which is the object of the present work, is to supply the model with statistics extracted from growth observations in free conditions (homogeneous medium and absence of resource limitations).

Different techniques have been used to visualize mycelial structure and to quantify its growth characteristics. A series of time-lapse 2D (bi-dimensional) images were recorded to visualize mycelial growth and structures by using photography, image scanner and conventional light microscopy [96, 97, 98, 99]. However, they are obtained with low clarity and limited by sample thickness. Electron microscopy [100, 101, 47] has a large depth of field able to produce images free of focus blur, but samples need to be dehydrated, which results in inactivating living samples and prevents time-lapse observations. Alternatively, confocal laser scanning microscopy (CLSM) allows non-destructive optical sectioning of samples in observing living fungal cells and is used in the visualization of 3D (three-dimensional) structures of fungi at a high spatial resolution, which realizes the quantification of fungal surface area, volume and density allocation [51, 102, 53, 54, 58, 59, 50, 57]. Moreover, in addition to the static visualization of fungi, dynamic observations of hyphal growth have been performed as well [52, 103].

Postia placenta is one of the most common brown rot fungi found in wood that is currently in service [10, 11, 12]. It decays wood at a rapid pace by degrading cellulose and hemicelluloses using self-produced enzymes and hydroxyl radicals, leaving lignin in place [104, 42, 105, 106]. Apart from the biochemical aspect, the environmental factors, (e.g., temperature, moisture content, and oxygen depletion), that influence its growth rate in wood, have also been studied [14, 15, 16]. However, to our knowledge, there are

no publications reporting the visualization of mycelial structures and quantitative measurement of growth characteristics of *Postia placenta* at the microscopic scale.

The objective of this work is to visualize *Postia placenta* and evaluate its morphological characteristics to produce a set of statistical functions able to feed a lattice-based model for simulating a free growth (without restriction of resources, like nutrients or growth space) of mycelium in a homogeneous environment. Thus, the observations on the free-grown culture were performed using CLSM during 17 days. 3D images and their 2D projection images were obtained in order to quantitatively measure and analyze the morphological and growth parameters of *Postia placenta*, such as tip growth rate, hyphal density, branch angle and branching location. Then, the mycelial growth in complex environments, such as porous morphologies and resource limitation, will be extended from the calibrated model. The simulation work based on the statistics derived in the present work will be the object of a full paper.

3.2 Materials and methods

3.2.1 Materials

Postia placenta strain FPRL 280 and a media of malt extract agar (No.X923.2, Carl Roth) at a concentration of 33.6 g/L was used. Teflon culture dishes, with an internal height of 5 mm and inner-radius of 7.5 mm, covered by glass coverslips with a thickness of 0.14 mm were designed for the observations using confocal microscopy. Vacuum grease (Carl Roth), which is non-toxic to fungi, was applied at regular points along the circumference of culture dishes to fix coverslips.

3.2.2 Methods

3.2.2.1 Inoculation and culture

750 μ L malt extract agar was added into the culture dish to obtain a \sim 4.2 mm-thick media. To avoid the contact of the suspension with the coverslip and to reduce the amount of small hyphal fragments in the inoculation, 5 μ L of the suspension, (*Postia placenta* strain FPRL 280 mixed in sterilized water), was inoculated on the media. Several drops of the

vacuum grease were put on the edge of the culture dish to fix the coverslip, which allowed sufficient oxygen supplies and, simultaneously, reduced the risk of contamination. Then the culture dish was kept in an incubator at 20°C for 72 hours before observations. Another ten cultures were prepared as controls at the same time and maintained at 20°C for one month. The mycelial growth in 2D began to be restricted by the surface of the culture dish after two-week growth. Then, the colonies regained rapid growth in the z direction thereafter till one month. This proves that the nutrients in media were sufficient at least for one-month growth of *Postia placenta*.

3.2.2.2 Fluorescence staining

Calcofluor White M2R (Fluorescent Brightener 28, Sigma Aldrich), which stains fungal cell walls, was prepared as a 0.1%(w/v) stock solution in distilled water. In each staining, the stock solution was diluted to 0.001%(w/v) and was added into the culture by syringe filter (0.2 μm). After 5 minutes, the dye was rinsed away gradually with sterilized water. The low concentration of the dye and short time of staining allowed for normal growth of hyphae [107] and, simultaneously, few residues of the fluorescent dye remaining in the media. The staining was repeated every 4 or 5 days to ensure a high signal-to-noise ratio while keeping low laser power, because the fluorescence intensity fades when exposed to the wavelength of 405 nm (the selected laser line).

3.2.2.3 Confocal observation

Observations were performed at room temperature ($\sim 20^\circ\text{C}$) during 17 days using a Zeiss LSM 700 Laser Scanning Confocal Microscope (CLSM). The UV diode laser, at a wavelength of 405 nm, was used for illumination. Fluorescence of Calcofluor White M2R was captured through a band pass filter at a wavelength of 420 – 475 nm. The sample was evaluated every 2-3 days. A Plan-Apochromat 10 \times /0.45 M27 objective lens was used to obtain the image, and each image was averaged across 4 scans. Since the medium was transparent and the dyes transferred to the penetrative hyphae, the whole colony could be visualized, including the surface and penetrative hyphae, (Fig. S3.2(a)). As the mycelium developed, the sizes of digital images in the x - y plane increased from approximately 4000 $\mu\text{m}\times 4000 \mu\text{m}$ to 9000 $\mu\text{m}\times 9000 \mu\text{m}$. Pixel size in the x - y plane was 1.25 $\mu\text{m}\times 1.25 \mu\text{m}$ to be able to visualize the individual hyphae, as the hyphal diameter was greater than 2 μm . The depth on the z -axis was approximately 600 μm and the interval distance between every

two adjacent x - y slices was approximately $20\ \mu\text{m}$. A 3D image was obtained through reconstructing the successive x - y slices in each observation (partly shown in Fig. S3.2(b)). A 2D projection image was obtained as well for each observation using the method of maximum intensity projection (MIP) [108], which consists of projecting the voxel with maximum intensity on every view throughout the volume onto a 2D image (Fig. S3.3). By using MIP of the color-coded slices, color projections were also generated to distinguish the hyphae at different depths.

3.2.2.4 Measurement and analysis

Optical slices in each 3D image were converted to binary masks using the triangle threshold method. The background noise caused by residual dyes was reduced by a selective median filter in ImageJ (NIH, Bethesda MD). In each 3D image, the number of voxels that contain hyphae in all slices were counted and plotted as a function of time to illustrate the evolution of biomass growth.

Tip extension length, (Δl_p), was measured and obtained by comparing the same hypha in the overlapped two 2D projection images of consecutive observations using ImageJ (Fig. S3.4). The tips were classified into two categories : active tips ($\Delta l_p > 0$) and dormant tips ($\Delta l_p = 0$, defined as temporal non-extending tips which can regain the activity). The hyphae that could be visually discriminated were measured. The extension rate for each tip, as well as the average extension rate of the active tips on each image, was calculated using Eq. (3.1) and Eq. (3.2) :

$$R_p(i; x, y) = \frac{\Delta l_p(i; x, y)}{\Delta t}, \quad (3.1)$$

$$\langle R_p \rangle = \frac{1}{N_{ap}} \sum_{i=1}^{N_{ap}} R_p(i), \quad (3.2)$$

where $R_p(i; x, y)$ ($\mu\text{m}/\text{h}$) is the extension rate of tip i and the coordinates (x, y) are its position. $\Delta l_p(i; x, y)$ denotes the extension length of tip i when it reaches (x, y) in the interval of time Δt . $\langle R_p \rangle$ is the average tip extension rate and N_{ap} is the number of active tips. The distribution of tip extension rate for each image was calculated by Eq. (3.3) :

$$f(x_k) = \frac{n_k}{n_t \Delta x}, \quad (3.3)$$

where x is the data to be classified (in this case the tip extension rate, R_p , was the sample data); n_k the number of data in the k^{th} interval $[x_k - \Delta x/2, x_k + \Delta x/2)$; n_t the sample size and Δx the width of the interval; $f(x_k)$ the probability density of x falling within the k^{th} interval. Moreover, the quantities of new emerged branches per hypha, as well as, the ratio of active tips from the measured tips were quantified for each image.

Due to the linear and radial growth of hyphae, the biomass of mycelium depends on the total length of hyphae not the area of colony. Thus, three regions, (R1, R2 and R3), with equal gap were successively divided covering almost the entire colony on the 5th, 7th and 10th day following inoculation (Fig. 3.1(a)). The selected regions were rectangular, which was more suitable for image processing but not ideal for measurement because of the radial growth of the colony. Therefore, four portions were selected in each region for quantitative comparison (Fig. 3.1(b)(i)), which allowed that the areas analyzed for each region were proportional to the radius. The shape and position of each portion chosen in the same region was representative of an "average" distance to the inoculum. In 3D images, the hyphal voxels of every four portions in each region were counted and normalized by the total number of voxels of all portions in the final observation. The data of each region was then plotted as a function of time. Curves from R2 and R3 were translated along the time axis to coincide with that of R1. The age of R1 was defined as the duration of the development of the colony since the inoculation, while the age of R2 and R3 was obtained by an age gap through this translation.

There are two types of hyphal branches, the apical branch (AB) and the lateral branch (LB), each distinguished by their formation patterns [28] (Fig. 3.1(b)(ii)). The AB emerges from a hyphal tip and two daughter branches develop symmetrically around this tip. Moreover, the LB is a new branch formed from a site distal to the hyphal tip. Accordingly, there are two types of branch angles and branch sites based on these types of branches. An AB angle is formed by two ABs and a LB angle is defined by the LB and the growth direction of the mother hypha. The location of branch development is denoted as one branch site, differing from a cross that is the intersection of two hyphae at different depths (Fig. 3.1(b)(ii)). Moreover, the segment length is defined as the hyphal length between the two adjacent branch sites. Next, the two types of branch angles, the number of AB sites and LB sites and the segment length were quantified and measured in each region from color projection images using the proprietary Zeiss software (ZEN 2012, black edition). The distributions of two branch angles, as well as, segment lengths were calculated using Eq. (3.3) where the measured branch angle θ and segment length l were the sample

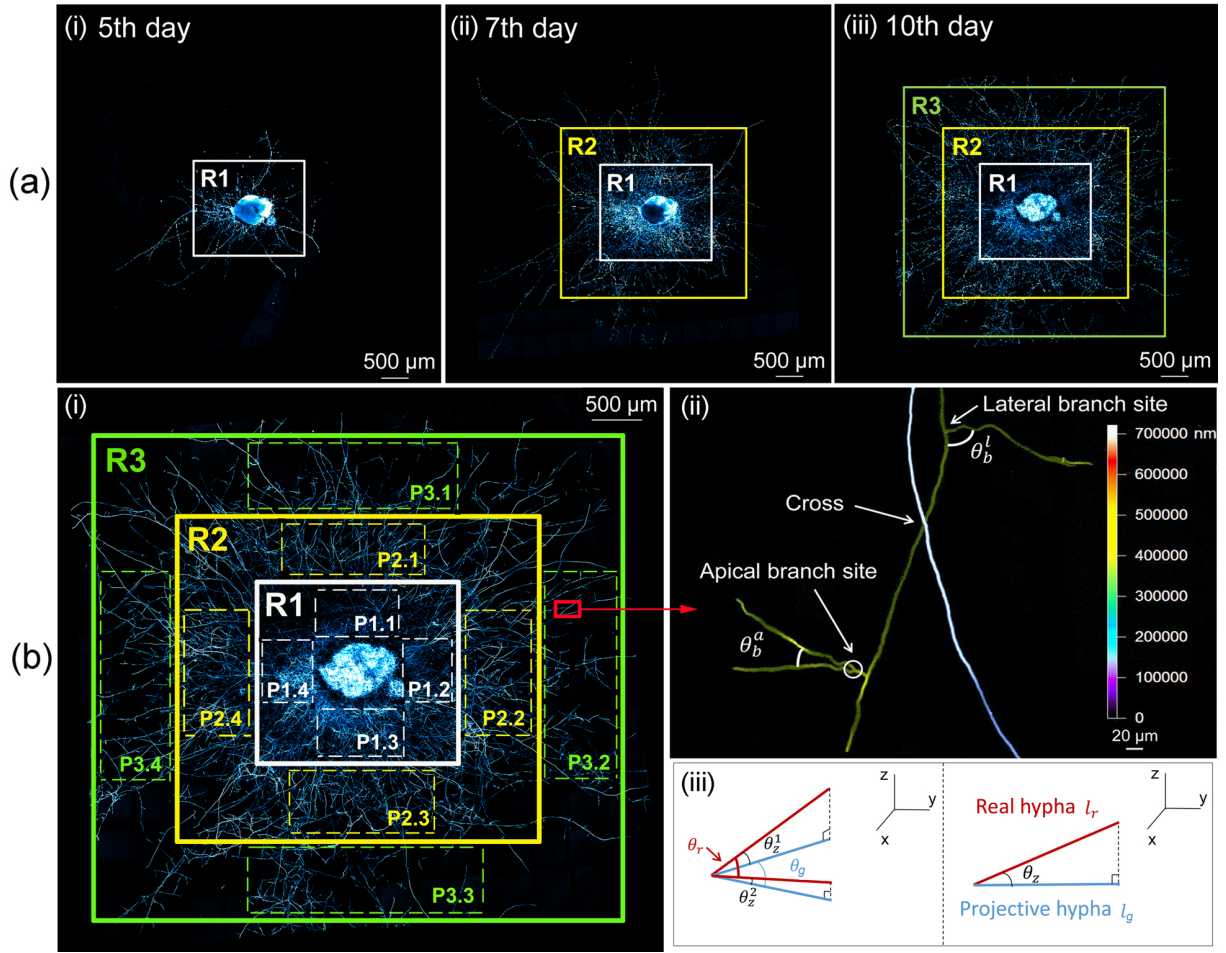


FIGURE 3.1 – Method of the measurement of branching characteristics. (a) Three regions with equal gap to partition the young and old hyphae : (i) R1, (ii) R2 and (iii) R3, covering almost the entire colony on the 5th, 7th and 10th day following inoculation. (b) (i) Four portions selected for the measurement in each of the three regions (e.g., P1.1, P1.2, P1.3 and P1.4 in R1). (ii) Zoom of a color projection for measurement to show a cross of two hyphae with two types of branch sites and branch angles (AB angle (θ_b^a) and LB angle (θ_b^l)). The color bar shows the depth of the mycelium along the z -axis. (iii) Errors between real values and projective ones caused by z -direction growth of hyphae : (left) real branch angle (θ_r), projective branch angle (θ_g), and angle of the real hypha to the x - y plan (θ_z); (right) real branch length (l_r) and projective branch length (l_g).

data. Due to the projection in 2D of the real 3D structure, an error is possible for some of the measured branch angles and segment lengths. The projection error due to the z -component of the hyphal direction is shown in Fig. 3.1(b)(iii). This error was calculated using Eq. (3.4) and Eq. (3.5) :

$$\epsilon_\theta = \theta_r - \theta_g = \arccos(\sin\theta_z^1 \sin\theta_z^2 \cos\theta_g + \cos\theta_z^1 \cos\theta_z^2) - \theta_g, \quad (3.4)$$

$$\epsilon_l = \varphi_l \times l_g = (1/\cos\theta_z - 1) \times l_g, \quad (3.5)$$

where ϵ_θ is error of angle; θ_r real branch angle; θ_g projective branch angle; θ_z angle between real hypha and the x - y plan, calculated by $\arctan(\Delta z/\Delta l)$; ϵ_l error of length; φ_l error coefficient, which was defined as the ratio of the error of length to the projective length; l_g projective segment length. Due to the color projection, the distance of z -direction growth (Δz) and the corresponding projective distance (Δl) can be measured and used to estimate θ_z .

3.3 Results and discussion

3D images were reconstructed from confocal slices, which allowed the calculation of the growth of the biomass. 2D projection images were also used to observe the mycelial growth and to measure its morphological characterization. As shown in Fig. S3.3, the *Postia placenta* grew from a central inoculum block and 8 instants were recorded on the 3rd, 4th, 5th, 7th, 10th, 12th, 14th and 17th day, following inoculation. During the initial 5 days, the hyphal elongation was dominant, while on the 7th day, a visible emergence of branches occurred. Next, a symmetric colony formed and enlarged its area by tip extension, as well as branching. After the 14th day, the colony nearly reached the edge of the culture dish and could not continue to increase its area. Overall, the colony remained radially symmetric as it developed over time. Additionally, the mycelial surface density increased over time at a given location but with a distinct spatial gradient as the density decreases with the colony radius. This phenomenon is consistent with the fractal nature of mycelial growth [109, 110].

Biomass growth is a global index used to represent the status of mycelial growth. In Fig. 3.2, the biomass growth is presented as a function of days post inoculation. The curve exhibits a lag phase of 5 days, during which the biomass growth was not considerable. The mycelium may be adapting and exploring the new environment and inducing its transport systems. The exponential phase began on the 5th day, when a rapid multiplication of hyphae occurred. As hyphal branches were initiated, the hyphae extended to the uncolonized regions and the increase of biomass exponentially increased. A stationary phase occurred after the 14th day, as evidenced by a gradual decrease of growth, potentially due to the limited planar space.

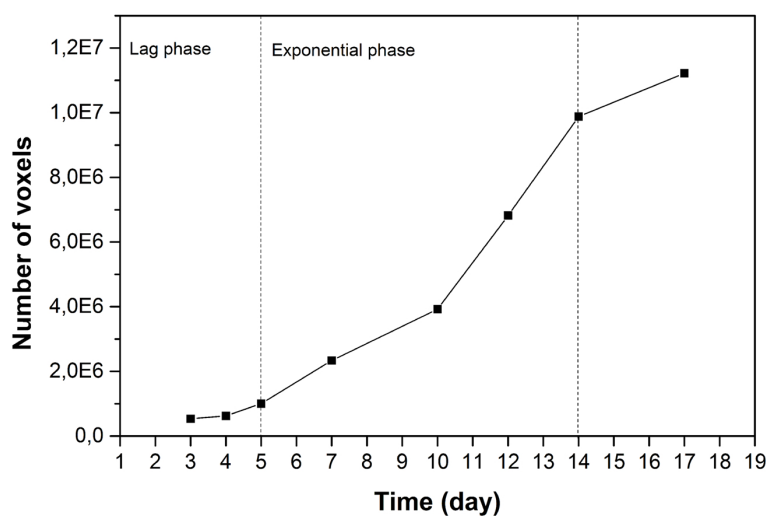


FIGURE 3.2 – Biomass growth of the whole colony as a function of days post inoculation.

The morphological characterization of mycelia, including the tip extension rate and the branching parameters, was obtained by image processing and subsequently analyzed. The number of measured tips (N_p) in each overlapped image is shown in Table 3.1. The average proportion of active tips (k_{active}) over all measurements was estimated as 0.72 and 0.70 during the lag and the exponential phase. And during the exponential phase, this proportion was high (0.77) from the 5th to the 12th day, and then decreased to 0.5 because the hyphal density became very high and a part of the tips approached the edge of the culture dish. The average extension rate of the active tips ($\langle R_p \rangle$) between two consecutive observations are also listed in Table 3.1 together with the new emerged branch number per hypha (φ_{br}), which is the increment of branch number (ΔN_{br}) over the number of tips (N_p). φ_{br} arose rapidly from 0.3 to 2.6 on the 7th day, then decreased to 1.8 and remained at this level for 7 days. The ratio (k_{lag}) of the average value of φ_{br} during the lag phase to that during the exponential phase is 1/5. Thus, although the average proportion of active tips was slightly higher in the lag phase, the increase of biomass was not so high just because there were much fewer new tips (generated by emerged branches) in the lag phase than in the exponential phase. The peak of the the average tip extension rate coincides with that of new emerged branch number per hypha (φ_{br}). It increased rapidly between the 5th and 7th day from $16.6 \mu\text{m}/\text{h}$ to $28.8 \mu\text{m}/\text{h}$, then decreased to around $14 \mu\text{m}/\text{h}$ until the 14th day. From the 14th day, it decreased much lower. As a result, the tip extension rate and the branching emergence rate are both tied to the mycelial growth phase. Throughout the lag phase, tip extension dominated and few branches emerged, as also reported by J. Meletiadiis *et al.*, 2001 [111]. Following the lag phase, both activities contributed to

the rapid multiplication observed on day 7. Then, the average tip extension rate and the branching emergence rate remained nearly constant, which resulted in the continuance of the exponential phase until the 14th day.

TABLE 3.1 – Average tip extension rate obtained using Eq. (3.2) and relative increase of branch number per hypha during two consecutive observations.

Days after inoculation	3	4	5	7	10	12	14	17
Number of measured tips (N_p)	–	86	119	132	144	150	190	224
New emerged branch number per hypha φ_{br}	–	0.3	0.3	2.6	1.8	1.4	1.4	0.9
Average extension rate of active tips $\langle R_p \rangle$ ($\mu\text{m/h}$)	–	11.4	16.6	28.8	15.5	12.7	13.9	5.3

Although the average tip extension, (calculated by Eq. (3.2)), provides a global view, it cannot absolutely represent the tip extension rate because of the important deviation of individual values from the average. Indeed, individual values are spread over a wide range as shown by the distributions, calculated by Eq. (3.3), in Fig. 3.3. Fig. 3.4 depicts the spatial distribution of tip extension rate calculated by Eq. (3.1) during the 17 days. The green points represent the rates smaller than $25 \mu\text{m/h}$, while the orange ones represent the higher rates. The green and orange points are randomly distributed over the entire domain, which indicates that the tip extension rate is randomly distributed in space. Therefore, the formation of the colony generally presents a radial symmetry over time, despite the irregular form of the inoculum. The fact that the extension rate of the same tip varies randomly with time has also been reported by Sampson K., 2003 [112].

As shown in Fig. 3.5(a), the biomass growth in each region displayed a similar trend. The curves of R2 and R3 were translated by -2 days and -4 days along the time axis, respectively. Following translation, the three curves are nearly superimposed, which reveals that the biomass behavior in the three regions is similar (the inset graph in Fig. 3.5(a)). Fig. 3.5(b) illustrates the age of each region. The estimated starting time of hyphal growth in the three regions was 0, 2 and 4 days following inoculation. Thus, Fig. 3.5(b) serves as an age axis for Fig. 3.5(a).

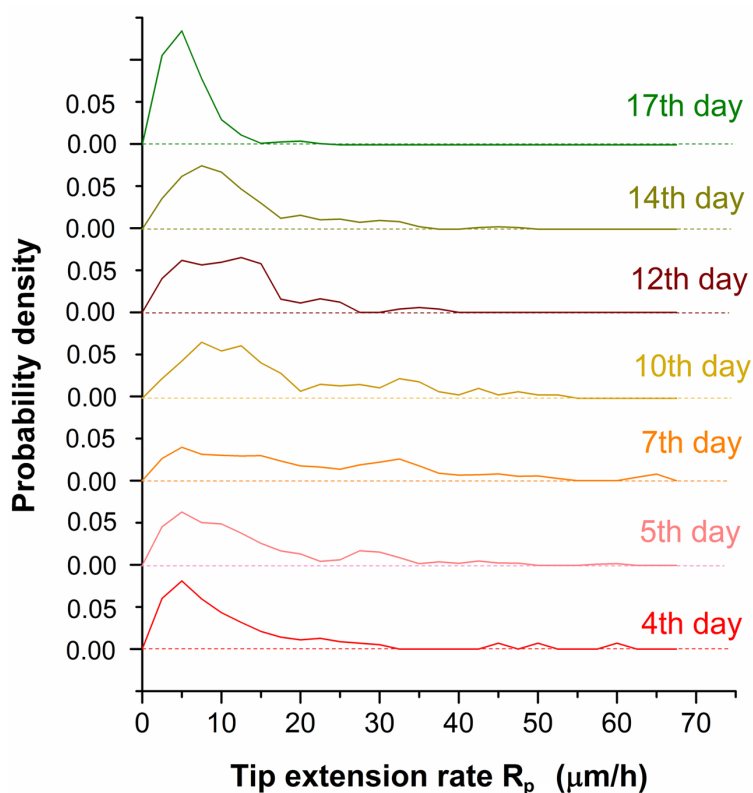


FIGURE 3.3 – Distribution of the extension rate ($R_p(i; x, y)$) of active tips calculated during two consecutive observations. Different observations are displayed from the 4th to 17th day post inoculation.

An additional important branching parameter to simulate the hyphal morphology is the branch angle. AB and LB angles were measured in the four portions of R1, R2 and R3 in the 12th-day observation. The population of the angle sample is approximately 1200, including ~ 400 , ~ 500 and ~ 300 data measured respectively in R1, R2 and R3, among which there were ~ 960 LB angles and ~ 240 AB angles. A comparative plot of the AB angle distribution and the LB angle distribution in all three regions (Fig. 3.6(a)) reveals that the type of branches has negligible effect on branch angle distribution. Fig. 3.6(b) exhibits a similar branch angle distribution in R1, R2 and R3. According to Fig. 3.5(b), these three regions on the 12th day were 12, 10 and 8 days old, which indicates there are no visible differences in the branch angle distribution at different ages of region. Alternatively, it is not influenced by different hyphal densities or by the age of the mother hypha from which the new branches emerged. Overall, the branch angle distribution of *Postia placenta* is not affected by the age of region, or by the branch type. The branch angle remained approximately 80° , close to a right angle, which appeared to maximize

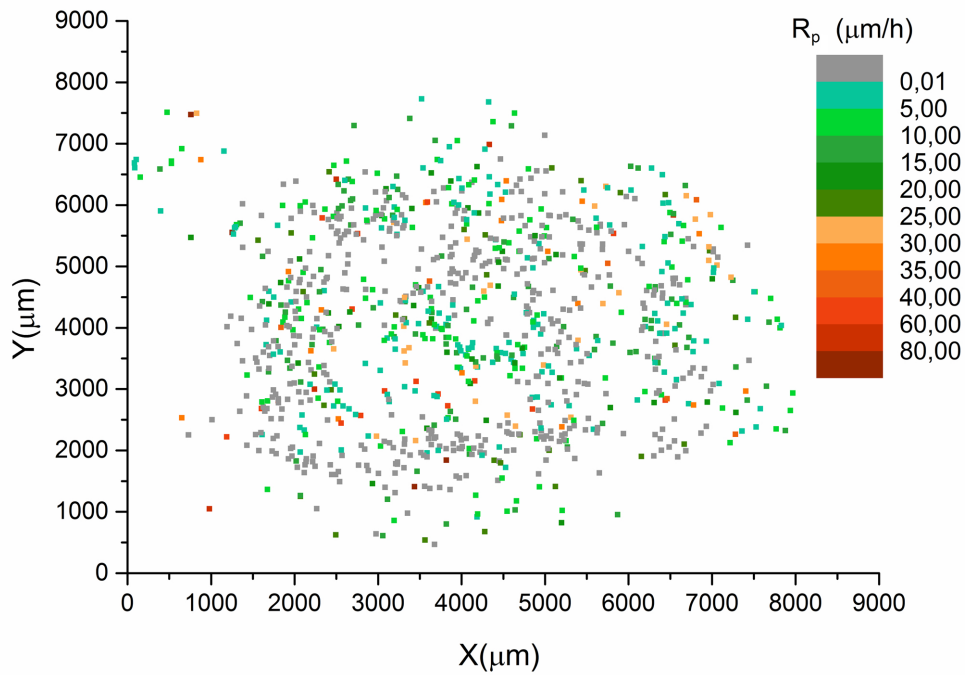


FIGURE 3.4 – Spatial distribution of tip extension rate ($R_p(i; x, y)$) during 17 days of observations. (x, y) are the coordinates of the position of tip i . The colors display the different ranges of rate : from green, less than $25 \mu\text{m}/\text{h}$, to orange for the $> 25 \mu\text{m}/\text{h}$. Grey points represent dormant tips.

the area covered by the colony. The error of the branch angle between the real value and projective value caused by the z -direction growth of hyphae calculated by Eq. (3.4) was shown in Fig. S3.5(a). Considering around 200 errors out of 1200 angles in total, there are only 10 absolute errors greater than 5° , (0.8% of 1200 measured data and the relative error is 6.3% by the average of angles $- 80^\circ$), and 46 greater than 2° , (3.8% of 1200 measured data and the relative error is 2.5% by the average of angles $- 80^\circ$). As a result, we can assume that the error of the angle did not impact the branch angle distribution. The curve fitting was then implemented to the probability density of all measured angles (AB and LB angles in all three regions) using an evolutionary algorithm to minimize the residual sum of squares (RSS) (Eq. (3.6)) between the experimental data and the Gaussian distribution. RSS is defined as :

$$RSS = \sum_k (f(x_k) - g(x_k))^2, \quad (3.6)$$

where x_k is the k^{th} explanatory variable, $f(x_k)$ is the k^{th} value of the probability density calculated from the experiment and $g(x_k)$ is that of the fit. The normalized Gaussian function

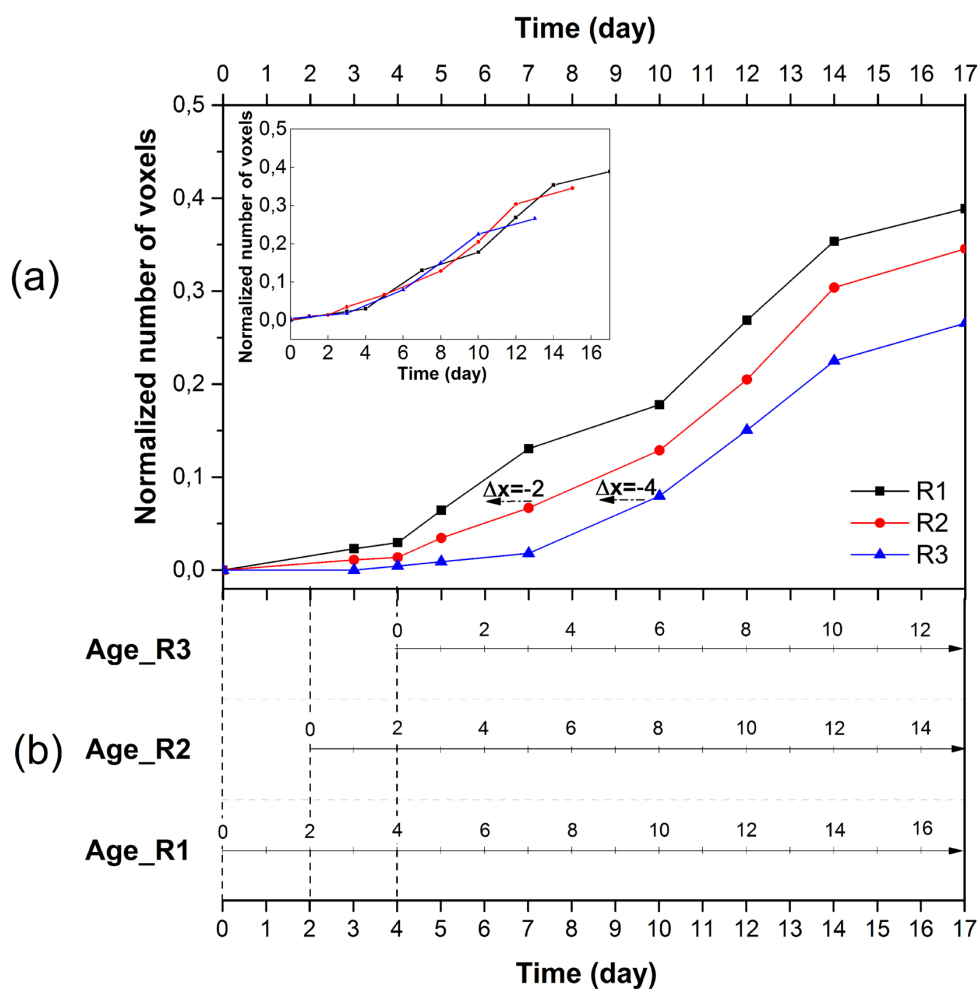


FIGURE 3.5 – Age of region for R1, R2 and R3. (a) Biomass growth measured throughout the 4 portions of R1, R2 and R3 as a function of days after inoculation (the inset graph shows the three curves translated by Δx). (b) The starting time of growth for R1, R2 and R3 is the inoculation day, the second day and the fourth day. The age axis is related with time axis to determine the age of each region on different observation days (e.g., the age of R1 on the 12th day is 12 days old but 10 and 8 days old for R2 and R3; the R1, R2 and R3 are 10 days old respectively after 10 days, 12 days and 14 days.) The age of region represented approximately the age of the oldest hyphae in that region.

reads as follows :

$$g_s(\theta; \mu, \sigma) = \frac{1}{\sigma \sqrt{2\pi}} \exp\left(-\frac{(\theta - \mu)^2}{2\sigma^2}\right), \quad (3.7)$$

where θ represents the branch angle, $\mu = 77.6^\circ$ the mean of the distribution and $\sigma = 12.3^\circ$ the standard deviation. According to the fit, more than 68% of the branch angles were within the interval : $\theta \in [65^\circ, 90^\circ]$. The accuracy of the fit was measured by RSS, which

characterized the global quality of the fit. Fig. 3.6(c) illustrates a low RSS of 5×10^{-5} , which represents strong agreement between the experimental data and the fit. Eq. (3.7) with the identified parameters will be applied in the modeling of mycelial growth to determine the formation of AB and LB angles.

In addition to branch angle, the segment length distribution, which is required to obtain the density of branches, is a complementary parameter to describe the branching pattern. The two types of branches were not distinguished while measuring the length, however, the number of LB sites (N_b^l) and AB sites (N_b^a) were additionally counted. The ratio of N_b^l/N_b^a decreased rapidly as a function of time and subsequently leveled off and remained between 4.0 and 5.0 from the 7th day. The segment length distribution is shown in Fig. 3.7(a) and each sample possessed a population of 300 to 500. The most frequent values were approximately $15 \mu\text{m}$ to $25 \mu\text{m}$, regardless of the age of the region. Their proportion increased with the age of the region. Indeed, as more branches appeared with time, a long segment length was divided into segments and produced several short lengths. The proportion of short lengths increased, while that of long ones decreased with time. As shown in Fig. 3.7(a), few segments were longer than $200 \mu\text{m}$. Due to their very low probability, these long segments were not clearly visible and their evolution with age was difficult to distinguish. Yet, their importance in terms of biomass and morphology of the mycelium is important. For this reason, a weighted cumulative distribution function (Fig. 3.7(b)) was defined to better consider the influence of the long segments :

$$F(l_m) = \frac{\sum_{k=1}^m f(l_k)l_k}{\sum_{k=1}^{m'} f(l_k)l_k}, \quad (3.8)$$

where f is the probability density shown in Fig. 3.7(a); l_k the length of the k^{th} interval; m the number of the interval to be calculated and m' the total number of the intervals. The comparison of the segment length distributions was performed among the same region (R1) of different days, among the three regions of the same day (on the 12th day) and among the regions of the same age (10-day-old). In Fig. 3.5(b), the age of the regions on different days can be identified. Fig. 3.7 (a)-(i), (a)-(ii) and (b)-(i), (b)-(ii), a comparison between the regions of different ages, indicate that with the increasing of age, the proportion of short segment lengths arose while that of long ones reduced. It reveals that the branches emerge not only from young hyphae but also from the old parts of hyphae, and that the branch sites can be located both in the parts with low and high branch density. The coincidence of the three curves in Fig. 3.7(a)-(iii) and (b)-(iii) illustrates that

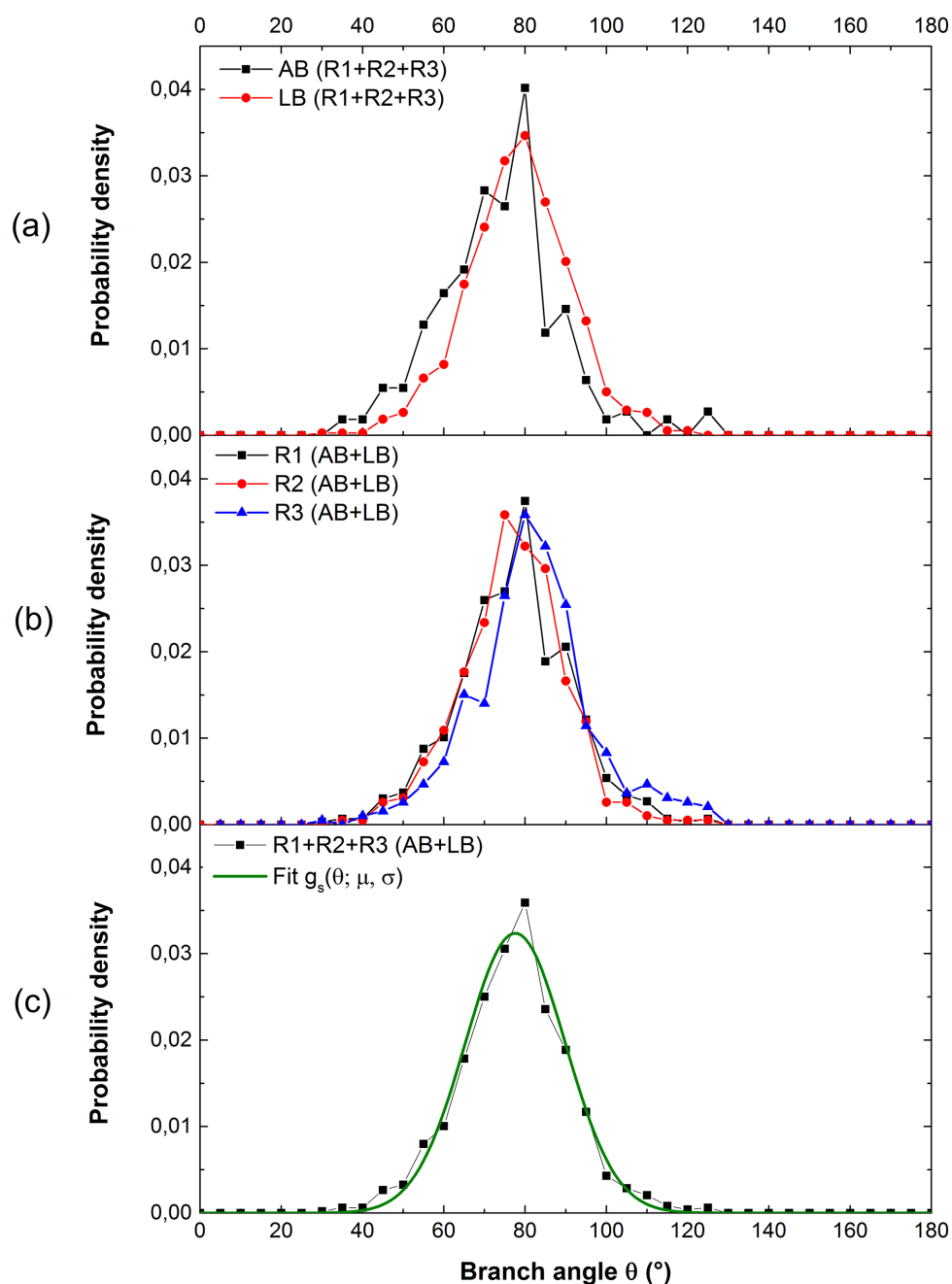


FIGURE 3.6 – Distribution of branch angle measured in the observation on the 12th day. (a) AB angles and LB angles in three regions; (b) two types of branch angles respectively in R1, R2 and R3; (c) two types of branch angles in three regions and fitted curve. The similar branch angle distributions were observed in each of the different regions and they follow a Gaussian distribution.

the segment length distributions are approximately equal at the same age of the region. The error coefficient of segment length calculated by Eq. (3.5) was shown in Fig. S3.5(b).

Considering the 240 errors out of about 1200 segment lengths in total, there are 82 relative errors, (6.8% of 1200 measured data), greater than 5.0%. Thus, this error can be also neglected for the segment length distribution. Experimental data measured at the same age were regrouped to calculate the segment length distribution (Fig. 3.8). The parameter identification was carried out to the segment length distributions at different hyphal ages. Fig. 3.8 displays examples of fitted curves using a gamma distribution :

$$g_{\gamma}(l; \alpha, \beta) = \frac{\beta^{\alpha}}{\Gamma(\alpha)} l^{\alpha-1} e^{-\beta l}, \quad (3.9)$$

where l is the length between two adjacent branch sites ; α and β are the scale and rate parameters of the gamma distribution. The low value of RSS, about 10^{-5} , indicates a tight fit of the simulated data to the experimental ones. The fitted curves, which are in good agreement with the observation curves, will be used to simulate all the hyphal branching at the corresponding ages of region. The values of the scale and the rate parameter are shown in Table 3.2 : the values of α are between 1.0 and 2.0 while those of β are less than 1.0, and increase when the branching age increases.

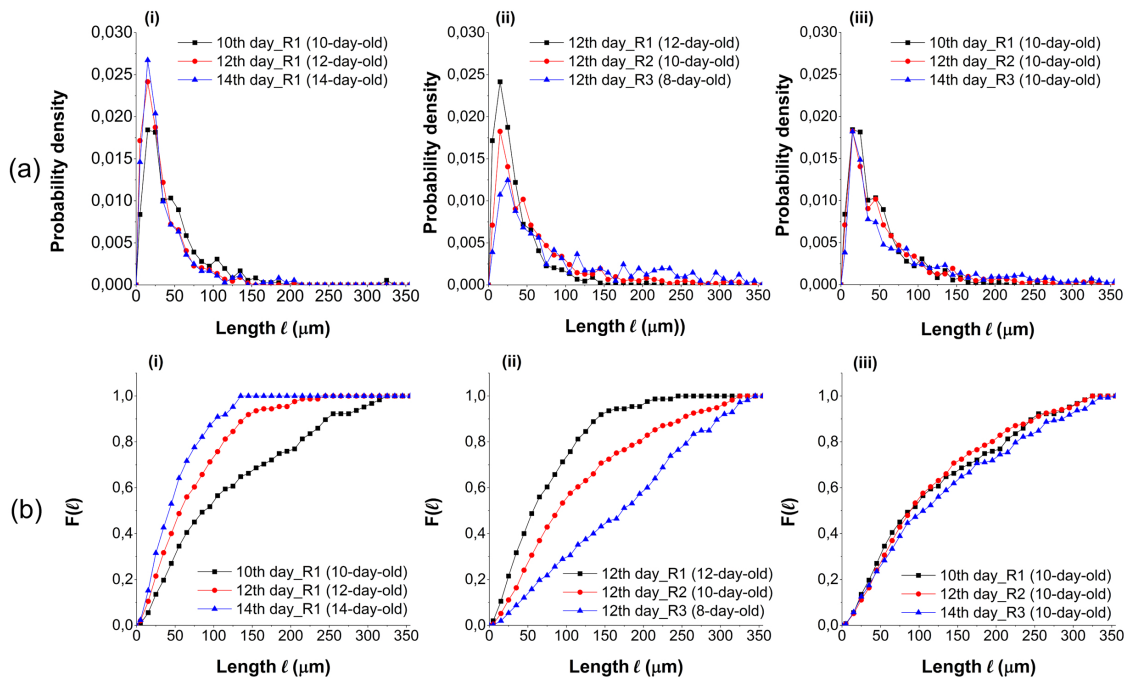


FIGURE 3.7 – (a) Segment length distribution and (b) the corresponding weighted cumulative distribution $F(l)$. The different graphs depict (i) the same region on different observation days, (ii) the different regions on the same observation day, (iii) the distributions of different ℓ regions on observation days selected to have the same hyphal age.

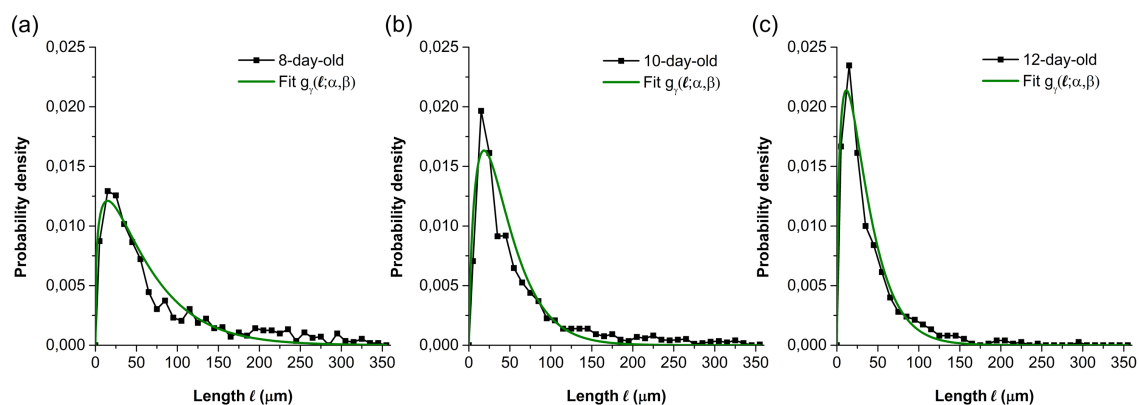


FIGURE 3.8 – Segment length distributions at different hyphal ages and their fitted curves. (a) 8-day-old (experimental data from R2 on the 10th day and R3 on the 12th day); (b) 10-day-old (experimental data from R1 on the 10th day, R2 on the 12th day and R3 on the 14th day); (c) 12-day-old (experimental data from R1 on the 12th day and R2 on the 14th day).

The identified parameters and their values that will be used for calibrating the model for simulating the mycelial growth are listed in Table 3.2. The proportion of active tips (k_{active}) and the tip extension rate distribution ($f(R_p)$) quantify the tip extension, while the branch angle distribution ($f(\theta)$), the ratio of N_b^l/N_b^a and the segment length distribution ($f(l)$) determine the branching pattern. In addition, the lag phase and the exponential phase are distinguished in assigning different values to k_{active} and k_{lag} in the further simulation due to the noticeable difference of hyphal growth.

3.4 Conclusion

The live-cell imaging using CLSM described in the present work allows recording the evolution of the mycelial structure of *Postia placenta* with time. Thanks to the observations on the whole colony level, the growth characteristics can be statistically analyzed in relation with the different duration of the development of the colony. The determination of the age of different regions implies the equivalence of time and space (radius of the colony) in mycelial growth. The data analysis allows a full set of statistical expressions to be proposed to characterize the fungal growth in free growth conditions. Among interesting results, the statistical analysis shows that the hyphal growth presents certain randomness, such as the spatial distribution of tip extension rate and the selection of the branch site. Afterwards, all the quantified hyphal growth reported in this paper will be used to feed

TABLE 3.2 – Description and values of the identified parameters to be applied in the simulation of the mycelial growth.

Parameter	Description	Value & expression
\bar{D}_h^a	Average diameter of hyphae	$3 \mu m$
k_{active}	Proportion of active tips	<ul style="list-style-type: none"> • Lag phase : 0.72 • Exponential phase : 0.7
$f(R_p)^b$	Tip extension rate distribution	$\Gamma(\alpha = 1.51, \beta = 0.09) + 4.65 \times 10^{-6}(R_{pmax} - R_p)$
k_{lag}	Ratio of emerged branch numbers per hypha during the lag phase to that during the exponential phase ($[\varphi_{br}]_{lag}/[\varphi_{br}]_{exp}$)	1/5
$f(\theta)$	Branch angle distribution	$\mathcal{N}(\mu = 77.6^\circ, \sigma = 12.3^\circ)$
N_b^l/N_b^a	Ratio of the number of LB sites to that of AB sites	4.0 – 5.0 ^c
$f(l)$	Segment length distribution	<ul style="list-style-type: none"> • 8-day-old : $\Gamma(\alpha = 1.32, \beta = 0.022)$ • 10-day-old : $\Gamma(\alpha = 1.71, \beta = 0.039)$ • 12-day-old : $\Gamma(\alpha = 1.52, \beta = 0.045)$

a identified by the observations using CLSM;

b fit to all the data from the 4th day to the 14th day (Fig. S3.6);

c from the 7th day.

a 2D lattice-based model for simulating the growth of *Postia placenta*. The tip extension rate and the branch angle distribution obtained in this work will be directly used as the input parameters for the model, while the segment length distribution calculated in the simulation will be compared with the experimental one to validate the rest branching parameters. Then the calibrated model will be extended to simulate the mycelial growth in heterogeneous environment with several hypotheses (e.g., the branch angle respects its intrinsic property but the extension and activity of this emerged branch is influenced by the environmental factor). However, the observation of hyphal growth in wood is important to further study, especially for validating a 3D model (work in progress in our team) to mimic hyphal growth in wood. Thus, the growth of *Postia placenta* in wood will also be

observed and quantified in using nano-tomography.

Acknowledgments

The authors are grateful to Mr. Cyril Breton (Laboratoire de Génie des Procédés et Matériaux, CentraleSupélec, Université Paris-Saclay, France) for his generous help with confocal laser scanning microscopy. Huan Du would like to acknowledge the financial support by the China Scholarship Council (CSC) for the study in France.

3.5 Supporting Information

Additional explanation for the measurement

- When measuring the segment lengths, the anastomosis point was also considered because it is difficult to distinguish the lateral branch (LB) site and the anastomosis point as depicted in Fig. S3.1. The proportion of the anastomosis points was very low, so that the increase of the short segments with time was still mainly caused by branching formation.
- When counting the number of LB sites, we checked the whole branch. Simple cases, such as branch 1 and branch 2, increase the number of sites by one. When two sites are found on one branch (e.g., branch 3), one is necessarily an anastomosis site, so one LB site was counted as well.
- When measuring the branching angles, we took the angle that was more close to 90° . However, the two angles (emanating from the LB and anastomosis sites) were both close to 90° , we took their average.

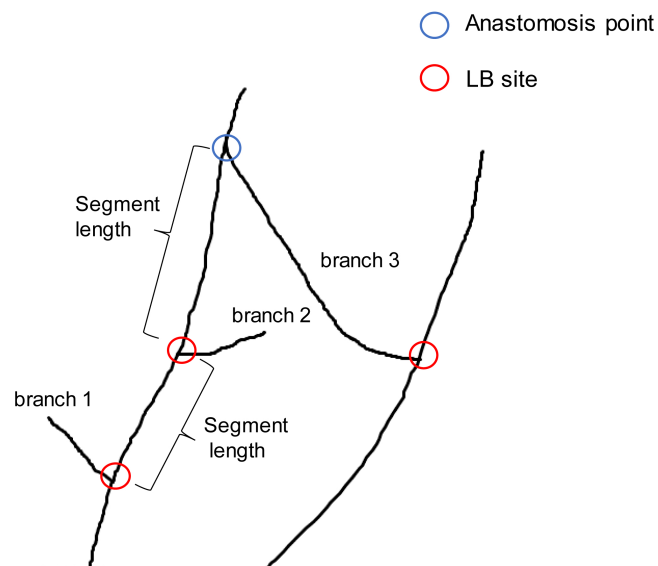


FIGURE S3.1 – Schematic showing the measurement of the segment lengths.

Supporting figures

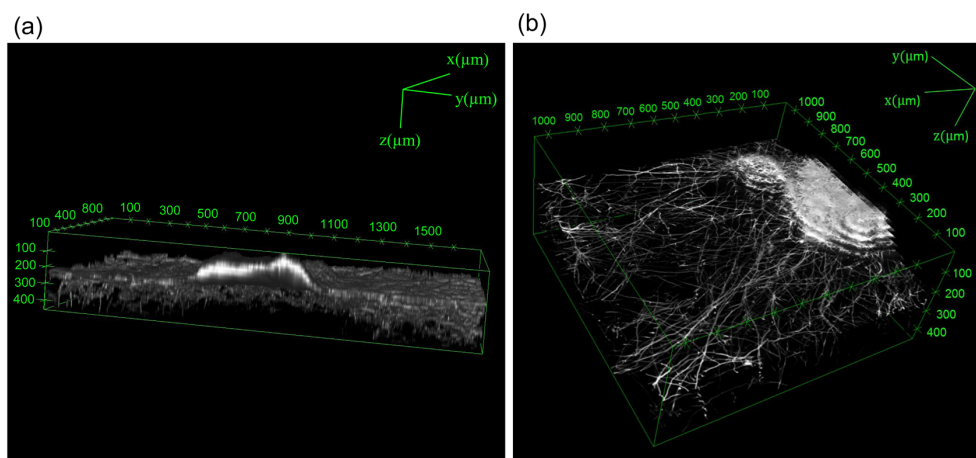


FIGURE S3.2 – 3D reconstruction of one section of the mycelium on the 12th day of observation.

(a) Cross-sectional view of the surface and penetrative hyphae. (b) Top view of the hyphae.

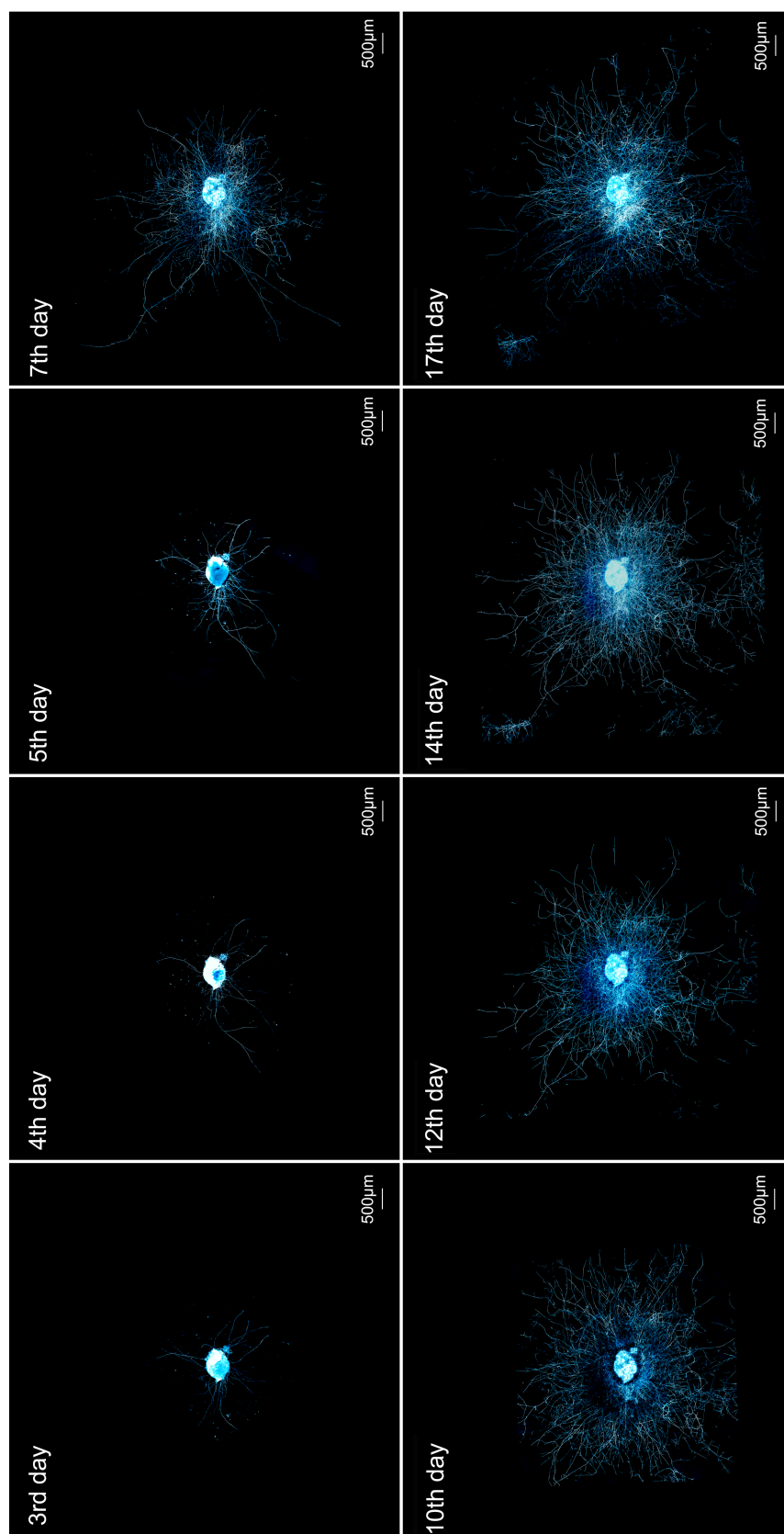


FIGURE S3.3 – 2D projection confocal images of *Postia placenta* obtained using the MIP method of the 3D images. The time evolution of the mycelial growth : the 3rd, 4th, 5th, 7th, 10th, 12th, 14th, 17th day following inoculation. The resolution is half of the original confocal images.

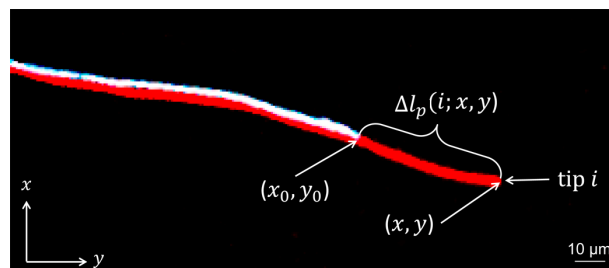


FIGURE S3.4 – Tip extension during two consecutive observations. The white curve is the hypha at the 1st observation and the red curve is its shape observed 2 days later. The coordinates of the tip positions are (x_0, y_0) and (x, y) respectively. $\Delta l_p(i; x, y)$ is the extension length of tip i (i.e., the length of the path from (x_0, y_0) to (x, y)).

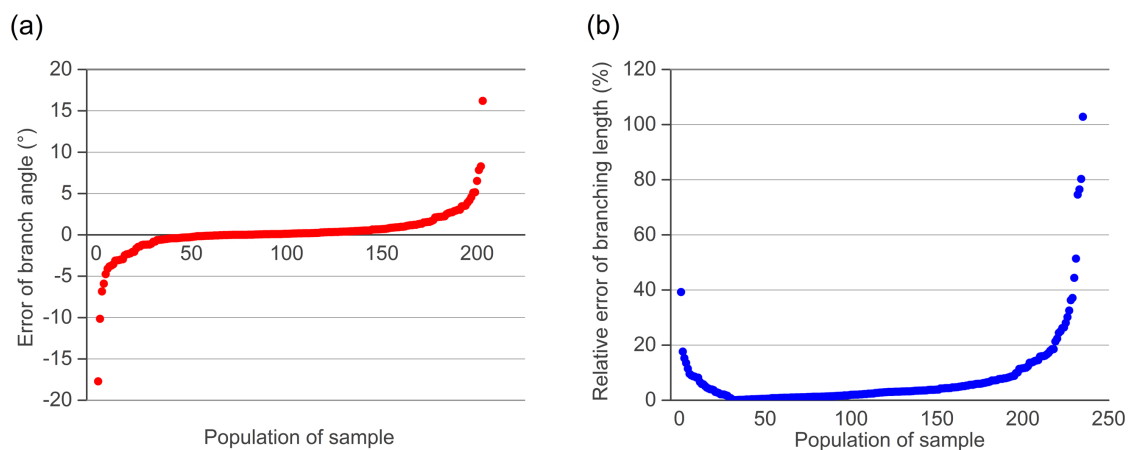


FIGURE S3.5 – Error of branch angle and segment length caused by z -direction growth of hyphae. (a) Error of branch angle, and (b) relative error of segment length calculated throughout all portions.

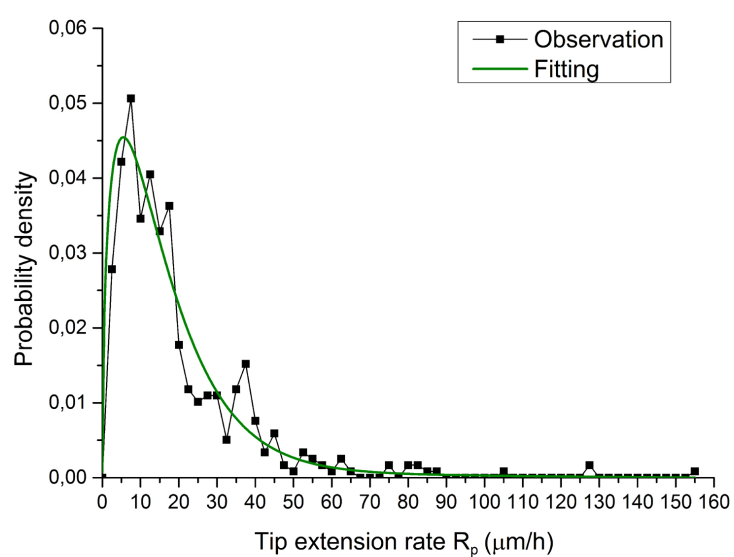


FIGURE S3.6 – Fitted curve of the tip extension rate distribution. The distribution, calculated by all the data from the 4th day to the 14th day, was well fitted by a gamma distribution corrected with a linear baseline.

Chapter4

Discrete model of mycelial growth in complex environment

*This chapter depicts a discrete lattice-based model to mimic the development of the mycelial network with time in various environment. In section 4.2, we present the main growth behaviors of hyphae, including tip extension, branching and anastomosis, and their response to the environmental stimuli. Section 4.3 depicts the transformation of these growth behaviors to mathematical rules which are incorporated into the lattice to realize a mathematical model. Then, in section 4.4, the validation of this model is implemented through experiment focusing on the morphology and the growth of *Postia placenta*. Two processes are included to determine the value of the modeling parameters : the value is directly obtained from the experiment and determined as in an inverse procedure by comparing the simulated results to the experimental ones. Finally, part 4.5 shows the mycelial growth in a complex environment, such as tropic media and porous media.*

•*This work is submitted.*

A lattice-based system for modeling mycelial growth in complex environment

Huan Du¹, Mehdi AYOUZ¹, Pin LV¹, Patrick Perré^{1*}

¹ LGPM, CentraleSupélec, Université Paris-Saclay, 92290, Châtenay-malabry, France

* patrick.perre@centralesupelec.fr

Abstract

Fungi are one of the most destructive agents to wood and wood-based products, resulting in the decrease of the building service life by breaking down lumber structures. This work presents a discrete lattice-based model to simulate mycelial growth, which explicitly incorporates tip extension, extension angle, anastomosis, and branching. The developed algorithm eliminates a geometrical restriction of the lattice directions; thus, it can generate realistic mycelial networks with low computational costs. Different growth conditions are reproduced via tropisms, which influence the tip dominant direction, such as thigmotropism that enables hyphae to bend around obstacles in structurally heterogeneous media. The validation of this model is implemented through an experiment focusing on the morphology and growth of *Postia placenta*, a species of brown rot fungi. Some model parameters are directly obtained from the experimental data, while others must be determined by an inverse procedure in comparing the simulated results with the experimental observation. This validated model provides an efficient tool for investigating and predicting mycelial growth under different conditions at the micro-scale.

4.1 Introduction

Due to highly-branched networks, mycelial fungi can survive in complex environments, such as soils, plant roots, and wood. Wood decay fungi play an essential role in the degradation of organic matter and cycling of the nutrient elements in the forest system. They are also the main organisms responsible for the decomposition of wood and wood-based products, which are traditional constructive materials in the building industry due to their

solidity, lightness, and sustainability. This is particularly problematic, as wood is promoted to address two main trends in building designs : the requirements for thermal performance and the use of renewable materials. However, an enormous amount of wood and wood-based products are destroyed by fungal decay every year, among which brown rot fungi are the most common and destructive within buildings throughout Europe and North America due to their rapid decay mechanisms [4]. Moreover, the breakdown of lumber structures leads to the reduction of building service life and even the risk of building collapse. Studying mycelial growth in different environments allows a better understanding of the fungal morphogenesis, predicting the service life of wood-based products and improving the protective methodology of wood.

As a supplemental tool to the costly and tedious experimental studies, mathematical modeling is efficient to mimic and forecast the behaviors of mycelial growth under different environmental conditions, which is especially crucial for service life to be accounted from the design stage. Efficient and validated models of fungal development are likely to be implemented in thermal models of the building envelope [113]. The approaches for simulating fungal growth are generally classified using continuous modeling and discrete modeling. In continuous models, the mycelium is treated as a continuous variable and is modeled by a system of partial differential equations [69, 86, 70, 88, 71, 114, 115]. This approach can describe the large-scale properties of mycelia in focusing on their collective attributes, such as the hyphal tip density, the biomass yield, and the substrate concentration. Thus, continuous models provide descriptions of mass distribution instead of the explicit morphological appearance. Contrary to continuous models, discrete models concentrate on the behavior of individual hyphae and describe the topological architectures of mycelium in its environment.

There are two popular approaches in discrete modeling of fungal growth, lattice-free models and lattice-based models. The lattice-free approach [80, 81, 82, 67, 77, 83, 84, 116, 68] represents the mycelial network as a collection of connected line segments. Without placing any restrictions on the position of these segments, the results produced by these models are extremely close to certain mycelial networks. However, due to the free network, these models usually induce a high computational complexity. Lattice-based modeling, as its name implies, is confined to a regular lattice. Different methods have been adopted to generate the filamentous mycelium on lattice, such as cellular automata (CA) [64, 117], network automata (NA) [78], and bond-based models [65, 79, 66]. The regular lattice, with a finite number of status transition rules and a finite number of orien-

tations for hyphal tip extension, allows the incorporation of complex growth behavior and realizes large improvements in computational efficiency. Since the hyphal growth is restricted to an artificial and predefined lattice, these models do not yield visually realistic networks as for lattice-free models.

This paper proposes a new lattice-based algorithm that can correctly simulate the mycelial shape, therefore accumulating the advantages of off-lattice and on-lattice models. This approach is also well suited to the process of model validation, as the initial conditions can be supplied as the binary mask of the inoculum. This feature allows straightforward use of our previous work [94], devoted to the observation and analysis of the morphology and the growth of *Postia placenta* using confocal laser scanning microscopy (CLSM).

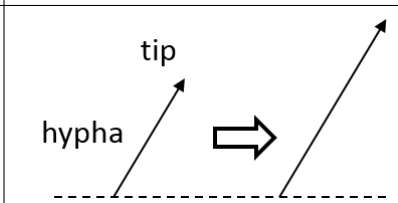
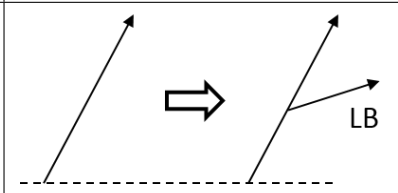
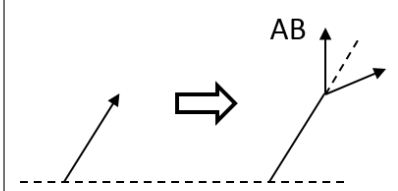
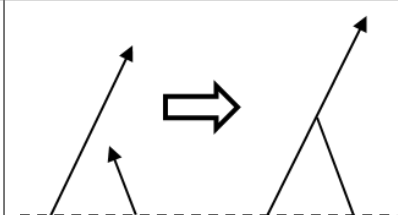
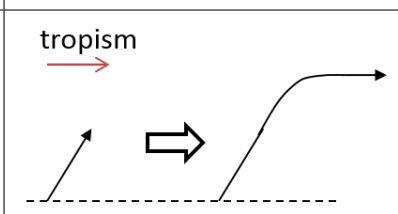
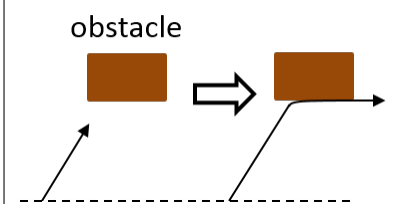
A set of rules are prescribed to simulate the mycelial growth, including tip elongation, anastomosis, and branching. In addition, the tropisms are incorporated in the model in consideration of the porous and fibrous structural tissue of wood. The same growth mechanisms are applied in such environments, provided the porous geometry and the other environmental stimuli are accounted for via tropisms to modify the hyphal elongation. Then, the validation of this model, which is carried out using the experimental data of our previous work on the growth of *P. placenta*, are depicted. Certain model parameter values are obtained directly from the experimental data, while the others are determined as an inverse procedure by comparing the simulated results to the experimental ones. Finally, several examples of mycelial networks in different conditions that can be generated by our model are provided. Overall, this model maintains the original advantage of the lattice-based approach in developing the mycelial networks more efficiently in different environments, and to our knowledge, this is the first model that overcomes the restriction of the lattice to the topology of mycelial networks due to the new mechanism of tip extension proposed in the model.

4.2 Fungal growth behaviors

Fungi are well adapted for growing in complex environments due to their ability to form hyphae, which consist of a complex network (i.e., mycelium). Hyphae are the characteristic growth form of fungal cells with a filamentous structure. The main growth behaviors of hyphae in forming mycelia include elongation, branching, and anastomosis and are

illustrated in Table 4.1 along with the response of hyphae to environmental stimuli (i.e., tropisms and obstacles).

TABLE 4.1 – Illustration of fungal growth behaviors.

Growth Behavior	Growth Pattern
Hyphal elongation	
Lateral branching (LB)	
Apical branching (AB)	
Anastomosis	
Tropism	
Obstacle	

With few exceptions, a hypha elongates strictly by apical deposition of wall skeletal po-

lysaccharides [26]. This apical part, contributing to hyphal elongation, is called the tip. A subcellular structure (i.e., Spitzenkörper) is found at the tips of the elongating hyphae, affecting the hyphal growth direction [118]. Without external stimuli, hyphal elongation maintains a relatively straight direction with frequent meandering. From time to time, hyphae abandon the original growth direction and establish a new one with minor directional change of approximately 10° due to the shift in Spitzenkörper trajectory.

In addition to elongation, hyphae can generate new hyphae by branching, which results in the formation of the networks of mycelia. Two types of branching, apical branching and lateral branching, are defined according to their branch sites and their growth patterns. Typically, apical branching is the emergence of two branches from a hyphal tip around which these two branches symmetrically develop [119], while the generation of new branches from the sub-apical part of one hypha is referred to as lateral branching. Lateral branching formation could be triggered by the stochastic accumulation of vesicles at a cortical site or behind hyphal cell septa [28]. Statistical analysis indicates that the selection of lateral branch sites is independent of the hyphal age or the branch density [94]. However, the formation of lateral branches is inhibited near a hyphal tip, which is known as apical dominance of individual hyphae [120].

Along their elongation, hyphae can contact each other and undergo fusions to yield an interconnected mycelial network. This phenomenon is anastomosis. Two morphological types of hyphal fusion are observed, tip-to-tip and tip-to-side. The process of anastomosis can be positive (e.g., two tips attract each other) and passive (hyphal fusion occurs when a tip contacts a hypha) [54]. For simplicity, only the passive anastomosis is considered in our model.

Although hyphae possess their intrinsic growth habit, their behaviors, especially hyphal growth direction, are greatly affected by environmental stimuli (e.g., chemicals [32], electrical fields [33] and physical contact [34]). Most of the external factors cause unidirectional tropisms, which make the hyphae grow along a determined direction (toward or away from the stimulus), except the thigmotropism, which forces the hyphae to ramp along the surface of an obstacle. The direction and intensity of a tropism are determined by the property or concentration of the stimuli. The reaction of fungi to the same environmental stimuli can be different depending on the species as well as the other factors existing in the environment (e.g., nutrients concentration and chemical elements) [121]. In addition to the tropisms, the external nutrient concentration can influence fungal morphology even

though their gradients do not create a tropism to hyphal growth direction. It is widely accepted that fungi growing in low-nutrient conditions adopt an 'exploratory' phase during which the formation of new branches is strongly inhibited [35].

4.3 Implementation of growth rules into lattice

The mycelium is modeled using a 2D square lattice with spacing δ . The position of each node in the lattice is represented by its coordinates (x_i, y_j) , and the number of hyphae $N_h(x_i, y_j, t)$ contained in node (x_i, y_j) at time t denotes the status of nodes with $N_h = 0$ for a vacant node and $N_h \in \mathbb{N}^+$ for an occupied node. The nodes of the lattice correspond to the possible locations of hyphal tips. For each tip i , three variables are defined to describe its status: $O_p(i, t)$, $\theta_p(i, t)$, and $R_p(i, t)$, which denote the location, the angle of the tip growth direction with respect to the positive x -axis, and the extension rate of tip i at time t , respectively. For each tip, the time-sequence of its previous positions builds a set of linked nodes, which constitute its trailing hypha. The three main behaviors of mycelial growth and the response of hyphal tips to environmental stimuli are implemented in the 2D square lattice (the effect of the corresponding parameters on fungal growth behaviors are depicted in Table 4.2).

4.3.1 Hyphal elongation

The hyphal elongation is modeled as a biased random walk following the tip extension direction identified by θ_p . To follow this direction, at each time step of duration τ , the tip attempts to move into one of the two neighboring nodes adjacent to this direction, $(x_i + \delta \text{sng}(\cos \theta_p), y_j)$ and $(x_i, y_j + \delta \text{sng}(\sin \theta_p))$ where $\text{sng}(x)$ represents the sign of x , according to the probabilities P_p^x and P_p^y with the relationship shown in Eq. 4.1 (Fig. 4.1(a)). Consequently, we set the probability of the movement into the other two nodes to be zero. During each time step, this tip may advance one step along the x -axis or y -axis and leave a trailing hypha formed by a sequence of linked nodes. These nodes are regularly distributed along the growth direction to form a visually smooth hypha which follows a relatively straight growth axis (Fig. 4.1(b)).

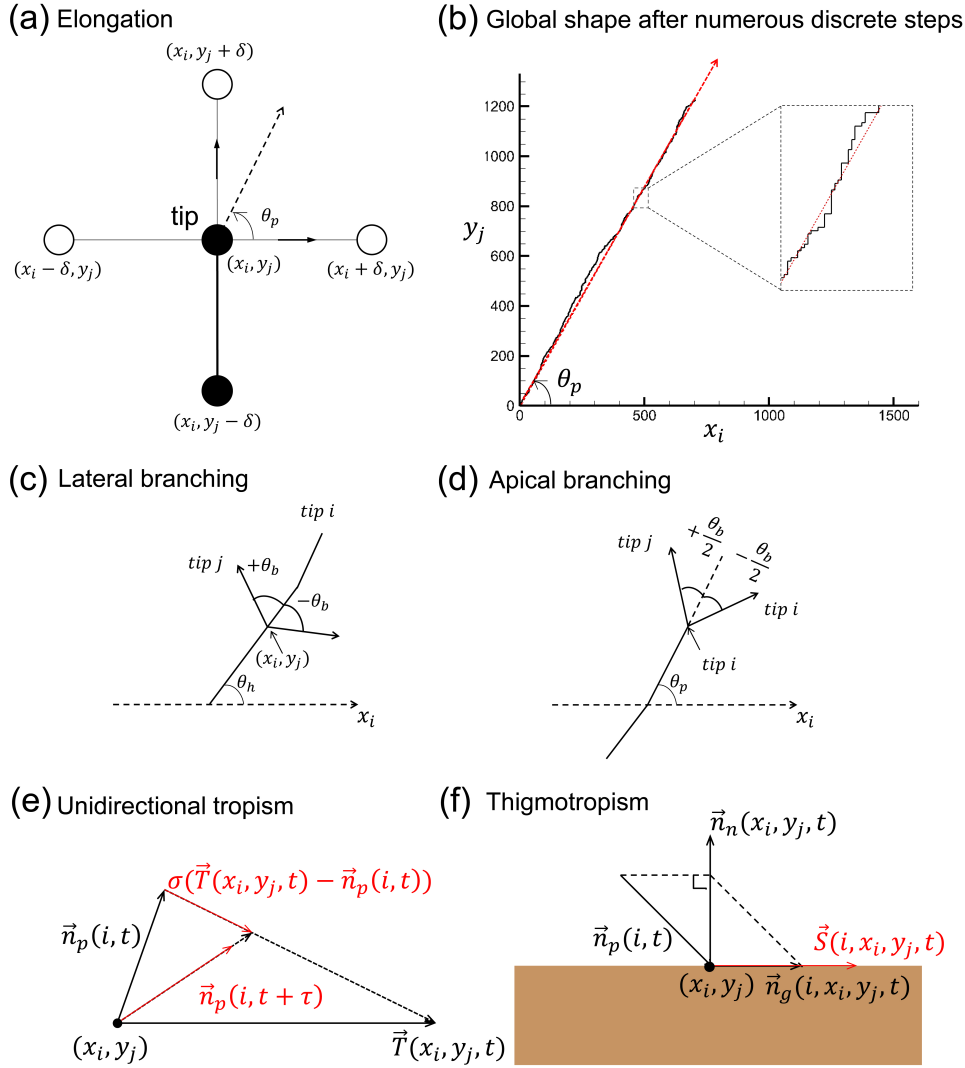


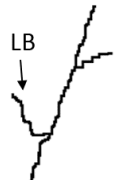





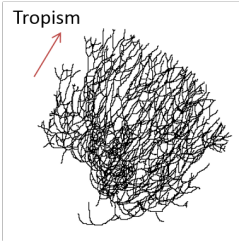
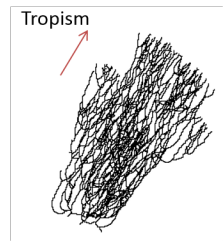

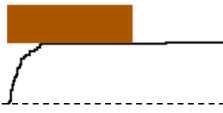


FIGURE 4.1 – Main mechanism of hyphal growth. Hyphal elongation in the lattice : (a) Elongation rules : consider the tip at location (x_i, y_j) and the four nodes adjacent to it; tip movement with P_p^x and P_p^y to select randomly one of the two nodes, $(x_i + \delta, y_j)$ and $(x_i, y_j + \delta)$, adjacent to the tip extension direction identified by θ_p as the target node during the next time step. (b) The global shape as an emergence of the local rules : after many iterations, the local stepwise effect disappears, and the tip extension rate and its direction become obvious. A hypha elongates following its extension direction with meandering. (c) Lateral branching : a lateral branch j emerges from the node located at (x_i, y_j) , with a branching angle θ_b with respect to the tangent direction (identified by $\theta_h(x_i, y_j)$) to the hypha at (x_i, y_j) ; (d) Apical branching : two apical branches emerge from tip i , symmetrically with respect to the tip direction θ_p with branching angle θ_b . The new tip is indexed as j , and the other keeps the tip number i . (e) Tropisms : the updated tip dominant direction for the next time step $\vec{n}_p(i, t + \tau)$ is obtained by applying the unidirectional tropism \vec{T} to $\vec{n}_p(i, t)$; ν is the reaction rate of hyphae. (f) Thigmotropism : calculation of the thigmotropism \vec{S} applied to the tip i located at (x_i, y_j) at time t ; \vec{n}_n is the unit normal vector of the solid surface, \vec{n}_p denotes the tip dominant direction, and \vec{n}_g is the vector projection of \vec{n}_p on the tangent of the solid surface.

TABLE 4.2 – Demonstration of the effect of the parameters on fungal growth behaviors.

Growth Behavior	Parameter	Effect (Growth Pattern During Δt)	
		①*	②*
Hyphal elongation	R_p		
Lateral branching	P_b^l		
Apical branching	P_b^a		
Anastomosis	P_a		
Tropism	$\ \vec{T}\ , \nu$		
Obstacle	c_s, ν		

* The value of parameter in the column ① is lower than that in the column ②.

$$\frac{P_p^x}{P_p^y} = \frac{\cos \theta_p}{\sin \theta_p} \quad (4.1)$$

Provided that the tip extension rate is constant, without the variation of tip extension direction ($\forall t \geq 0, \theta_p(i, t) = \theta_p(i, 0)$), the actual elongation length of the hypha over a period Δt is calculated as follows :

$$l_h(i, \Delta t) = \frac{\Delta t}{\tau} [P_p^x(i, 0) + P_p^y(i, 0)] \frac{\delta}{\cos \theta_p(i, 0) + \sin \theta_p(i, 0)}, \quad (4.2)$$

where $\frac{\Delta t}{\tau}$ denotes the number of time steps during Δt and $P_p^x(i, 0) + P_p^y(i, 0) \in [0, 1]$ represents the probability of the extension of tip i at each time step. Accordingly, their product is the number of steps that the tip i advances over time Δt . As the tip extension rate is constant, the total length of the hyphae growing over the same time must be equal regardless of along which direction they elongate, resulting in a linear relationship between $P_p^x + P_p^y$ and $\cos \theta_p + \sin \theta_p$ with a coefficient c_0 depending on the tip extension rate R_p . The formula of the tip extension rate is expressed as follows :

$$R_p(i, t) = \lim_{\Delta t \rightarrow 0} \frac{l_h(i, t) - l_h(i, t - \Delta t)}{\Delta t} = \frac{\delta}{\tau} \frac{P_p^x(i, t) + P_p^y(i, t)}{\cos \theta_p(i, t) + \sin \theta_p(i, t)} = c_0 \frac{\delta}{\tau}. \quad (4.3)$$

As the probability of extension is equal to or less than 1, the maximum duration of each time step τ_{max} is determined by the maximum rate of tip extension R_{pmax} and the maximum value of $\cos \theta_p + \sin \theta_p$:

$$\tau_{max} = \frac{\delta}{\sqrt{2} R_{pmax}}. \quad (4.4)$$

The probability of tip extension toward the two allowed nodes, one along the x -axis (P_p^x) and the other along the y -axis (P_p^y), are derived by Eq. 4.1 and Eq. 4.3 :

$$\begin{cases} P_p^x(i, t) = R_p(i, t) |\cos \theta_p(i, t)| \frac{\tau}{\delta}, \\ P_p^y(i, t) = R_p(i, t) |\sin \theta_p(i, t)| \frac{\tau}{\delta}. \end{cases} \quad (4.5)$$

Overall, one of the three events, i) remaining in the position, ii) advancing along the x -axis or iii) advancing along the y -axis, occurs to each tip at each time step with respective probabilities $1 - (P_p^x + P_p^y)$, P_p^x and P_p^y . The tip extension rate is regulated by adjusting the value of the two probabilities. If $R_p > 0$, the tip is active and if $R_p = 0$, the tip is dormant and does not elongate.

Note that hyphae change their growth axis from time to time. Thus, before elongation, the tip extension direction is updated with probability P_{dir} to decide whether a small directional change occurs or not. If it happens, the direction varies by either $+10^\circ$ or -10° with

equal probability with respect to its former direction. Then, the probabilities P_p^x and P_p^y are calculated with the updated extension direction.

4.3.2 Branching

To implement lateral branching rules into the lattice, the tangent direction to a hypha at a node (x_i, y_j) is determined by $\theta_h(x_i, y_j)$ and equals the tip extension direction when the tip was at this position (x_i, y_j) . As shown in Fig. 4.1(c), a lateral branch emerges from a node belonging to the sub-apical part of the hypha, located at (x_i, y_j) . The extension direction of the new tip j is identified by $\theta_h(x_i, y_j) + \theta_b$ or $\theta_h(x_i, y_j) - \theta_b$ from which one is randomly picked. Moreover, θ_b denotes the branching angle that can be either constant or determined as a distribution. For the apical branching (Fig. 4.1(d)), two branches emerge from tip i , and one is randomly labeled as a new tip j so that the other one remains tip i . The dominant directions of the two tips, which are symmetrical with respect to the previous tip direction, are set to $\theta_p(i, t) + \theta_b/2$ and $\theta_p(i, t) - \theta_b/2$.

The frequency of lateral branching obeys the probability P_b^l for a branch to form from a hypha during a time step. The number of lateral branches to be formed at time t is calculated as follows :

$$\Delta N_b^l(t) = N_b^l(t) - N_b^l(t - \tau) = \lfloor P_b^l N_p(t) \rfloor + 1_{A1}(\omega), \quad (4.6)$$

where $N_p(t)$ is the total number of tips at time t ; “ $\lfloor \cdot \rfloor$ ” is a floor function mapping the real number to the largest previous integer; 1_{A1} is an indicator function that has the value 1 if $\omega \in A1$; ω is a number randomly picked in the interval $[0, 1]$; $A1 = \{x | x \in (0, P_b^l N_p(t) - \lfloor P_b^l N_p(t) \rfloor)\}$. Due to the stochastic pattern of lateral branching formation mentioned in section 2, we apply an equal probability of branching to all mycelium. Thus, the ΔN_b^l positions of branch formation are randomly selected from the set involving all the nodes occupied by hyphae except those that have emerged branches or are inhibited by apical dominance. One node is considered inhibited by apical dominance when the distance of this node to the tip is less than l_{ad} , which is defined as the length of apical dominance.

Since the apical branching occurs at the active tips, we apply the same probability P_b^a to each active tip. The number of apical branching during the time increment is obtained as

follows :

$$\Delta N_b^a(t) = N_b^a(t) - N_b^a(t - \tau) = \left[P_b^a N_{ap}(t) \right] + 1_{A2}(\omega), \quad (4.7)$$

where $N_{ap}(t)$ is the total number of active tips ($R > 0$) at time t ; 1_{A2} an indicator function, which has the value 1 if $\omega \in A2$, where ω is a random number in the interval $[0, 1]$ and $A2 = \{x | x \in (0, P_b^a N_{ap}(t) - \lfloor P_b^a N_{ap}(t) \rfloor)\}$. Then, $\Delta N_b^a(t)$ tips are randomly selected from all active tips.

4.3.3 Anastomosis

The anastomosis is simply incorporated in the model by assuming that it occurs when a hyphal tip contacts another hypha. In the 2D lattice, all hyphae are in the same plane so that two intersecting hyphae eventually touch each other. However, in the real colony, hyphae grow in a 3D space, and they possess a probability of horizontal separation. Therefore, we define a probability of anastomosis P_a to determine whether a tip that moves into an occupied node anastomoses or not. If it anastomoses, the tip is removed from the lattice, otherwise the tip crosses over the hypha and continues to elongate. The anastomosis influences the number of tips in the lattice, and thereby the production of mycelial biomass.

4.3.4 Tropism and obstacle

Two types of external stimuli are incorporated in this model, unidirectional tropism and obstacles. The unidirectional tropism is represented by a vector field $\vec{T}(x_i, y_j, t)$ of which the direction depends on the location of the stimuli. The magnitude of $\vec{T}(x_i, y_j, t)$ represents the intensity of the tropism. In addition to the tropism intensity, the reaction rate of hyphae to the tropism influences the changing rate of the tip extension direction. Thus, a coefficient of hyphal reaction rate ν is defined. The tip extension direction is denoted by a unit vector $\vec{n}_p(i, t) = (\cos \theta_p(i, t), \sin \theta_p(i, t))$. The tip extension direction \vec{n}_p is changed by the tropism \vec{T} at each time step as shown in Fig. 4.1(e), and the affected \vec{n}_p is calculated as follows :

$$\vec{n}_p(i, t + \tau) = \frac{\vec{n}_p(i, t) + \Delta\vec{n}_p(i, t)}{\|\vec{n}_p(i, t) + \Delta\vec{n}_p(i, t)\|}, \quad (4.8)$$

$$\Delta\vec{n}_p(i, t) = \nu[\vec{T}(i, x_i, y_j, t) - \vec{n}_p(i, t)].$$

The obstacles located in the lattice generate a thigmotropism around them. The thigmotropism vector $\vec{S}(i, x_i, y_j, t)$ is related to both the presence of obstacles and the direction of the tips. As shown in Fig. 4.1(f), the direction of the thigmotropism is within the tangent plane to the surface. Its magnitude, which gives the intensity of this tropism, depends on the extension direction of the tip i arriving at (x_i, y_j) (i.e., $\vec{n}_p(i, t)$) and the intensity coefficient $c_s(x_i, y_j)$ with $c_s > 0$ for the nodes surrounding the obstacle and $c_s = 0$ for the others. The thigmotropism vector is calculated as follows :

$$\vec{S}(i, x_i, y_j, t) = c_s(x_i, y_j) \frac{\vec{n}_g(i, x_i, y_j, t)}{\|\vec{n}_g(i, x_i, y_j, t)\|^2}, \quad (4.9)$$

$$\vec{n}_g(i, x_i, y_j, t) = \vec{n}_p(i, t) - [\vec{n}_p(i, t) \cdot \vec{n}_n(x_i, y_j)]\vec{n}_n(x_i, y_j),$$

where $\vec{n}_n(x_i, y_j)$ is the unit vector normal to the surface and $\vec{n}_g(i, x_i, y_j, t)$ is the projection of the tip direction vector on the tangent plane. Due to the divisor $\|\vec{n}_g\|^2$ in Eq. 4.9, the intensity of the thigmotropism decreases as the tip direction approaches the tangent plane of the surface. The thigmotropism generated by the obstacles influences the tip extension rate in the same way as the unidirectional tropism. As Eq. 4.8 is linear, this equation can be simply applied with the total tropism \vec{T}_{tot} obtained by the sum of tropisms (i.e., $\vec{T}_{tot} = \vec{T} + \vec{S}$).

4.3.5 Simulation

Following the procedures described above, the growth of a mycelium can finally be simulated. A simulation basically comprises two important steps :

- **Step 1. Initial field** : The initial mycelium (spores or a binary mask of plugs of mycelium) is replicated in the lattice (position and directions) as well as the environmental conditions (tropisms and obstacles) by setting the initial variables to each node.
- **Step 2. Incremental growth** : The evolution of the mycelium is obtained by iterative time increments. During each time step, all the tips are randomly selected since there is no priority for hyphal growth. Then, the mycelium is expanded by applying two main processes to hyphae : tip extension and branching. The anastomosis and

the effect of the tropisms are incorporated into the process of tip extension. Thus, the tip extension process is responsible for the determination of the tip dominant direction and hyphal elongation, while the branching process leads to new tips.

4.4 Calibration from growth observation

The developed model was calibrated using the parameter values and statistical data obtained from our recent work on the mycelial growth experiment of *Postia placenta* (strain FPRL 280) [94]. In this experiment, a tiny plug of *Postia placenta* was inoculated on a media of malt extract agar. Then, the mycelial growth in homogeneous conditions was visualized using CLSM and analyzed during a 17-day period. Part of the modeling parameters was directly obtained from the experimental data; the rest was determined as an inverse procedure by comparing the simulated results and the experimental data.

4.4.1 Initial field

In the experiment, a sequence of images of mycelial growth were obtained using CLSM microscopy from the third day after inoculation. The first confocal image (Fig. 4.2 (a)) was transformed into a binary mask and embedded in the center of the lattice at $t = 0$ as the initial field of the simulation. As shown in Fig. 4.2 (b), we divided the colony into three parts : inactive inner-inoculum (in black), tips (in red), and outstretched hyphae (in blue). The inoculum was active and could continuously emerge new hyphae. However, in the model, due to the anastomosis mechanism, the hyphae in the inner inoculum had difficulties to extend. Thus, we assumed that the nodes inside the inoculum were inactive and could neither elongate nor emerge branches, whereas all the nodes on the edge of this inoculum were considered tips. These tips were inactive at $t = 0$, and 10% of the inactive tips were transformed as dormant tips every 24 hours. This is a way to mimic the delayed behavior of the emergence of tips from the inner part of the inoculum. We defined that inactive tips can never elongate before transformation, while dormant tips will elongate when they achieve an extension rate higher than $0 \mu\text{m}/\text{min}$. All these tips have an extension direction that is outwards from the inoculum. Moreover, the tips of the outstretched hyphae were also recorded and their extension direction was calculated by a normalized vector directed from the tenth node backward from one tip (the first node of this hypha if it contains less than 10 nodes) to this tip. Note that the outstretched hyphae were active

to emerge branches. The tangent direction to these hyphae at each node was necessary to determine the direction of the newly emerged branches. This tangent direction was estimated in the same way using the coordinates of this node and the tenth node backward.

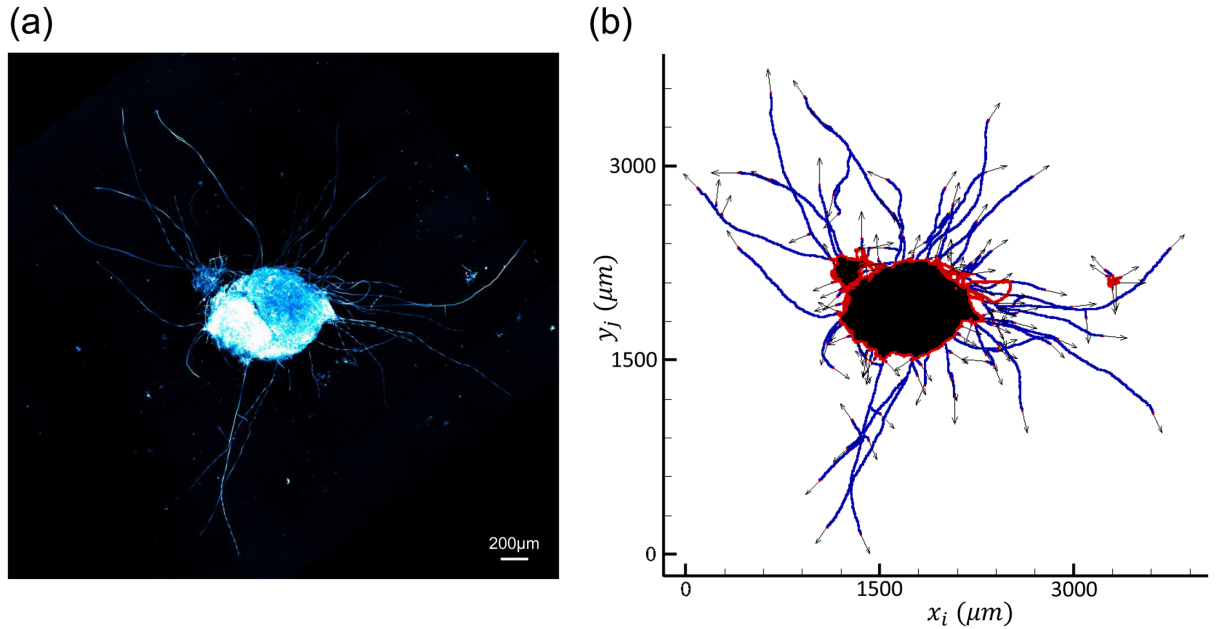


FIGURE 4.2 – (a) Image of mycelium of the first observation using CLSM was transformed on (b) a binary mask, which was used as an initial field in the simulation. The black, red, and blue nodes represent the inactive inner inoculum, the tips, and the outstretched hyphae, respectively. The tip extension directions of the outstretched hyphae were shown by the unit vectors in black.

4.4.2 Parameter defined directly from experimental observation

All the parameters mentioned in this section were directly obtained from the experiment as detailed in [94]. For the model, the spacing of the lattice $\delta = 3 \mu\text{m}$ was determined by the average diameter of hyphae of *Postia placenta*. The lattice is 4000 by 4000 nodes large, which corresponds to an area of 1.44 cm^2 . As 99.0% of the tip extension rates in the experiments were less than $80 \mu\text{m}/\text{h}$, we set $R_{pmax} = 80 \mu\text{m}/\text{h}$. Thus, the maximum value of the time scale $\tau_{max} = 1.59 \text{ min}$ was obtained by Eq. 4.4 with $R_{pmax} = 80 \mu\text{m}/\text{h}$. For simplicity, time step τ was set as 1.5 min . The active tips were selected from all active and dormant tips every 24 hours by a probability of activation obtained from the experiment as $P_{active} = 0.7$. The extension rate of each active tip was determined by a corrected gamma cumulative distribution F_{Γ} , which was fitted to the experimental data :

$$F_{\Gamma}(R_p; \alpha, \beta) = \Gamma(\alpha = 1.51, \beta = 0.09) + 4.65 \times 10^{-6} (R_{pmax} R_p - \frac{1}{2} R_p^2). \quad (4.10)$$

The value of the probability P_{dir} was set as 0.05 to realize a minor directional change in tip extension from time to time.

According to the experimental results, the difference of hyphal growth in the lag and exponential phase was significant mainly in the branching frequency. Consequently, we define a ratio k_{lag} of the branching frequency in the lag phase to that in the exponential phase. Its value was estimated as 0.2 based on the observed results, which acted on the value of P_b^l and P_b^a in the two growth phases. In the simulation, the lag phase lasted two days, followed by the exponential phase. The branching angle θ_b is represented by a Gaussian inverse cumulative distribution with $\mu = 77.6^\circ$ and $\sigma = 12.3^\circ$, which allows the experimental data to be nicely fitted. Finally, the length of apical dominance was defined as the minimum length measured between the tip and the proximate branch ($l_{ad} = 5 \mu m$).

4.4.3 Parameters determined by inverse analysis

The experimental values of branching probabilities (lateral branching P_b^l and apical branching P_b^a) and anastomosis probability (P_a) are not explicitly available. Indeed, their effect on the network structure can be assessed only after many time increments. Therefore, they must be determined by an inverse procedure. Optimistically, the three parameters are not independent. The observed ratio $N_b^l/N_b^a \in [4.0, 5.0]$ reveals that P_b^l is proportional to P_b^a . From Eqs. 4.6 and 4.7, where N_p and N_{ap} respectively denote the total number of active and dormant tips and that of active tips, the ratio P_b^l/P_b^a was calculated and should be in the range $[2.8, 3.5]$ since $P_{active} = 0.7$. We set P_b^l/P_b^a to 3.5. Thus, P_b^a is linearly related to P_b^l . Only two independent parameters remain. The discussion below will focus on the relationship between P_b^l and P_a by fixing $P_b^l/P_b^a = 3.5$.

To determine their values, we compared the simulated and experimental segment length distributions. The segment length is defined as the distance between two successive sites of either branches or anastomosis, as the two types of sites are difficult to be distinguished in observation. In the experiment, three regions were partitioned in the observed images (from the center outward : R1, R2, and R3), to select different durations of mycelial growth, from old to young (details in [94]). In this published work, we defined the age of the region to compare the growth observed in different regions and on different days,

post inoculation. Each two consecutive regions are two days apart in age, and R1 is the oldest region. The segment length distributions of each region were calculated with the data measured in four radially arranged portions. The same measurements were carried out for the three corresponding regions partitioned in the lattice. The results show that the peak of the distribution is shifted toward short segment lengths in the simulated results, from interval $[0 \mu m, 10 \mu m]$ to $[10 \mu m, 20 \mu m]$ (Fig. 4.3 (a)). This indicates that, branching is inhibited near an already existing branch. This inhibition exists to avoid the generation of too many short segments and was implemented as a local lateral branching mechanism (LOC) (Fig. 4.3 (b)), which eliminates the possibility of lateral branching over N_{LOC} nodes on both sides of any branch/anastomosis site. The optimal value of N_{LOC} was determined through a criterion C_1 , using the root mean square (RMS) of the difference between the simulated results and the fitted curves :

$$C_1 = \frac{1}{3} \sum_{X \in \{R1, R2, R3\}} \sqrt{\frac{1}{n} \sum_{i=1}^n (g_\gamma^X(l_b^i) - f^X(l_b^i))^2}, \quad (4.11)$$

where l_b^i is the length of the i^{th} interval, n is the total number of intervals, and g_γ^X and f^X respectively denote the fitted gamma distribution and the probability density calculated with the simulated data in Region X . We used several sets of parameters (P_a, P_b^l) and computed criterion C_1 with different values of N_{LOC} . C_1 was found to have its minimum value for $N_{LOC} = 5$, which corresponds to a distance of $15 \mu m$. It is important to note that, with this value, the RMS is also small for each individual region (R1, R2, and R3).

Criterion C_1 was relevant while focusing on small segments but underestimated the contribution of large segments to the biomass production. Therefore, we defined a second criterion C_2 in which the segment length distribution is weighted by the length of each category :

$$C_2 = \frac{1}{3} \sum_{X \in \{R1, R2, R3\}} \sqrt{\frac{\sum_{i=1}^n (g_\gamma^X(l_b^i) l_b^i - f^X(l_b^i) l_b^i)^2}{\sum_{i=1}^n g_\gamma^X(l_b^i) l_b^i}}, \quad (4.12)$$

where C_2 was calculated with the simulated distributions f in R1, R2, and R3 at the end of the 12th day and the corresponding experimental data. For each value of P_a , simulations were performed with several values of P_b^l , keeping P_b^l/P_b^a equal to 3.5, as stated before. Fig. 4.4 shows the contour plot of $C_2(P_a, P_b^l)$, which depicts a valley-like shape with a small influence of P_a ; whatever the value of P_a , the minimum of C_2 is obtained for al-

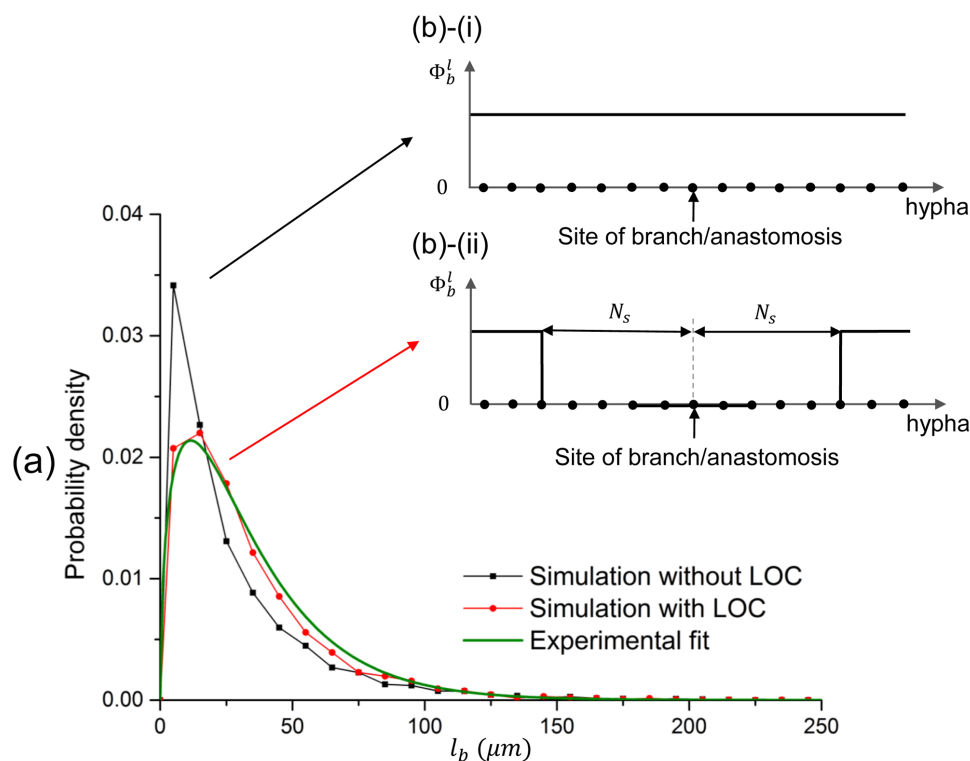


FIGURE 4.3 – (a) Segment length distributions obtained from the experimental fit (in green), the simulation without LOC (in red), and the simulation with LOC (in black), (simulation parameter values : $P_a = 0.1$, $P_b^l = 0.001$, $P_b^a = 0.00029$); (b)-(i) possibility of lateral branching (Φ_b^l) along a hypha without LOC, (b)-(ii) in applying LOC, no branches emerge from the N_{LOC} nodes around a branch/anastomosis site.

most the same value of P_b^l (0.001). Indeed, an increase in P_a leads to a reduction of the total number of tips N_p , and hence a reduction of the number of branching formation per time-step. This effect tends to produce longer segments but is balanced by another effect, as the increase of anastomosis sites divides more segments into shorter ones. Thus, C_2 is a good criterion to determine the value of P_b^l but is quite loose regarding the value of P_a . Through the analysis above, we noticed that increasing P_a simultaneously reduces the total hyphal elongation and the branching emergence, which has a great negative effect on the fungal biomass. Hence, P_a should be defined by accounting for the total biomass production. To do so, the objective function should consider the total biomass production rather than the dimensionless distribution.

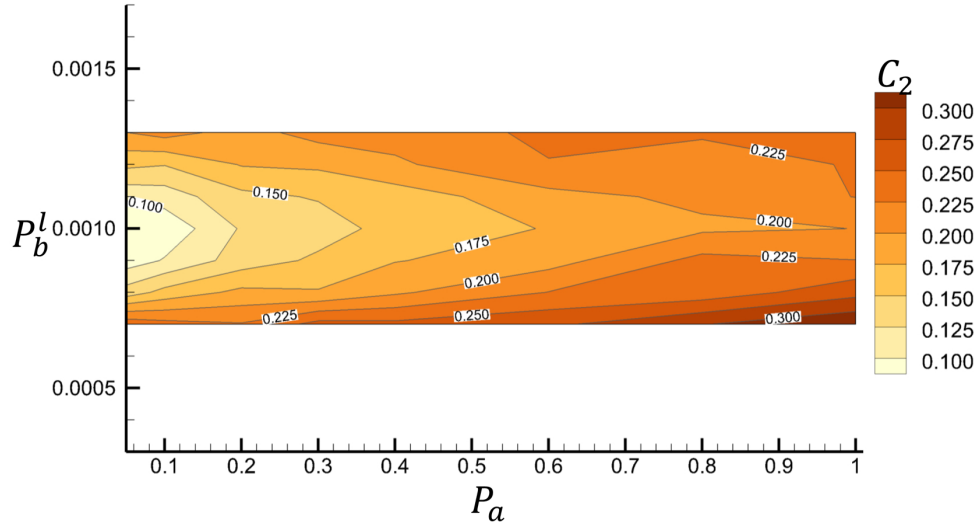


FIGURE 4.4 – The 2D contour (C_2) displays the effect of (P_a, P_b^l) on the segment length distribution (12th day).

4.4.4 Validation on macroscopic profiles

To determine the optimal P_a , we compared the computed normalized biomass density profiles with the experiment at different observation days in fixing $(P_b^l = 0.001, P_b^a = P_b^l/3.5)$. The normalized radial biomass density $\rho(r, t)$ was calculated by averaging the discrete network along the radius :

$$\rho(r, t) = \frac{1}{N_n(r)} \sum_{\{(x_i, y_j) | r - \frac{\Delta r}{2} \leq \sqrt{x_i^2 + y_j^2} < r + \frac{\Delta r}{2}\}} (N_{occupy}(x_i, y_j, t)), \quad (4.13)$$

where N_{occupy} is equal to 1 if the node (x_i, y_j) is occupied and 0 if not. Additionally, N_n denotes the total number of nodes within the corresponding ring. We chose $60 \mu m$ for Δr as a good compromise to reduce the noise level of the profiles without losing information on the profile shape. Fig. 4.5 (a) and (b) show the biomass density profiles, respectively, at 5 and 12 days, post inoculation. The biomass density augments with the decrease of P_a , especially when the value of P_a is low. The simulated profile obtained with $P_a = 0.1$ agrees the most with the experimental profile. This result coincides with the segment length distribution, which indicates that the macroscopic result and the statistical data are consistent.

After the determination of the optimal set of $(P_a = 0.1, P_b^l = 0.001, P_b^a = 0.00029)$, all modeling parameters were obtained and are listed in Table 4.3. With these parameter values, we find that the simulated result is consistent with the experimental data on

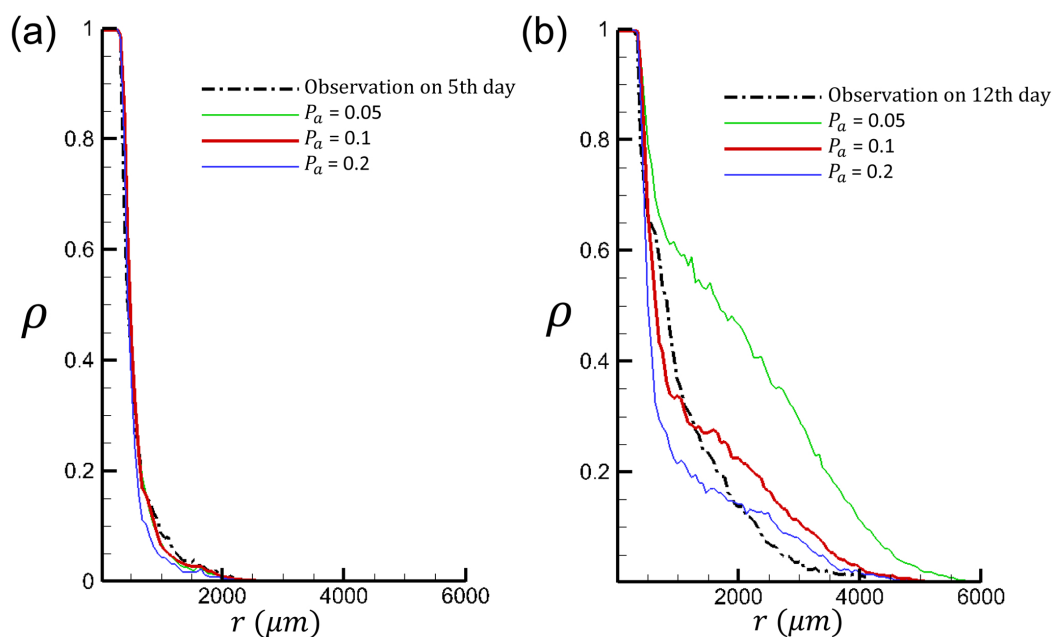


FIGURE 4.5 – Normalized biomass density profiles (ρ) on the 5th and 12th day.

the evolution of the segment length distribution versus time (Fig. 4.6). The distributions were calculated with the simulated network in each region and time corresponding to the age/region relationship defined in the experimental work [94]. A good agreement was found between simulated and experimental results. This means that the model can account for the intricate effects of distance and time on the development of the mycelial network, namely the spatial invasion due to tip elongation and apical branching and the densification of the network due to lateral branching. However, the relatively rapid increase of branching/anastomosis sites in R1 and the slow increase in R3 reveals that the probability of anastomosis may change with the density of hyphae since the thickness of the colony can augment, resulting in the increase of the growth space of hyphae.

Fig. 4.7 depicts the evolution of the mycelial network with time obtained both in the simulation and the experiment. These graphs confirm that the simulated spatial development of the mycelial network is a good representation of the actual morphology development, as observed by CLSM.

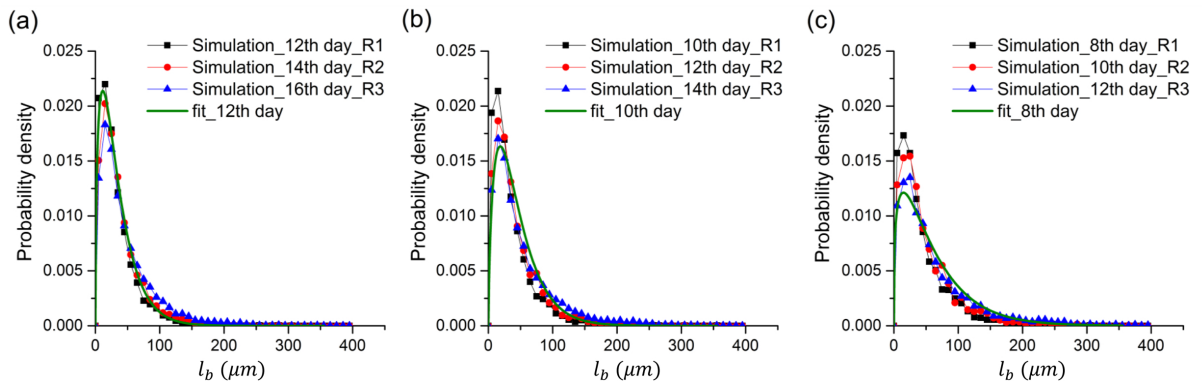


FIGURE 4.6 – The fitted curve of observations at different ages of region and the distributions of the branching lengths : (a) 12-day-old (simulated data from R1 on the 12th day, R2 on the 14th day and R3 on the 16th day); (b) 10-day-old (simulated data from R1 on the 10th day, R2 on the 12th day and R3 on the 14th day); (c) 8-day-old (simulated data from R1 on the 8th day, R2 on the 10th day and R3 on the 12th day). Parameter value in the simulation : $P_a = 0.1$, $P_b^l = 0.001$, and $P_b^a = 0.00029$.

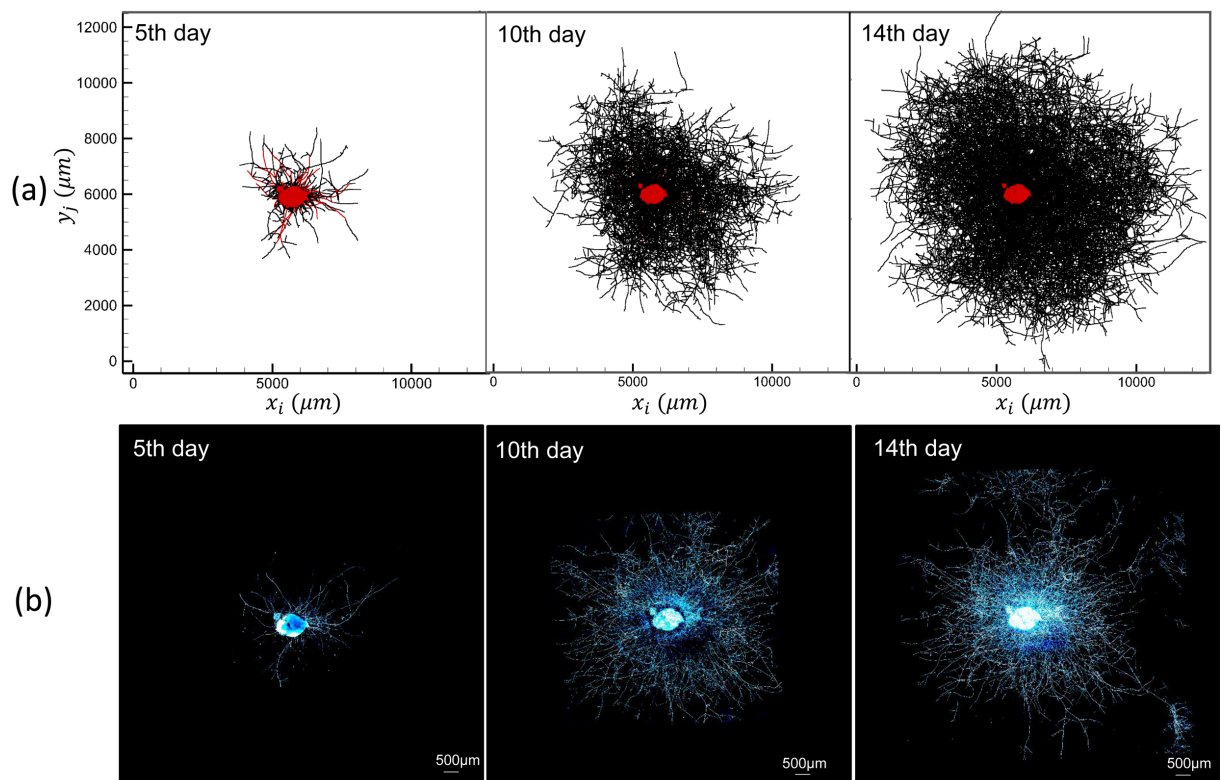


FIGURE 4.7 – Evolution of the topological architecture of a mycelial network versus time obtained by (a) simulation with $P_a = 0.1$, $P_b^l = 0.001$, $P_b^a = 0.00029$, and (b) observation using CLSM on the 5th, 10th and 14th days.

TABLE 4.3 – Description and values of the modeling parameters.

Parameter	Description	Value & Expression
R_p	Tip extension rate	$\Gamma(\alpha = 1.51, \beta = 0.09) + 4.65 \times 10^{-6}(R_{pmax} - R_p)$
θ_b	Branching angle	$\mathcal{N}(\mu = 77.6^\circ, \sigma = 12.3^\circ)$
l_{ad}	Length of apical dominance	$5 \mu m$
P_b^l	Probability of lateral branching	0.001
P_b^a	Probability of apical branching	0.00029
P_a	Probability of anastomosis	0.1
N_{LOC}	Number of nodes around a branch that do not emerge branches	5

4.5 Potential in complex environment

To depict the potential of the model, various simulations of mycelial growth in different environments were carried out with the calibrated parameters listed in Table 4.3. The dimension of the lattice was set as $18000 \mu m \times 18000 \mu m$ and the mycelial network spread from a spore placed at the center of the lattice (i.e., $(9000 \mu m, 9000 \mu m)$).

4.5.1 Obstacles in mycelial growth environment

To mimic fungal development in porous media, such as fiberboards, solid obstacles with a periodic pattern were included into the lattice. In Fig 4.8A, the two series of graphs, (i) and (ii), show the mycelial networks at two times, which are $t = 15000 \text{ min}$ and $t = 30000 \text{ min}$, in the case of free growth (a) and for two different porous media :

- Squares with side length of $1500 \mu m$ and distance between two neighboring squares of $1500 \mu m$ (b);
- Rectangles with dimension of $4500 \mu m \times 1500 \mu m$ and distance between two neighboring rectangles of $1500 \mu m$ (c).

We arbitrarily fixed the extension direction of the tip extended from the spore as 45° with respect to the positive x -axis. The tips developed around the obstacles due to the thigmotropism and changed the mycelial morphology and biomass distribution. From (a) to

(c) in Fig. 4.8A, it is obvious that obstacles reduced the entire expansion of the mycelium. The rate of tip extension slows down because of the reduced space available for fungal development (porosity) and increased local length (tortuosity) generated by the obstacles. In the case of square obstacles, the expansion is reduced by the same amount in the x - and y -directions. In the case of the rectangles, the reduction is much larger along the y -direction since the obstacle width limits the possibility of vertical expansion (Fig. 4.8A(c)(i)). Fig. 4.8B depicts the averaged density profiles along x and y for the three configurations at two contrasting times. In each case, the average is computed along a line perpendicular to the profile direction, including the porous and solid phases (for the concept of global averaging, see [122]). At $t = 15000 \text{ min}$ (dashed lines), the density profiles confirm that the extension is smaller in porous media than in a homogeneous environment. These profiles confirm the anisotropic behavior of the rectangular shape; the profiles along y are narrower than profiles along x . These trends are even more pronounced at $t = 30000 \text{ min}$ (solid lines). Overall, these simulations allow the analysis of biomass distribution in structurally heterogeneous environments, such as fiber panels used for building insulation. The model is therefore ready to be applied to mycelial growth in realistic porous media by placing obstacles with irregular shapes.

4.5.2 Other complex environments

In addition to the obstacles, the different distributions of nutrients and existence of tropisms can cause different strategies of mycelial growth. Some examples are shown in Fig. 4.9. The two series of graphs, (i) and (ii), show the mycelial networks at two times, which are $t = 11250 \text{ min}$ and $t = 22500 \text{ min}$ in one realization, respectively, while the effect of three environmental factors are presented in (a)-(c). As shown in Fig. 4.9 (a), a complex structure was generated by canceling branching and increasing the tip extension rate in a shell area due to a lack of nutrients, for example. In Fig. 4.9(b) and 4.9(c), a uniform unidirectional tropism of 60° with respect to the positive x -axis but with two different intensities ($\|\vec{T}\| = 1.0$ and $\|\vec{T}\| = 0.5$) was applied to the environment. The tips tended to follow this direction, and all hyphae formed a smoothly curved structure. With the same reaction rate, the morphology of the curved structure depends heavily on the intensity of the tropism.

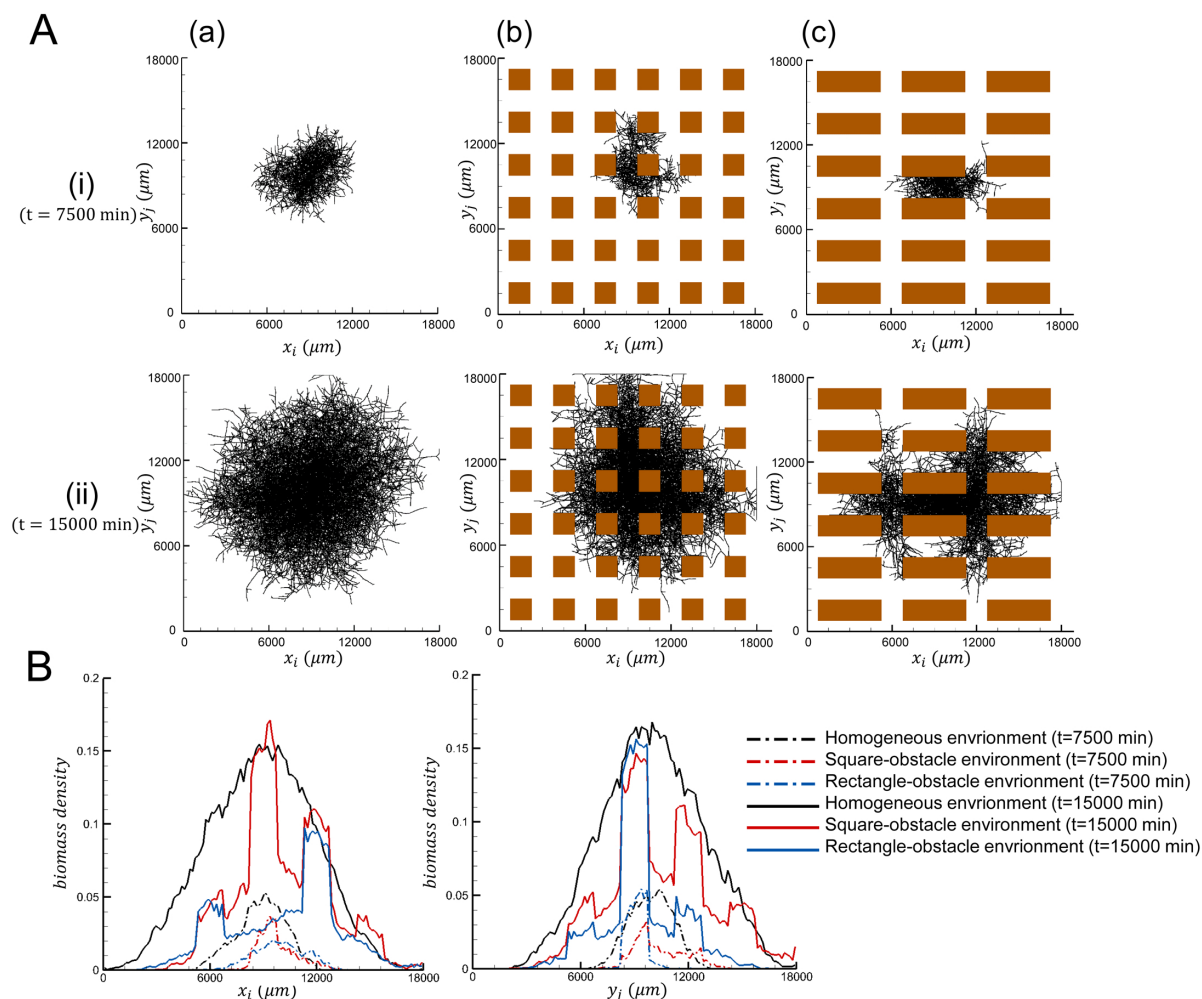


FIGURE 4.8 – Mycelial growth in structurally heterogeneous environments. A : Mycelial networks in (a) a homogeneous environment, (b) an environment with squares of $1500\ \mu\text{m}$ sides, and (c) an environment with rectangles of dimensions of $4500\ \mu\text{m} \times 1500\ \mu\text{m}$. The parameter values are $c_s = 1.0$, $v = 0.01$, $P_b^l = 0.001$, $P_b^a = 0.00029$, and $P_a = 0.1$. The model networks are shown at two times : (i) $t=15000$ min and (ii) $t=30000$ min. B : Column density of biomass along x - and y -directions for the six mycelial networks in A.

4.6 Conclusion

A discrete lattice-based model able to mimic mycelial development has been derived, incorporating the basic growth behaviors of hyphae, including tip extension, branching, and anastomosis. An important feature of this model is the elimination of the restriction of the lattice configuration to the hyphal elongation and branching angle. As a result, this model

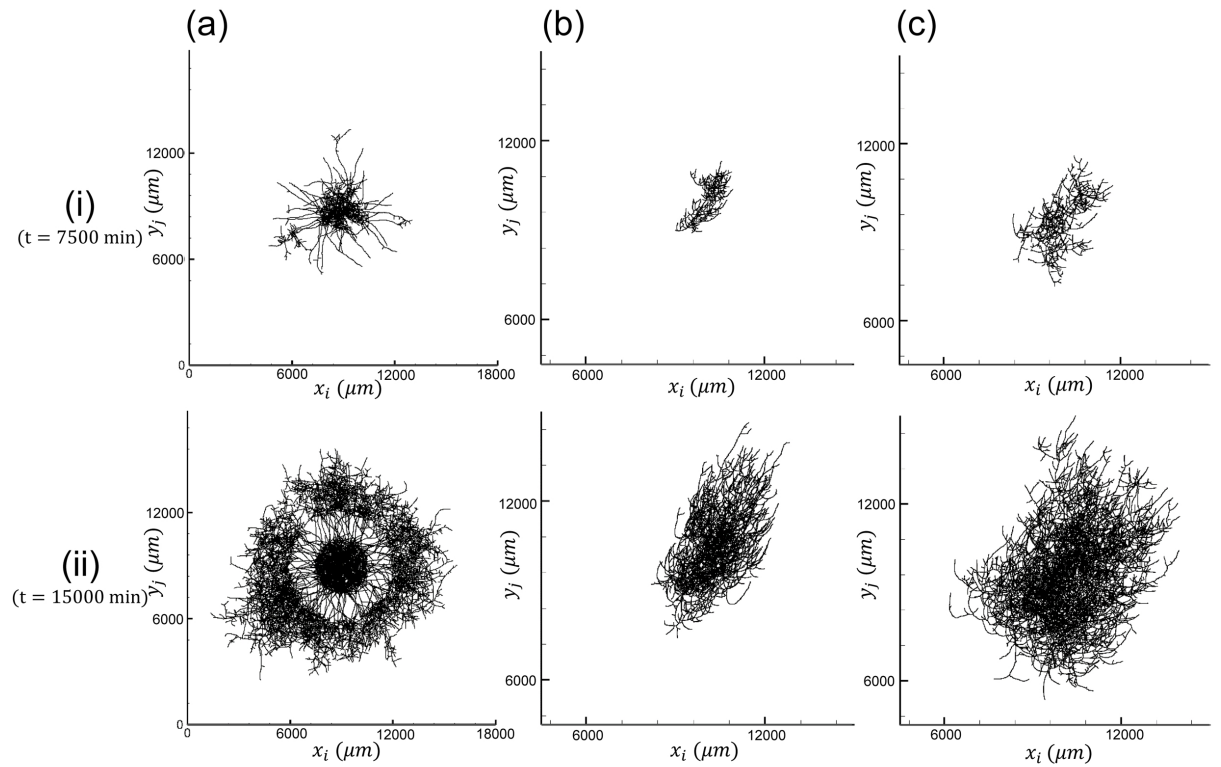


FIGURE 4.9 – Different growth strategies of mycelium in response to various environmental factors : (a) inhibition of branching in a shell area with the inner radius $1500 \mu\text{m}$ and the outer radius $3000 \mu\text{m}$; application of a tropism directing to 60° with respect to positive x -axis with tropism intensity (b) $\|\vec{T}\| = 1.0$ and (c) $\|\vec{T}\| = 0.5$ in fixing the reaction rate $\text{upsilon} = 0.01$. The parameter values are $P_b^l = 0.001$, $P_b^a = 0.00029$ and $P_a = 0.1$. The model networks are shown at two times : (i) $t = 11250 \text{ min}$ and (ii) $t = 22500 \text{ min}$.

generates a visually realistic mycelial network. Moreover, due to the tropism and obstacle mechanisms, the model possesses the potential to reproduce the different possible strategies of mycelial growth in complex environments. In particular, the thigmotropism permits hyphal growth in a structurally heterogeneous media, which provides a base for simulating hyphal growth in bio-based products. A rigorous procedure has been carried out to feed the model with all needed parameters from experimental observation, including the parameters obtained directly from experimental results and those determined by inverse analysis. Branching and anastomosis probabilities were determined through their effect on the mycelium network after a huge number of time steps. With these calibrated parameters, the model is able to reproduce the intricate coupling between spatial invasion and network densification. This validated discrete model will be used to tune a continuous model able to realize fungal development over larger scales in complex morphologies.

4.7 Supporting Information

Validation of the elongation mechanism

The hyphal elongation is modeled as a biased random walk following the tip extension direction. With the probability of tip extension P_p^x and P_p^y , the tip selects at random a node adjacent to the direction and advances into it. In averaging 10 identical simulations of the elongation process along one direction, we tested if the averaged hypha follows exactly this direction. Fig. S4.1 shows seven tests along seven different directions. The averaged hyphae are well coincident to their predetermined directions. In addition, Fig. S4.1 reveals that the elongated lengths of hyphae over the same time are equal despite of their growth directions when their extension rates are the same.

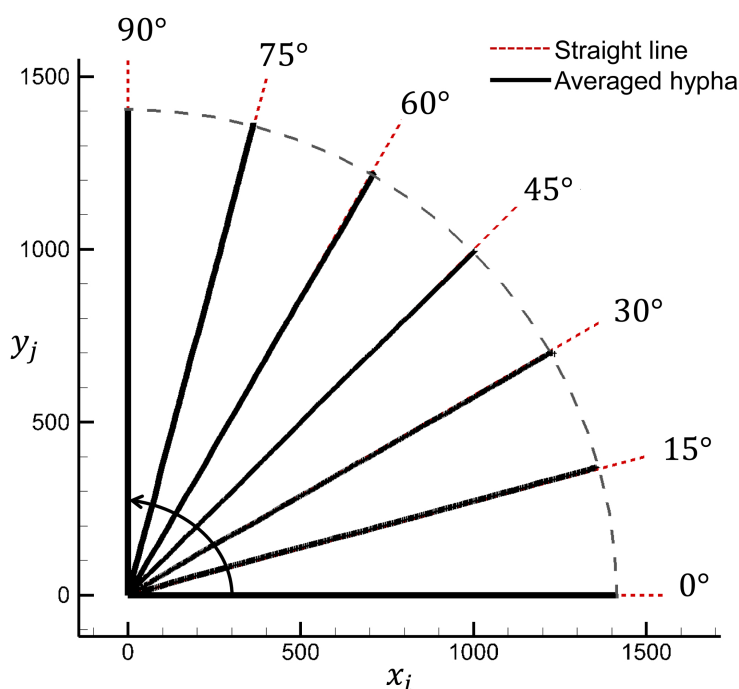


FIGURE S4.1 – Test of the elongation mechanism. Seven averaged hyphae (black solid lines) over 10 identical simulations agree perfectly with their predetermined extension directions (red dashed lines) in a dimensionless lattice. The hyphae elongate over $t = 2000$ with the same extension rate.

Impact of lateral branching mechanisms on mycelial morphology

We have tested two mechanisms for the selection of the sites of lateral branches :

- **Dirac function**

Only the nodes having a fixed length behind the tips possess a probability of lateral branching greater than 0 and the others cannot emerge lateral branches.

- **Equal probability**

All the nodes occupied by hyphae except those that have emerged branches or inhibited by apical dominance possess an equal probability of lateral branching.

The mycelia formed in following the two lateral branching mechanisms are shown respectively in Fig. S4.2(a)(b). The morphologies of the two mycelia are totally different. The Dirac function leads to a relatively uniform biomass distribution in the whole colony, while the biomass density is evidently much higher in the center of the colony and became lower and lower from the center outwards due to the equal probability. Obviously, for *Postia placenta*, the second lateral branching mechanism is more suitable.

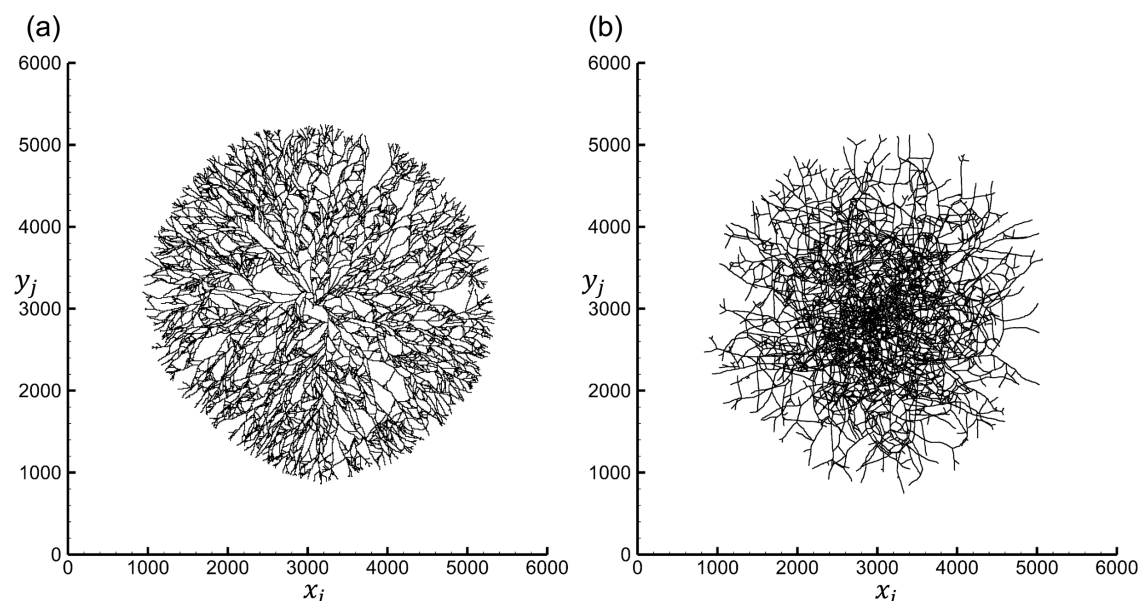


FIGURE S4.2 – Mycelial networks generated by two different lateral branching mechanisms. (a) Dirac function and (b) equal probability.

TABLE 4.4 – Mathematical functions for modeling hyphal growth behaviors.

Growth behavior	Function	Notation	
Hyphal elongation	$\begin{cases} P_p^x(i, t) = R_p(i, t) \cos \theta_p(i, t) \frac{\tau}{\delta} \\ P_p^y(i, t) = R_p(i, t) \sin \theta_p(i, t) \frac{\tau}{\delta} \end{cases}$	P_p^x	Probability of tip extension along x -axis
		P_p^y	Probability of tip extension along y -axis
		R_p^*	Tip extension rate
		θ_p	Angle of tip extension direction with respect to positive x -axis
		τ	Duration of each time step
		δ	Lattice spacing
		i	Tip number
		t	Time
Lateral branching	$\begin{aligned} \Delta N_b^l(t) \\ = N_b^l(t) - N_b^l(t - \tau) \\ = \lfloor P_b^l N_p(t) \rfloor + 1_{A1}(\omega) \end{aligned}$	N_b^l	Total number of lateral branches
		P_b^{l*}	Probability of lateral branching
		N_p	Total number of tips
		$1_{A1}(\omega)$	Indicator function which has the value 1 if $\omega \in A1$
		$A1$	Set involving the real number between 0 and decimal part of $P_b^l N_p(t)$
		ω	Random number in $[0, 1]$
Apical branching	$\begin{aligned} \Delta N_b^a(t) \\ = N_b^a(t) - N_b^a(t - \tau) \\ = \lfloor P_b^a N_{ap}(t) \rfloor + 1_{A2}(\omega) \end{aligned}$	N_b^a	Total number of apical branches
		P_b^{a*}	Probability of apical branching
		N_{ap}	Total number of active tips
		$A2$	Set involving the real number between 0 and decimal part of $P_b^a N_{ap}(t)$
Anastomosis	$\Delta N_p(t) = \sum_{i=1}^{N_p(t)} -1_{[0, P_a]}(\omega) 1_{\mathbb{N}^+}(N_h(O_p(i, t), t))$	P_a^*	Probability of anastomosis
		O_p	Coordinates of tip location
		N_h	Number of hyphae contained in a node
Tropism	$\begin{cases} \vec{n}_p(i, t + \tau) = \frac{\vec{n}_p(i, t) + \Delta \vec{n}_p(i, t)}{\ \vec{n}_p(i, t) + \Delta \vec{n}_p(i, t)\ } \\ \Delta \vec{n}_p(i, t) = \nu [\vec{T}(i, x_i, y_j, t) - \vec{n}_p(i, t)] \end{cases}$	\vec{n}_p	Unit vector denoting tip extension direction
		\vec{T}^*	Vector denoting unidirectional tropism
		ν^*	Coefficient of hyphal reaction rate to tropism
Obstacle	$\begin{cases} \vec{S}(i, x_i, y_j, t) = c_s(x_i, y_j) \frac{\vec{n}_g(i, x_i, y_j, t)}{\ \vec{n}_g(i, x_i, y_j, t)\ ^2} \\ \vec{n}_g(i, x_i, y_j, t) = \\ \vec{n}_p(i, t) - [\vec{n}_p(i, t) \cdot \vec{n}_n(x_i, y_j)] \vec{n}_n(x_i, y_j) \end{cases}$	\vec{S}	Vector denoting thigmotropism generated by obstacles
		c_s^*	Intensity coefficient of thigmotropism
		\vec{n}_g	Projection of the tip direction vector on the tangent plane
		\vec{n}_n	Unit vector normal to the surface of obstacles

* The parameter can be regulated to affect fungal growth behaviors.

Chapter5

Continuous model of the fungal growth in porous media

This chapter presents a continuous formulation capable of simulating the fungal growth in porous media at the macro-scale. The strategy of this work follows two major steps. As depicted in part 5.2, the first step is to identify an equivalent reaction-diffusion equation from the radial biomass density of a mycelial network obtained from the validated discrete model. This equation simulates the expansion of fungal biomass at the colony scale (i.e., free growth at the local scale). Highly nonlinear expressions were obtained for the diffusivity and the source term, which is consistent with the local mechanisms of fungal development. This continuous model was then used to derive an equivalent macro-scale model able to account for fungal development in a structurally heterogeneous medium (part 5.3). Simulations were performed on various periodic heterogeneous media. In part 5.4, the parameters of a reaction-diffusion model were identified on the macroscopic field obtained by averaging the local field over one periodic unit cell. The identified functions for the equivalent diffusivity and source term have a form similar to the local model, but their values depend on the medium porosity and the morphology of the solid phase, possibly leading to an anisotropic equivalent medium.

Continuous model of the fungal growth in porous media : identification of a macroscale model from local-scale simulations

Huan Du¹, Patrick Perré^{1*}

¹ LGPM, CentraleSupélec, Université Paris-Saclay, 92290, Châtenay-malabry, France

* patrick.perre@centralesupelec.fr

5.1 Introduction

Wood and wood-based products have been popular constructive materials due to their excellent mechanical properties for many years. The good thermal performance and design of new manufacturing technology enable the reduction of energy consumption and emission, which responds well to the trends in building construction. This is why, these materials became even more promoted in construction. However, fungal decay in bio-based materials is of major concern in relation to the service time of buildings and even to human safety, since it weakens the structural support of wood enough to cause mechanical failure. Every year an enormous amount of wood and wood-based products is destroyed by fungal decay, among which brown rot fungi are the most common and destructive within buildings throughout Europe and North America due to their rapid decay mechanisms [4]. Many researches have studied the growth and decay patterns of brown rot fungi as well as the impact of environmental factors to their growth [104, 42, 105, 106, 14, 15, 16]. Nevertheless, the laboratory observations are constrained by the scales of study and their cost. As a supplementary tool, mathematical modeling in combination with laboratory experiments can realize a deeper and wider insight in a more efficient way.

It is a challenge to model the spatial growth of filamentous fungi in porous media such as wooden panels or soils, which can be considered as multi-scale materials (e.g., pore scale and macro-scale). The modeling techniques to simulate the spatial distribution of fungi are classified into two categories : discrete models and continuous models. The previous ones adapt well to model the mycelial growth at a small scale in identifying individual hypha to form mycelial networks in porous media. For example, Boswell *et al.* (2007) and Boswell (2008) respectively developed a 2D and a 3D lattice-based mo-

del to simulate mycelial growth in a soil-like environment [65, 79]. Fuhr *et al.* (2011) constructed a 3D lattice-free model of hyphal growth in the heartwood of Norway spruce in simplifying the structure of wood. Alternatively, the density of fungal matter was viewed as smooth variable(s) in the continuous models, which are suitable for both colony and macroscale modeling. These models focused on the interaction of fungal growth with the environment, especially the distribution of nutrients. The early models were extended from reaction-advection systems which included nutrients and geometries of mycelial spread [69, 85, 123, 86]. However, the advection process requires the development direction to be known at each point, which limits the prediction ability of the code and/or augments the mathematical complexity especially in heterogeneous media. Thus, in the recent models, the diffusion process has replaced advection to model the movement of hyphae [70, 124, 87, 114, 125, 75]. Nevertheless, few of them investigated the fungal growth in a structurally heterogeneous environment and involved a multi-scale modeling. Apart from the models of spatial fungal growth, several macroscale models were developed to simulate non-spatial fungal growth in wood (i.e., the wood decay). These models focused on the impact of the environmental factors on the decay risk and the decay rate (i.e., the fungal expansion rate and the reduction rate of the woody biomass) based on the field test data or the laboratory test data [76, 92, 93].

This work is devoted to two-scale modeling of spatial fungal growth of a brown rot fungus, *Postia placenta*, in periodic porous media. Two successive upscaling techniques were performed to achieve this goal : i) a continuous formulation able to mimic the biomass development as simulated by a discrete model in free growth conditions and ii) the use of this continuous formulation to simulate the fungal development in a periodic heterogeneous model to derive an equivalent macroscale model.

The continuous formulation was first developed to simulate the distribution of fungal biomass of *Postia placenta* in applying a reaction diffusion (RD) equation. The parameters of the local-scale continuous model (the diffusion coefficient D and the source term S) were identified by an inverse method : the model parameters were adjusted to minimize the gap between the numerical solutions of the RD equation and the radial profiles of fungal biomass density calculated by the validated discrete model (in Chapter 4). Highly nonlinear expressions were obtained for the diffusivity and the source term, which is consistent with the local mechanisms of fungal development.

This continuous model was then used to derive an equivalent macroscale model able to

account for fungal development in a heterogeneous medium. Simulations were performed on various periodic heterogeneous media. The parameters of the RD model were then identified on the macroscopic fields obtained by averaging the local field over one periodic unit cell. Thus, the parameters of the macroscale model were identified from the local-scale growth of hyphae and can simulate the spatial fungal growth in porous media at both local- and macro-scales. Fig. 5.1 summarizes the procedure to develop the continuous formulation at the macroscopic scale.

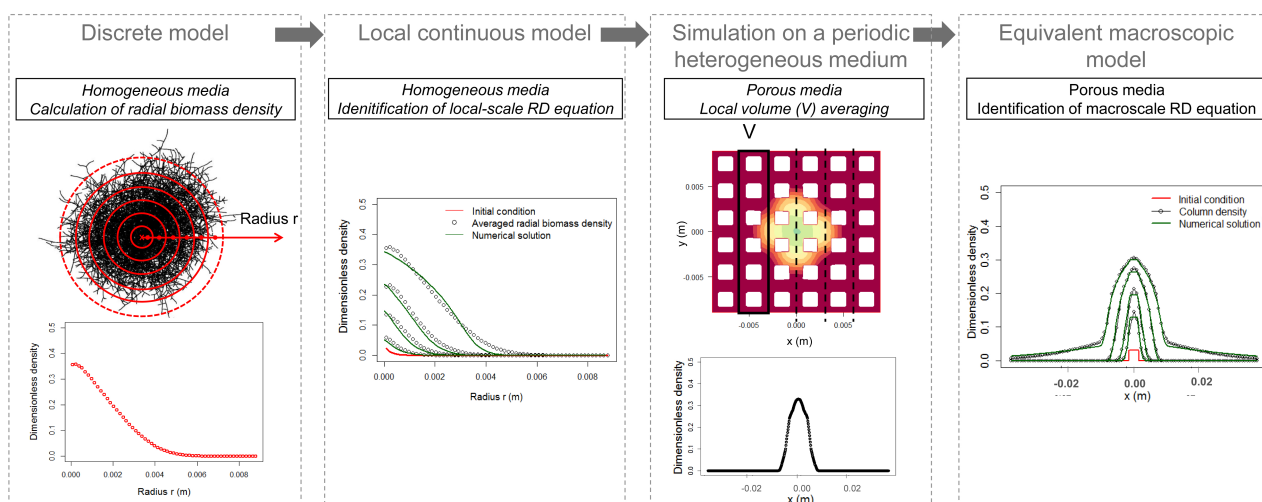


FIGURE 5.1 – Procedure of development of the continuous model.

5.2 Identification of the continuous model based on the discrete model

5.2.1 Radial biomass density calculated from the discrete model

In using the validated fungal growth parameters listed in Table 3.2, the discrete model presented in Chapter 4 generates a mycelial network from a spore. The simulated mycelium was divided into a series of rings with a gap of $\Delta r = 1.5 \times 10^{-4} \text{ m}$ (Fig. 5.2), of which the normalized radial biomass density $\rho(r, t)$ was calculated by averaging the discrete network over radius increments using Eq. 4.13. Note that ρ is a dimensionless variable which is the ratio of the space occupied by hyphae to the total space. Due to the numerous random processes in the discrete model, one simulation was not representative so that 100

realizations were simulated to obtain an averaged radial biomass density $\langle \rho \rangle (r, t)$ for each ring :

$$\langle \rho \rangle (r, t) = \sum_{k=1}^{100} \rho_k(r, t) / 100, \quad (5.1)$$

where ρ_k is the normalized radial biomass density in the k^{th} simulation. In addition, in following the evolution of fungal biomass distribution with time, the averaged biomass density was calculated at five times $t_1 = 4.5 \times 10^4$, $t_2 = 4.5 \times 10^5$, $t_3 = 6.75 \times 10^5$, $t_4 = 9 \times 10^5$ and $t_5 = 1.35 \times 10^6$ s. Thus, five profiles of the averaged radial biomass density at different times were obtained from the discrete model.

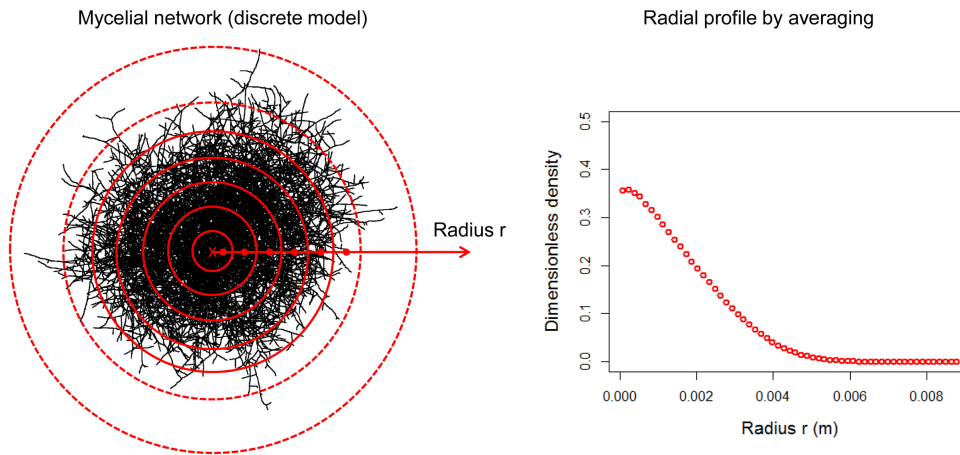


FIGURE 5.2 – Calculation of the normalized radial biomass density from the discrete model. (a) Series of ring-parts with equal gap divided on the mycelial network; (b) profile of normalized biomass density calculated in the rings.

5.2.2 Continuous model at the local scale

The normalized biomass density was treated as the variable to be reproduced by the continuous model to represent the fungal development. In the continuous model, the biomass density was denoted by B , a spatial field which evolves in time. A RD equation was solved in a 1D axisymmetric configuration to simulate the evolution of the biomass density in a homogeneous medium. The comparison of its numerical solution to the radial profiles of biomass density obtained with the discrete model was used as the objective function

to identify the diffusion coefficient $D(B)$ and the source term $S(B)$. The 1D RD axisymmetric formulation was used to calculate the radial biomass B , which can be compared to $\langle \rho \rangle$, and reads as follows :

$$\frac{\partial B(r, t)}{\partial t} = \frac{1}{r} \frac{\partial}{\partial r} \left(D(B) r \frac{\partial B(r, t)}{\partial r} \right) + S(B), \quad (5.2)$$

where r is the radius of the fungal colony and t denotes the time. After numerous tests, we found that both the diffusion coefficient and the source term must depend strongly on the biomass density. Finally, we optimize the parameters of the following nonlinear expressions, product of a constant term, an increasing function and a decreasing function :

$$D(B) = D_l B^\gamma (1 - B)^{\gamma'}, \quad (5.3a)$$

$$S(B) = \lambda B^\kappa (1 - B)^{\kappa'}. \quad (5.3b)$$

These expressions contain six degrees of freedom, D_l , γ , γ' , λ , κ and κ' , which build up the set of model parameters to be defined by inverse analysis. The flux of biomass on the boundaries was assumed to be zero and the initial condition was the profile of the averaged radial biomass density of the discrete model at $t = 4.5 \times 10^4$ s.

The RD equation was solved using the finite volume method in cylindrical coordinates. A uniform grid spacing (δ) was used to discretize the calculation domain and it was set to be equal to the spatial resolution of the profiles obtained in the discrete model (i.e., $\delta = \Delta r = 1.5 \times 10^{-4}$ m). A simple explicit scheme but with the time step τ that must then be made small enough to deal with non-linearity was applied for the numerical solution as a 1D solution is very fast. For a diffusion equation, the time step τ should be less than $\delta^2 / (2 \cdot D)$, which is the well-known stability criterion for the explicit scheme. However, as the diffusion coefficient D as well as the source term S are nonlinear functions of the biomass density, we made different tests to be sure that the time step is small enough to capture the strong nonlinear behavior. All simulations were performed with $\tau \leq 100$ s, which is much less than the simple stability criterion by 2 orders of magnitude.

5.2.3 Determination of D and S

The determination of D and S involves an optimization problem to make the numerical solution of the 1D RD equation close to the normalized biomass density obtained from the discrete model. The Nelder-Mead method was applied to minimize the mean squared error (MSE) between them, which was defined as follows :

$$MSE = \frac{1}{4N} \sum_{t \in \{t_2, \dots, t_5\}} \sum_{k=1}^N (\langle \rho \rangle [r(k), t] - B[r(k), t])^2, \quad (5.4)$$

where N denotes the total number of rings (here $N = 59$) and $r(k)$ represents the radius of the k^{th} ring.

Fig. 5.3(a) depicts the optimization results in which the value of MSE equals 6×10^{-4} . The red line represents the initial condition and the four curves plotted by circles represent the profiles of the averaged biomass density at the four additional selected times. The dark green lines are the numerical solutions of the RD equation. The profiles simulated by the continuous model are in quite close agreement with the corresponding profiles of the discrete model. In particular, one can note that the shape of the discrete model is globally well-captured by the nonlinear RD model, even though it resembles more a front-like progression than a diffusion phenomenon. This agreement is particularly good for the profiles at the first three times after the initial profile. The profile obtained for the last time is in slightly poorer agreement due to the peak value of the source term around $B = 0.15$ (Fig. 5.3(b)-(ii)). The value of the six parameters (i.e., D_l , γ , γ' , λ , κ and κ') governing the diffusion coefficient D and the source term S are listed in Fig. 5.3(a). The large value of γ' leads to the sharp decrease of D from the peak value towards 0 over a short interval of B , while the low value of γ forces the peak position to be close to $B = 0$ and D_l regulates the range of D (Fig. 5.3(b)-(i)). This means that, in the RD model, diffusion acts only over a short range of B values, which is a way for the continuous formulation to mimic the tip extension. After this first appearance of biomass, further increase in B is solely tied to the source term. The parameters λ , κ and κ' of the source term S play the same role, respectively, as D_l , γ and γ' for D . Note that κ' regulates the maximum value of the biomass density through controlling the density B where S starts to tend to 0. However, the value of the parameters identified for the source term leads to a smoother function shape, which presents its peak value at around 0.15 instead of 0.01 for D . The profiles of D and S are consistent with the expansion of fungal biomass. The diffusion occurs at the marge of the colony where the biomass density is low, while the increase of the density in the

inner colony is mainly caused by the fungal growth (i.e., the source term). In addition, the normalized fungal density cannot reach 1.0 which means the filamentous hyphae cannot cover the whole domain, owing to anastomosis.

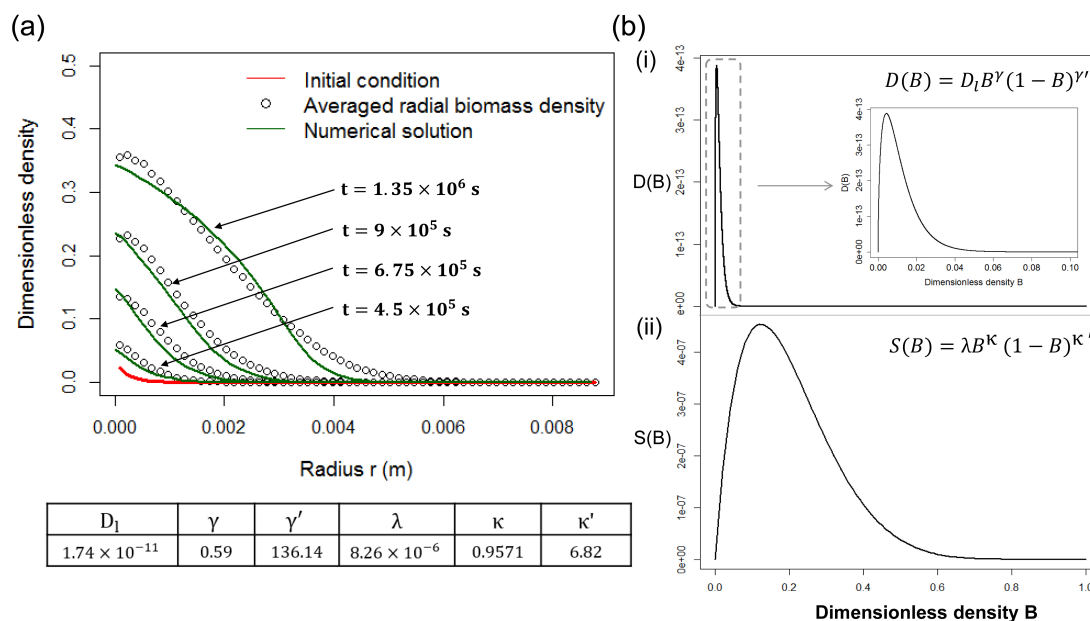


FIGURE 5.3 – Optimization result of 1D RD equation compared with the profiles of averaged density obtained from the discrete model. (a) Four optimized profiles of the numerical solution (dark green lines) calculated at $t = 4.5 \times 10^5$, 6.75×10^5 , 9×10^5 , and 1.35×10^6 s compared with the corresponding profiles obtained from the discrete model (black circle); red line is the initial condition which is the profile at $t = 4.5 \times 10^4$ s obtained from the discrete model; the inset table lists the optimized value of the six model parameters governing the diffusion coefficient and the source term. (b) Evolution of (i) the diffusion coefficient $D(B)$ and (ii) the source term $S(B)$ with the normalized biomass density B .

5.3 2D simulation of fungal growth using the continuous model

5.3.1 Comparison of fungal growth in various media

In this section, the RD continuous model is used to simulate fungal development at a larger scale, in a periodic heterogeneous medium. As shown in Fig. 5.4, the 2D simulation

was carried out in a porous medium $\Omega \in \mathbf{R}^2$ composed of two phases, pore (Ω_α) and obstacle (solid phase) (Ω_β). We assumed that the flow of fungal biomass is homogeneous and isotropic in the pore space, while no fungal biomass can grow in the solid phase. Consequently, the flux normal to their interfaces $\partial\Omega_\beta$ is equal to zero. The biomass development in the pore space is calculated according to the calibrated $D(B)$ and $S(B)$. A zero-flux external boundary condition (BC) is applied on the external boundary of the computed domain Ω (i.e., $\partial\Omega$). The 2D RD system in Cartesian coordinates can be summarized as follows :

$$\frac{\partial B(x, y, t)}{\partial t} = \nabla \cdot (D(B)\nabla B(x, y, t)) + S(B), \text{ in } \Omega_\alpha, \quad (5.5a)$$

$$\text{Internal BC } D(B)\nabla B(x, y, t) \cdot n = 0, \text{ on } \partial\Omega_\beta, \quad (5.5b)$$

$$\text{External BC } D(B)\nabla B(x, y, t) \cdot n = 0, \text{ on } \partial\Omega. \quad (5.5c)$$

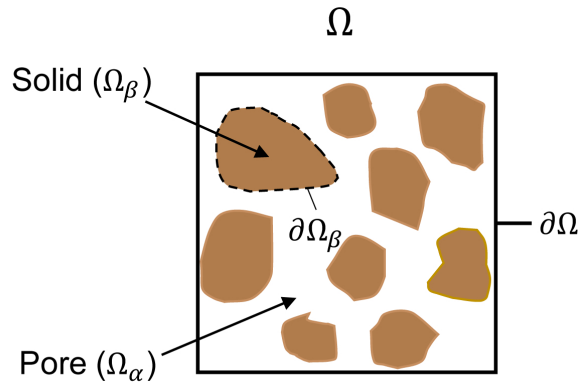


FIGURE 5.4 – General configuration of a porous medium. The whole domain (Ω) consists of two phases : pore phase (Ω_α) and solid phase (Ω_β). The interface of the two phases is denoted by $\partial\Omega_\beta$ and the boundary of Ω is $\partial\Omega$.

Two types of periodic porous media were constructed to investigate the biomass development in isotropic and anisotropic porous media. The calculation domain consists of 120×120 grid points (pts) and the resolution of the 2D grid is $1.5 \cdot 10^{-4} \times 1.5 \cdot 10^{-4} m^2$. The equivalent macroscopic medium is expected to be isotropic with respect to diffusion when the elementary periodic pattern is unchanged by a rotation of 90° . For example, in the medium illustrated in Fig. 5.5(a) (denoted by *isotropic medium*), the identical squares

are uniformly distributed in the domain and the spacing in x - and y -direction between two squares is equal to the length of the square side (i.e., 10 pts). This equivalent medium is isotropic since the diffusion in the x - and y -direction is the same (proved by Fig. 5.6). The other medium shown in Fig. 5.5(b) (denoted by *anisotropic medium*) is composed of rectangles of 30 pts long and 10 pts wide with the spacing between two adjacent rectangles of 10 pts in both x - and y -direction. The minimum offset distance (denoted by s) between the rectangles of two consecutive rows along the x -direction is 20 pts . In this case, the elementary period is not invariant by rotation.

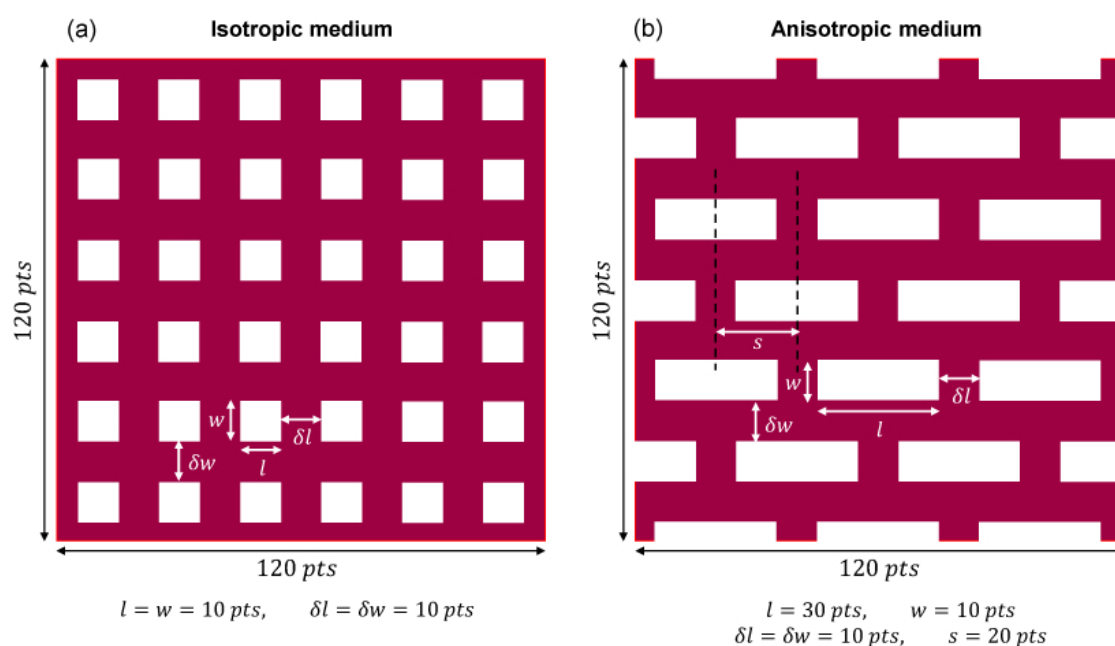


FIGURE 5.5 – Geometrical models of porous media. (a) Isotropic medium composed by aligned squares and (b) anisotropic medium composed of offset rectangles. The grid dimension is $120\text{ pts} \times 120\text{ pts}$; l and w denote respectively the length and the width of the obstacles; δl and δw are the spacing between two adjacent obstacles along x and y -direction; s represents the minimum offset distance between the two consecutive rectangle-rows along x -direction.

Eq. 5.5 was applied to calculate the biomass distribution in the homogeneous medium (no solid phase), the isotropic medium and the anisotropic medium. The 2D RD problem was solved using a 2D explicit finite volume method. The same protocol as for the 1D solution was adopted to fix the time step. The initial condition consists in applying the averaged radial biomass density of the discrete model at $t = 4.5 \times 10^4\text{ s}$ in the following way :

$$B(x, y, t) = \langle \rho \rangle (r_k, t) \quad \text{if} \quad \left(r_k - \frac{\Delta r_k}{2}\right)^2 < (x^2 + y^2) \leq \left(r_k + \frac{\Delta r_k}{2}\right)^2. \quad (5.6)$$

The fungal fields at two different times ($t = 9 \times 10^5$ s and $t = 1.8 \times 10^6$ s) are depicted in Fig. 5.6 for the three selected media via 2D contours and 3D carpet plots, which respectively emphasize the shape of the mycelium and the flow of biomass bypassing the obstacles. As expected, the mycelium in the homogeneous medium presents a round shape with the highest biomass density in the center of the colony. We observed the nonlinear decline of the biomass density from the center outward in the homogeneous medium from the 3D carpet plots. In the two porous media, the morphology of the colony changes significantly. The obstacles inhibit the flow of the biomass along the original direction and hence slow down its expansion rate. However, the diffusion and reaction processes give rise to a smooth flow of biomass bypassing the obstacles along the density gradient from the region of high density to that of low density. The maximal density in the center is not influenced by the obstacles due to the extremely low value of the diffusion coefficient when the biomass density is greater than 0.05. The fungal biomass in the isotropic medium is symmetrically distributed with respect to both x - and y -axis, which confirms an *isotropic diffusion process*. On the contrary, the expansion of biomass in the anisotropic medium is evidently faster in x -direction than in y -direction. As expected, the length of the obstacles along x -axis is efficient in limiting biomass diffusion along the y -direction.

5.3.2 Simulation of fungal growth in extended domains

The final aim of this work is to derive a macroscopic formulation able to predict the averaged field resulting from fungal development in structurally heterogeneous media. This goal needs averaged fields of sufficient extension to be obtained to identify the model parameters at the macro-scale. To achieve this goal, enlarged calculation domains, based on those in Fig. 5.5, were constructed. To limit the computational time and memory needs, heterogeneous media were constructed along one direction. The extension of the medium along the direction perpendicular to that direction is just one period wide, which is the minimum extension needed to capture the macroscopic behavior.

In the homogeneous medium and the isotropic equivalent medium, the diffusion process is the same in x - and y -directions, so that the expansion of fungal biomass along the x -axis is also representative of the y -direction. On the contrary, both x - and y -directions need to be computed for the anisotropic medium. Thus, the band domains of four studied cases were

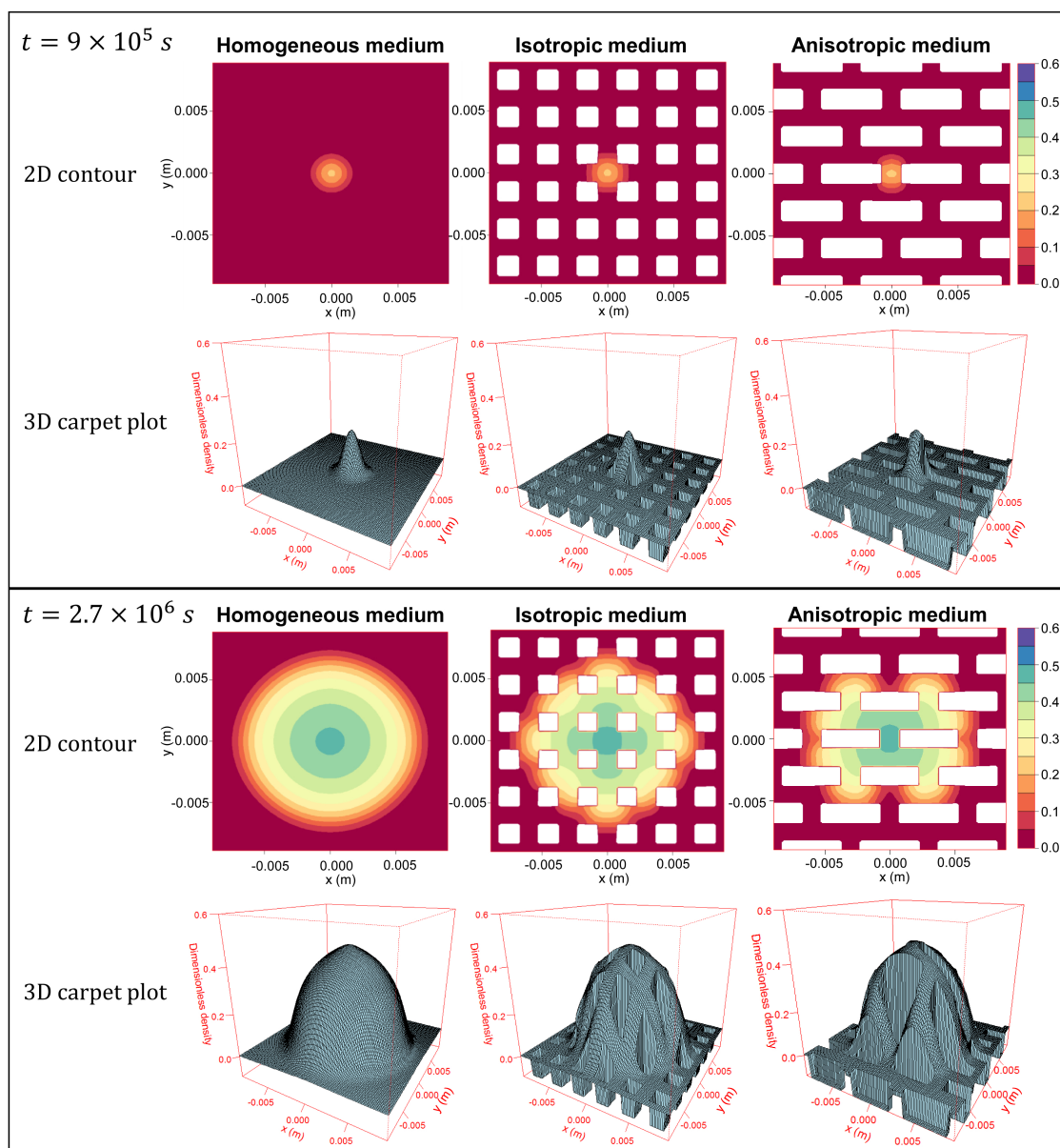


FIGURE 5.6 – 2D simulations of fungal biomass development at two selected times for various contrasted media. Color bar indicates the normalized biomass density.

considered as shown in Fig. 5.7 : (i) homogeneous medium, (ii) isotropic medium, (iii) anisotropic medium along x -direction, and (iv) anisotropic medium along y -direction. The dimensions of the first two domains are $520 \times 20 \text{ pts}$, while the last two are respectively of dimension $520 \times 40 \text{ pts}$ and $40 \times 520 \text{ pts}$. The obstacle size and the spacing between two adjacent obstacles are identical to those of Fig. 5.5. The initial conditions are consistent with a 1D problem in the following way : the normalized biomass density B is 0.05 in the

column-domain (in light red) with width of 20 pts at the mid-length of the domain and $B = 0$ for the remaining part.

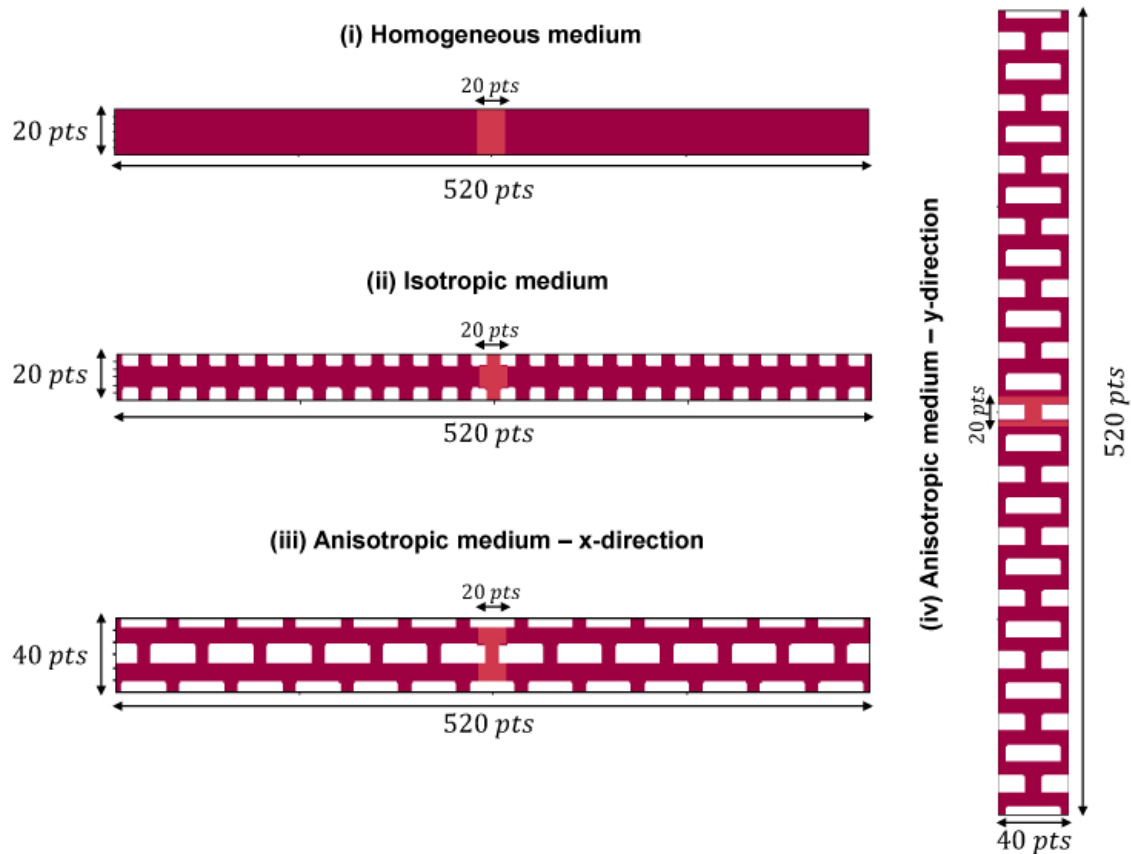


FIGURE 5.7 – Enlarged calculation domains with the initial field. The size of the obstacles and the spacing between two adjacent squares are respectively $10 \times 10 \text{ pts}$ and 10 pts in the isotropic medium, and $30 \times 10 \text{ pts}$ and 10 pts in the anisotropic medium; the initial condition in each case is that the normalized biomass density is set to 0.05 in the light red part and to 0 in the rest of the domain.

The 2D contours of the numerical solutions were plotted at two times ($t = 9 \times 10^5 \text{ s}$ and $t = 2.7 \times 10^6 \text{ s}$) for each case (Fig. 5.8). In the homogeneous medium, the isovalues of the biomass field remain vertical throughout the simulation, while the obstacles in the porous media force the isovalues to be curved for the biomass flux to navigate around the obstacles. The biomass spreads faster along the x -direction than along the y -direction in the anisotropic medium, which is consistent with the shape of the unit cell (not invariant by a rotation of 90°).

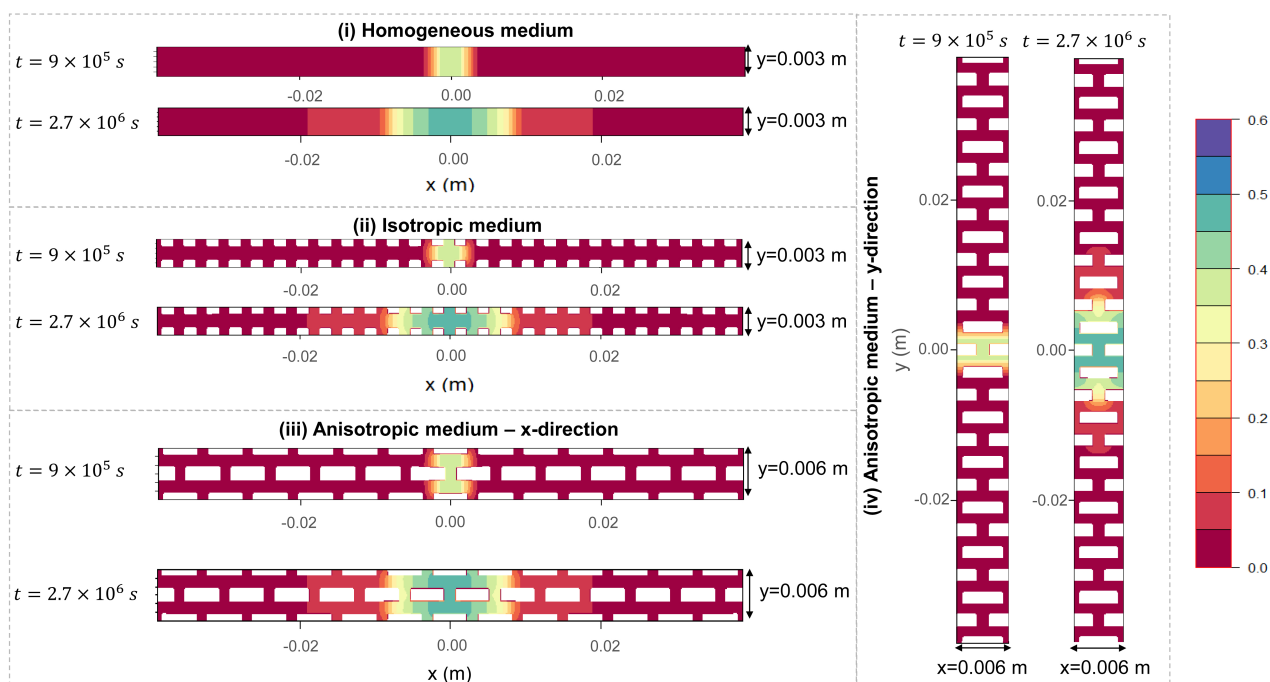


FIGURE 5.8 – 2D solutions computed for the extended calculation domains at two different times. Color bar represents the normalized biomass density.

5.4 Deriving the macroscale model

When the size of the obstacles Ω_β is much smaller than the whole domain Ω , the scale of the heterogeneity is small enough for the behavior of the porous medium to be homogenized by volume averaging. The objective of this last section is to derive a macroscopic formulation, valid on an effective homogeneous medium, whose solution is able to reproduce the local field averaged over the unit cell.

5.4.1 Spatial averaging of the local fields

As the extended domains were designed to obtain 1D macroscopic fields, these domains were simply averaged along the x -axis using a sliding window whose dimensions are those of the unit periodic cell. The width of the unit cell (extension along the main domain direction) was therefore equal to 20 pts which guarantees a uniform porosity ($\epsilon = 0.75$ for the isotropic medium and $\epsilon = 0.625$ for the anisotropic medium) whatever the position of the cell. While calculating the column density, we used global averaging, hence the

pore phase and solid phase volumes were both considered [122]. This method was used to calculate the macroscopic field, denote by $\phi(x, t)$, from the simulated local-scale fields at four different times : $t'_1 = 4.5 \times 10^5$, $t'_2 = 9 \times 10^5$, $t'_3 = 1.8 \times 10^6$ and $t'_4 = 2.7 \times 10^6$ s (Fig. 5.8).

The averaged fields for the four cases and the four times are plotted in Fig. 5.9. The time evolution of these profiles is quite similar. Consistently, profiles of case (i), a medium without a solid phase, has the higher field value and a slightly larger extension. On the contrary, case (iv) depicts narrower profiles. This trend is especially obvious at 2.7×10^6 s. Note the difference of width between profiles (iii) and (iv) (the same medium but for two orthogonal diffusion directions) : this emergent macroscopic anisotropy, obtained with two isotropic local phases (pore- and solid-phase), is then due to the spatial arrangement of the phases.

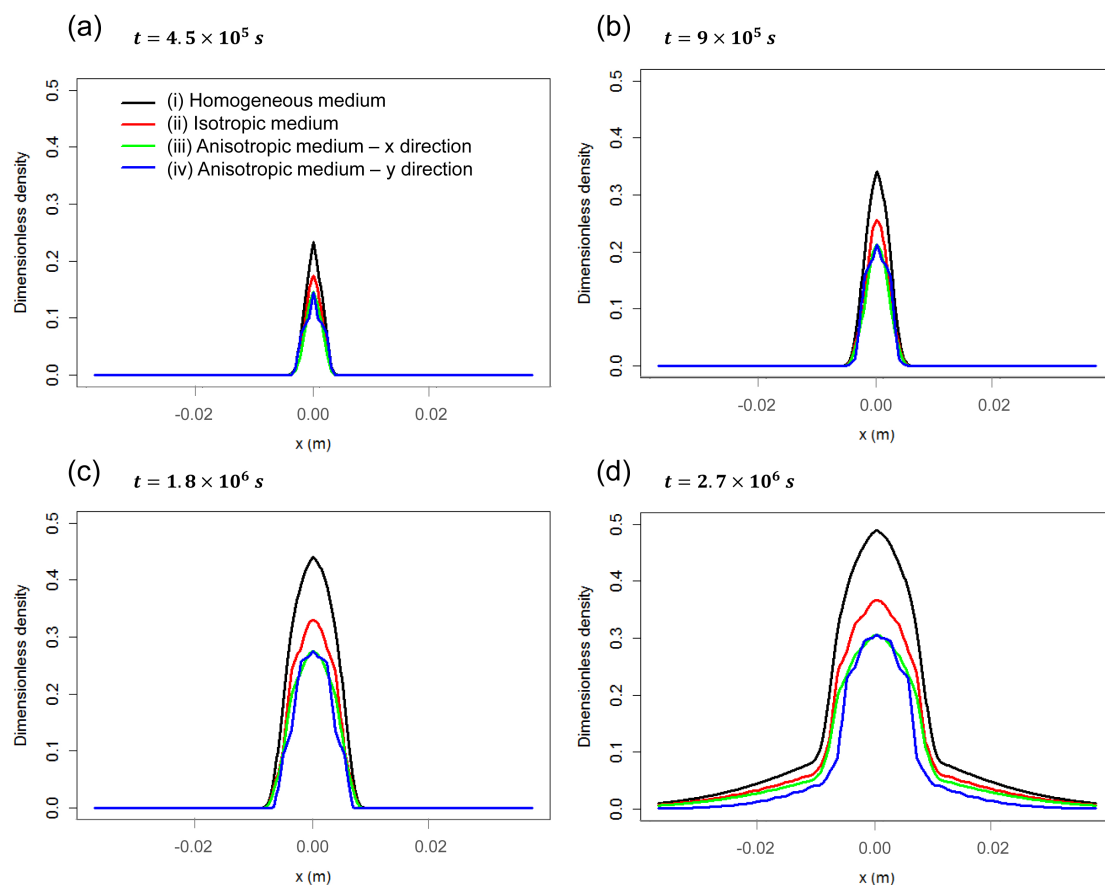


FIGURE 5.9 – Profiles of the column density calculated from the simulations in extended calculation domains.

5.4.2 Identification of the macroscale model

Unsurprisingly, a RD model is proposed at the macro-scale. The same mathematical expressions were also used to obtain the diffusion coefficient and the source term as a function of the biomass density. The identification procedure therefore involves a 1D RD solution (Eq. 5.7) in Cartesian coordinates with macroscopic variables : averaged fungal biomass density $\langle B \rangle$, macroscopic diffusion coefficient $\langle D \rangle$ and macroscopic source term $\langle S \rangle$. Hence, six parameters D_m , γ_m , γ'_m , λ_m , κ_m and κ'_m have to be adjusted by inverse analysis. The procedure is performed to determine the equivalent macroscopic forms of $\langle D \rangle$ and $\langle S \rangle$. The objective was to determine the equivalent macroscopic $\langle D \rangle$ and $\langle S \rangle$ for the three cases of the porous media, case (ii), (iii) and (iv). The BCs and initial conditions are assumed to be the same as for the local-scale model. For the initial conditions, we assigned $\langle B \rangle = 0.05 \times \epsilon$ to the 20 *pts* in the middle of the calculation domain and $\langle B \rangle = 0$ for the rest of the domain. The grid spacing and the time stepping are the same as the local-scale model (i.e., $\delta = 1.5 \times 10^{-4} m$ and $\tau = 100 s$).

$$\begin{aligned} \frac{\partial \langle B \rangle (x, t)}{\partial t} &= \nabla \cdot (\langle D \rangle (\langle B \rangle) \nabla \langle B \rangle (x, t)) + \langle S \rangle (\langle B \rangle) \\ \langle D \rangle (\langle B \rangle) &= D_m \langle B \rangle^{\gamma_m} (1 - \langle B \rangle)^{\gamma'_m} \\ \langle S \rangle (\langle B \rangle) &= \lambda_m \langle B \rangle^{\kappa_m} (1 - \langle B \rangle)^{\kappa'_m} \end{aligned} \quad (5.7)$$

The objective function of the optimization problem is the MSE (Eq. 5.8) between the numerical solution $\langle B \rangle$ of the macroscale model and the profiles ϕ obtained by averaging the 2D local-scale field at four different times :

$$MSE = \frac{1}{4N} \sum_{t \in \{t'_1, \dots, t'_4\}} \sum_{k=1}^N (\phi[x(5(k-1)+1), t] - \langle B \rangle [x(5(k-1)+1), t])^2, \quad (5.8)$$

where $N = 101$ since 101 points with the same spacing (5 *pts*) were selected to calculate MSE. The optimized results are presented in Fig. 5.10 where the red line is the initial condition, the black circles are the averaged local-scale fields and the dark green line depicts the solution of the macroscale model. The macroscopic profiles are in very good agreement with the averaged local-scale fields, leading to very low values of $MSE = 4 \times 10^{-5}$, 3×10^{-5} and 6×10^{-5} respectively for the three cases (ii)-(iv). The parameters of the macroscale model are listed in Table 5.1 and the corresponding functions $\langle D \rangle$ and $\langle S \rangle$ for the three cases are plotted in Fig. 5.11. In the case of the homogeneous medium, the macroscopic parameters are equal to those of the local-scale model : this uses to be

expected and simply allows the strategy adopted for initial, boundary conditions and volume averaging to be validated. The obvious difference between the shape of the diffusion coefficient in case (iv) compared to the other cases denotes a difference in biomass development due to the larger tortuosity imposed by the solid phase pattern. As a consequence, the diffusivity is much smaller at very low values of density, when the source term is still small. On the contrary, the diffusivity remains large up to larger values of density, up to 0.25 against 0.05, to compensate. Diffusion then starts later, when the source term has already produced a sufficient amount of biomass.

It is also interesting to notice that the densities at which the source term starts to tend to zero (i.e., the maximum density ($\langle B \rangle_{max}$) to be reached) in the case (ii)-(iv) are approximately the product of the porosity ($\epsilon = 0.75$ for case (ii) and $\epsilon = 0.625$ for case (iii) and (iv)) and $\langle B \rangle_{max}$ in the homogeneous medium. Note that the higher peak of the source term in case (iv) compared to case (iii) compensates the greater diffusion around $\langle B \rangle = 0.1$ to obtain the similar maximum density at $x = 0$.

TABLE 5.1 – Parameter values of the macroscale model.

	D_m	γ_m	γ'_m	λ_m	κ_m	κ'_m
Isotropic medium	8.71×10^{-12}	0.48	94.44	6.84×10^{-6}	0.9506	9.34
Anisotropic medium along <i>x</i>-direction	5.06×10^{-12}	0.41	61.33	6.99×10^{-6}	0.9521	11.89
Anisotropic medium along <i>y</i>-direction	8.69×10^{-12}	0.81	16.65	8.98×10^{-6}	0.9606	12.96

5.5 Conclusion

In this work, two successive upscaling steps were performed to propose a macroscale model able to simulate the spatial expansion of the biomass of *Postia placenta* in a porous medium. The first step used the results of a discrete model to obtain averaged radial profiles of biomass at different times. This discrete model uses a new algorithm to mimic the development of mycelium (tip elongation, lateral and apical branching, anastomosis) as measured in conditions of free growth. A continuous model, based on a reaction-diffusion equation, was successfully identified by inverse analysis to reproduce the radial profiles

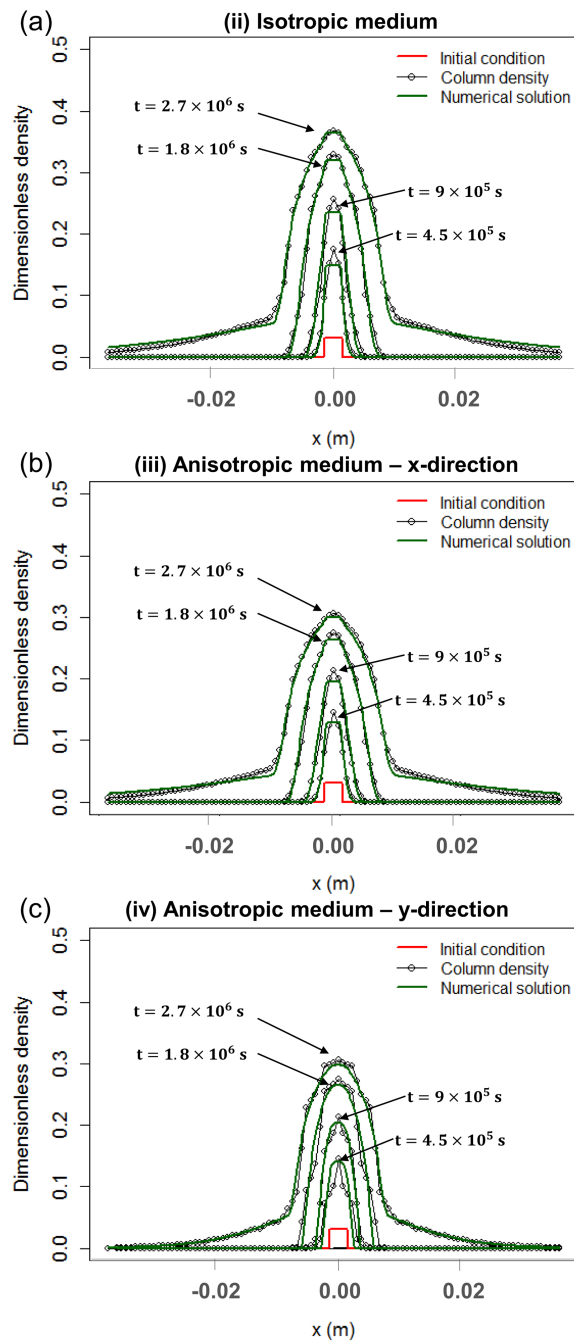


FIGURE 5.10 – Optimized results of the macroscale model compared with the averaged microscopic fields. (a) Isotropic medium, (b) anisotropic medium along x -direction and (c) anisotropic medium along y -direction.

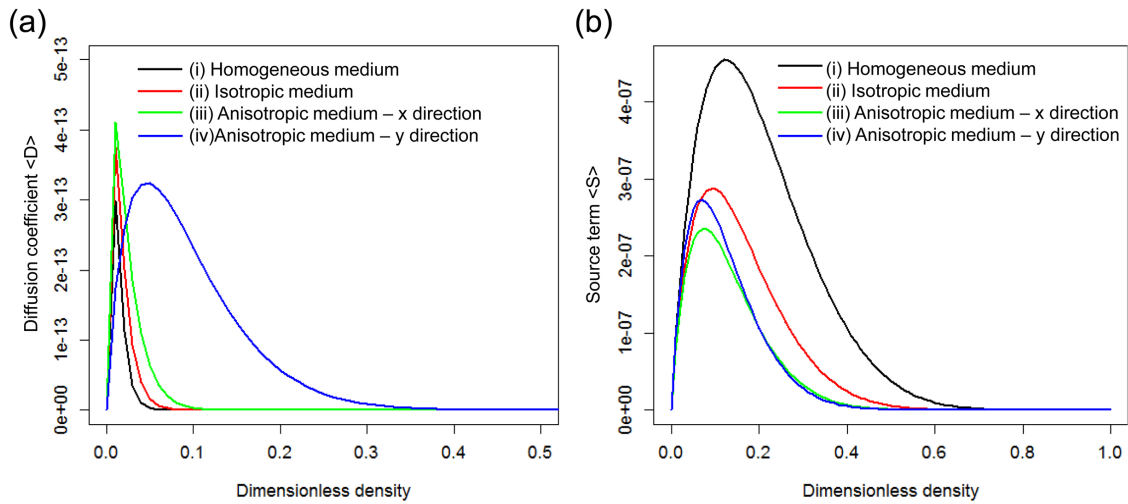


FIGURE 5.11 – Evolution of the macroscopic variables $\langle D \rangle$ and $\langle S \rangle$ with $\langle B \rangle$ for different media.

obtained with the discrete model.

It is interesting to note that the two model parameters, the diffusivity and the source term, are stiff non-linear functions of biomass density. The function shapes obtained for D and S are consistent with the strategy of fungal development : the diffusion occurs at the marge of the colony where the biomass density is low, while the density increase inside the colony is ensured by the source term. This source term tends towards zero before a normalized fungal density of 1.0, which is consistent because anastomosis prevents the filamentous hyphae to cover the whole domain.

This continuous model was then used to simulate fungal development in 2D periodic porous media with different solid phase patterns. The local-scale fields obtained on these media were then averaged to produce macroscopic fields used to derive an equivalent macroscale model for each pattern of the solid phase. Our results prove that a reaction-diffusion model works very nicely for the macroscale model. The function obtained for the diffusivity and the source term are affected by the porosity (part of the medium accessible to fungi) and to the pattern of the solid phase : for example, an anisotropic behavior emerges from a solid phase pattern which is not invariant by rotation.

Chapter6

Conclusion and perspectives

Using experimental and modeling tools, the spatial growth of the brown rot fungus *Postia placenta* in a complex environment at both local- and macro-scale was investigated. This work includes three successive and complementary parts : (i) the experimental observation of mycelial morphology in homogeneous media at the local scale, (ii) the discrete model of mycelial network development at the local scale, and (iii) the continuous model of the expansion of fungal biomass in porous media at the macro-scale. The experimental observation provided the growth parameters of the discrete model and then the continuous model was derived from the results of the validated discrete model. In this way, the equivalent macroscale properties of fungal growth in porous media were determined step by step from the small-scale properties of hyphal growth. The three main parts of the work and possible future work are summarized below.

Experimental observation

The temporal evolution of the whole colony of *Postia placenta* was visualized using a confocal laser scanning microscope whose resolution enables the behaviors of individual hyphae to be observed. The 3D constructions and 2D projections of each observation were obtained for the determination of different growth parameters. As a direct result of the imaging of a large field covering the whole colony with a high resolution, the change of the fungal biomass at the colony level and the growth characteristics at the hyphal level could be both quantified and analyzed. The morphological characterization of the mycelium, including the tip extension rate, the branch angle and the segment length distribution, was quantitatively measured and represented by mathematical expressions with

full sets of identified parameters. The tip extension rate was measured and determined for the whole colony, while the calculation of the branching parameters was carried out in three radial regions which represent the different duration of the colony development. The results indicate that the branch angle distribution, which was well fitted using a Gaussian distribution, did not change with the age of the region, or with branching types (apical or lateral). On the contrary, the segment length distribution, which represented the branch density and was fitted by gamma distributions, varied with the age of the region. The main hyphal growth parameters of *Postia placenta* are, for the first time, systematically quantified via imaging technique as well as the spatial biomass distribution of the whole colony. These experimental results were used to validate our discrete model.

Discrete model

In this part, a discrete lattice-based model was derived to mimic the evolution of the mycelial network with time in incorporating the basic hyphal growth behaviors observed in the experiment and described in the literature, including hyphal elongation, branching and anastomosis. We developed a new algorithm to eliminate the geometrical restriction of the regular lattice on the morphology of the mycelia and gain the computational efficiency at the same time owing to the discrete transition rules and discrete orientations for tips. Furthermore, the tropism and obstacle mechanisms highlight that the model possesses the potential to reproduce the different possible strategies of mycelial growth in complex environments. In particular, the thigmotropism allows the hyphae to navigate around the obstacles, which provides a base for simulating hyphal growth in bio-based materials. This model has been calibrated and validated via a rigorous procedure using the experimental results. Some of the modeling parameters were obtained directly from experimental data, while others were determined by inverse analysis (in comparing the simulated results to the experimental ones). With these validated parameters, both the mycelial spatial invasion and the small-scale behaviors of hyphae are reproduced simultaneously.

Continuous model

In order to simulate the spatial development of *Postia placenta* in porous media at the macro-scale, a continuous model was derived by two successive upscaling steps from the

results of the validated discrete model. Firstly, an equivalent reaction-diffusion equation was identified by inverse analysis to reproduce the radial biomass density of the mycelial network obtained from the discrete model. Highly nonlinear expressions were obtained for the diffusivity and the source term, which is consistent with the strategy of fungal development : the diffusion occurs at the marge of the colony where the biomass density is low, while the density increase inside the colony is regulated by the source term. Secondly, this continuous formulation was used to simulate the fungal growth in a 2D periodic porous medium, by assuming normal growth in the pore phase and no fungal growth in the solid phase. By averaging the local fields over one periodic unit cell, the macroscopic biomass field was obtained and was successfully used to derive an equivalent macroscale model for each porous medium. The identified functions for the equivalent diffusivity and source term on the macroscopic field have a form similar to the local model, but their values depend on the medium porosity and the morphology of the solid phase, possibly leading to an anisotropic equivalent medium.

Perspectives

The accomplished work, which scales from the small-scale properties of hyphal growth to the macroscale spread of fungal biomass in periodic heterogeneous media, is a solid base for modeling fungal decay in bio-based materials. However, due to the complex decay dynamics of fungi and their dependence on environmental factors, there is still much work to be carried out. In terms of experiments, since the woody cell walls provide nutrients for fungal growth, it would be interesting to investigate the possible different hyphal density around these cell walls and the decay patterns. In using nano-tomography (LGPM project for 2017), the local hyphal distributions and the local decay patterns in small blocks of wood samples can be observed. These experimental results would provide the necessary information to identify the decay mechanisms for our models. The 2D discrete model could be extended to a 3D model which would generate mycelial networks in real porous media to validate the decay mechanism in comparing to the observed results obtained by nano-tomography. In addition, the impact of the temperature and the moisture content on hyphal elongation and branching can also be studied to develop the relationship between the growth parameters in the models and the environmental factors. A PhD work has just started at LGPM to develop an original experimental bioreactor able to observe and measure the fungal growth in lignocellulosic products in controlled growth conditions. The experimental database collected by this project will be specially designed to feed the

reaction-diffusion model at various growth conditions.

For the continuous model, the complexity of the nonlinear diffusion coefficient and source term leads to the difficulty in analyzing and extracting the change rules of them related to the fungal expansion in complex porous media. Due to the fractal nature of mycelial colonies of *Postia placenta*, a fractional formulation, either in space or in time or both, is certainly a promising approach to derive a continuous model from either observations or discrete simulations. The leading idea is to simplify the bridge between the fungal strategy (elongation rate, branching probabilities) and the parameter values of the continuous formulation. A collaboration with the School of Mathematical Sciences, QUT, Brisbane, Australia, will start on this possibility just after the PhD defense.

Annex

Résumé

Les matériaux d'origine végétale sont largement utilisés dans l'industrie de la construction en raison de leurs excellentes propriétés structurels et thermiques. Cependant, l'utilisation de ces matériaux dans les bâtiments pose la question de la pérennité des ouvrages principalement à cause de la dégradation fongique. *Postia placenta* est une espèce de champignon provoquant la pourriture brune qui est la plus destructrice pour les constructions et structures en bois en raison de son mécanisme rapide de dégradation. A cet effet, cette espèce rencontre une grande attention dans les domaines de la recherche mycologique et sur les matériaux bio-sourcés.

Ce travail de thèse porte sur l'observation et la modélisation de la croissance de *Postia placenta* à trois échelles successives : l'arborescence du mycélium (échelle discrète), la croissance en milieu libre (échelle continue) et la croissance en milieu encombré (échelle macroscopique). L'observation expérimentale de la croissance de *Postia placenta* se fait via un microscope confocal à balayage laser. Une série d'images de l'évolution temporelle de la morphologie d'un mycélium a été obtenue à l'aide d'un fluorochrome vital pendant dix-sept jours. Ces images ont permis de mesurer la croissance de la biomasse via une méthode de voxels pour obtenir les trois phases de croissance (phase de latence, exponentielle et stationnaire). De plus, les différents mécanismes ont été quantifiés pour obtenir les paramètres de croissance fongique. Les distributions de vitesse de prolongement des tips (i.e., apex des hyphes), d'angle de branchaison et de longueur de segment entre deux sites adjacents de branchaison et/ou d'anastomose ont été mesurées et calculées. L'analyse statistique révèle que la vitesse des tips est répartie aléatoirement dans l'espace. La distribution d'angle de branchaison n'évolue pas avec le développement de la colonie, cependant, la densification du mycélium augmente avec le temps.

A partir de cette observation, un modèle discret sur lattice capable de reproduire les trois mécanismes fongiques, y compris l'élongation des hyphes, la branchaison et l'anastomose, a été imaginé et implémenté. L'originalité du travail repose sur l'élaboration d'un

nouvel algorithme sur l'extension du tip, qui permet d'éliminer la restriction géométrique de la lattice sur la forme du mycélium. Grâce à cette originalité, le modèle est capable de générer un mycélium dont la morphologie est extrêmement similaire à celle observée. De plus, en ajoutant des tropismes, ce modèle permet aussi de simuler le développement du mycélium dans différents environnements, notamment le thigmotropisme qui permet aux hyphes de contourner les obstacles. Ceci ouvre la possibilité de simuler la croissance du mycélium dans des milieux poreux, notamment les isolants à base de fibres naturelles. Un processus rigoureux de validation du modèle a été effectué. Certains paramètres ont été directement alimentés par ceux-ci de croissance obtenus grâce à l'expérimentation, tandis que les autres ont dû être déterminés par méthode inverse. Les paramètres étant définis, le modèle est capable de reproduire le couplage complexe entre l'extension spatiale de biomasse et la densification du réseau fongique. Avec le modèle discret, divers profils de biomasse ont été obtenus à différents instants à l'échelle continue par prise de moyenne selon le rayon des mycéliums simulés dans un milieu homogène. Un modèle continu basé sur une équation de réaction-diffusion permet de décrire l'évolution de la densité de biomasse fongique. Le coefficient de diffusion D et le terme source S ont été déterminés par identification en confrontant les profils calculés par ce modèle continu à ceux obtenus par le modèle discret. Ces deux paramètres, D et S , sont fortement non linéaires en raison de la stratégie de développement fongique : la diffusion ne se produit qu'à la marge de la colonie où la densité de biomasse est faible, alors que la croissance de la biomasse à l'intérieur liée à la branchaison est assurée par le terme de source.

Ce modèle continu offre la possibilité de la transition de l'échelle de la colonie vers l'échelle macroscopique. Pour cela, des simulations de la prolifération en environnement encombré ont été obtenues à l'aide du modèle continu. Deux types de milieux hétérogènes (phases poreuse et solide) ont été étudiés : (i) milieu isotrope équivalent construit par des obstacles carrés et (ii) milieu anisotrope construit par des obstacles rectangulaires. Les champs macroscopiques, obtenus par prise de moyenne des champs locaux sur une cellule unitaire périodique, permettent de déterminer les paramètres d'un modèle continu similaire, mais valable à l'échelle macroscopique. Les paramètres macroscopiques dépendent de la porosité et de la morphologie de la phase solide. De cette manière, les propriétés macroscopiques équivalentes de la croissance fongique dans des milieux poreux ont été déterminées étape par étape à partir des caractéristiques de la croissance des hyphes à petite échelle.

Bibliographie

- [1] R Sinha, M Lennartsson, and B Frostell. Environmental footprint assessment of building structures : a comparative study. *Build. Environ.*, 104 :162–171, 2016.
- [2] L Gustavsson and R Sathre. Variability in energy and carbon dioxide balances of wood and concrete building materials. *Build. Environ.*, 41(7) :940–951, 2006.
- [3] B Wedvik, M Stein, JM Stornes, and J Mattsson. On-site radioscopic qualitative assessment of historic timber structures : identification and mapping of biological deterioration of wood. *Int. J. Archit. Herit.*, 3058(August) :150820110921004, 2015.
- [4] O Schmidt. *Wood and Tree Fungi*. Springer Verlag Berlin Heidelberg, 2005.
- [5] Y Kobayashi, N Iida, Y Imamura, and U Watanabe. Drying and anatomical characteristics of sugi wood attacked by bacteria during pond storage. *J. Wood Sci.*, 44(6) :432–437, 1998.
- [6] SL Quales. Wood decay. http://ucanr.edu/sites/Wildfire/Appendixes/Appendix_F-_Wood_decay/, 2017.
- [7] D Taylor. Fungi : rotting civilisation from its very foundations. <http://davescienceblog.blogspot.fr/2012/03/fungi-rotting-civilisation-from-its.html>, March 2012.
- [8] AM Turing. The chemical basis of morphogenesis. *Philos. Trans. R. Soc. London*, 237(641) :37–72, 1952.
- [9] CEN/TS 15083-1. Durabilité du bois et des matériaux dérivés du bois - Détermination de la durabilité naturelle du bois massif vis-à-vis des champignons lignivores - Méthodes d’essai - Partie 1 : basidiomycètes, 2006.
- [10] P Koch. *Wood decay in Danish buildings*. International Research Group on Wood Preservation, 1985.
- [11] H Viitanen and AC Ritschkoff. *Brown rot decay in wooden constructions : effect of temperature, humidity and moisture*. Institutionen för Virkeslära. Swedish

- University of Agricultural Sciences, Department of Forest Products, 1991.
- [12] WW Wilco and M Dietz. Fungi causing above-ground wood decay in structures in California. *Wood fiber Sci.*, 29(3) :291–298, 1997.
- [13] D Martinez, J Challacombe, I Morgenstern, D Hibbett, M Schmoll, CP Kubicek, P Ferreira, FJ Ruiz-Duenas, AT Martinez, P Kersten, KE Hammel, A Vanden Wymelenberg, J Gaskell, E Lindquist, G Sabat, SS Bondurant, LF Larrondo, P Canessa, R Vicuna, J Yadav, H Doddapaneni, V Subramanian, AG Pisabarro, JL Lavín, JA Oguiza, E Master, B Henrissat, PM Coutinho, P Harris, JK Magnusson, SE Baker, K Bruno, W Kenealy, PJ Hoegger, U Kües, P Ramaiya, S Lucas, A Salamov, H Shapiro, H Tu, CL Chee, M Misra, G Xie, S Teter, D Yaver, T James, M Mokrejs, M Pospisek, IV Grigoriev, T Brettin, D Rokhsar, R Berka, and D Cullen. Genome, transcriptome, and secretome analysis of wood decay fungus *Postia placenta* supports unique mechanisms of lignocellulose conversion. *Proc. Natl. Acad. Sci. U. S. A.*, 106(6) :1954–1959, 2009.
- [14] Y Xie, J Bjurman, and L Wadsö. Microcalorimetric characterization of the recovery of a brown-rot fungus after exposures to high and low temperature, oxygen depletion, and drying. *Holzforschung*, 51(3) :201–206, 1997.
- [15] JM Gonzalez and JJ Morrell. Effects of environmental factors on decay rates of selected white- and brown-rot fungi. *Wood Fiber Sci.*, 44(4) :343–356, 2012.
- [16] L Wadsö, S Johansson, A Pilgård, and G Alfredsen. The activity of rot fungi (*Postia placenta*) during drying and rewetting cycles measured by isothermal calorimetry. *Eng. Life Sci.*, 13(6) :536–540, 2013.
- [17] Keller R. *Cours de DEA Sciences du Bois : structure, composition, formation du bois*. PhD thesis, ENGREF, 1999.
- [18] RL Gilbertson. Wood-rotting fungi of North America. *Mycologia*, 72(1) :1–49, 1980.
- [19] S Carlquist. *Comparative Wood Anatomy. Systematic, Ecological, and Evolutionary Aspects of Dicotyledon Wood*. Springer, Heidelberg, 1988.
- [20] J Fahlén. *The cell wall ultrastructure of wood fibres - effects of the chemical pulp fibre line*. PhD thesis, Royal Institute of Technology (KTH), 2005.
- [21] J Brändström. Micro- and ultrastructural aspects of Norway spruce tracheids : a review. *IAWA J.*, 22(4) :333–353, 2001.
- [22] FWMR Schwarze. Wood decay under the microscope. *Fungal Biol. Rev.*, 21(4) :133–170, 2007.

- [23] J Brändström, SL Bardage, G Daniel, and T Nilsson. The structural organisation of the S1 cell wall layer of Norway spruce tracheids. *IAWA J.*, 24(1) :27–40, 2003.
- [24] H Abe and R Funada. Review - The orientation of cellulose microfibrils in the cell walls of tracheids in Conifers. *IAWA J.*, 26(2) :161–174, 2005.
- [25] SD Harris. Hyphal morphogenesis : an evolutionary perspective. *Fungal Biol.*, 115(6) :475–484, 2011.
- [26] GW Gooday. The dynamics of hyphal growth. *Mycol. Res.*, 99(4) :385–394, 1995.
- [27] SD Harris, ND Read, RW Roberson, B Shaw, S Seiler, M Plamann, and M Momany. Polarisome meets Spitzenkörper : microscopy, genetics, and genomics converge. *Society*, 4(2) :225–229, 2005.
- [28] SD Harris. Branching of fungal hyphae : regulation, mechanisms and comparison with other branching systems. *Mycologia*, 100(December) :823–832, 2008.
- [29] NL Glass, C Rasmussen, MG Roca, and ND Read. Hyphal homing, fusion and mycelial interconnectedness. *Trends Microbiol.*, 12(3) :135–141, 2004.
- [30] ADM Rayner. Interconnectedness and individualism in fungal mycelia. In BC Sutton, editor, *A Century of Mycology*, pages 193–232. Cambridge University Press, 1996.
- [31] F Kollmann and WA Cote. Principles of wood science and technology. *Springer Verlag*, d :185–186, 1968.
- [32] A Brand, S Shanks, VMS Duncan, M Yang, K Mackenzie, and NAR Gow. Hyphal orientation of *Candida albicans* is regulated by a calcium-dependent mechanism. *Curr. Biol.*, 17(4) :347–352, 2007.
- [33] T Crombie, NA Gow, and GW Gooday. Influence of applied electrical fields on yeast and hyphal growth of *Candida albicans*. *J. Gen. Microbiol.*, 136(2) :311–7, 1990.
- [34] HJ Watts, AA Véry, TH Perera, JM Davies, and NA Gow. Thigmotropism and stretch-activated channels in the pathogenic fungus *Candida albicans*. *Microbiology*, 144(Pt 3) :689–695, 1998.
- [35] J Dighton. *Fungi in Ecosystem Processes*. Marcel Dekker, Inc., New York, NY, USA, 2003.
- [36] H Viitanen. Factors affecting mould growth on kiln dried wood. In *Proceedings of COST E15 Conference*, pages 1–8, 2001.
- [37] PG Ayres and L Boddy. *Water, Fungi and Plants*. Cambridge University Press, 1 edition, 2011.

- [38] V Hintikka. The colonization of litter and wood by basidiomycetes in Finnish forests. In JC Frankland, JN Hedger, and MJ Swift, editors, *Decomposer basidiomycetes*, pages 227–239. Cambridge University Press, 1982.
- [39] L Reinprecht. *Wood deterioration, protection and maintenance*. John Wiley & Sons, Ltd, Oxford, United Kingdom, 2016.
- [40] FWMR Schwarze. Forest Pathology : Heart rot and Wood Decay. In J Burley, J Evans, and J Youngquist, editors, *Encyclopedia Forest Sci.*, pages 808–816. Elsevier Science, 2004.
- [41] FWMR Schwarze, C Mattheck, and J Engels. *Fungal strategies of wood decay in trees*. Springer, Heidelberg, Schwarze2004a, 2004.
- [42] KEL Eriksson, RA Blanchette, and P Ander. *Microbial and Enzymatic Degradation of Wood and Wood Components*. Springer Berlin Heidelberg, 1990.
- [43] MJ Fuhr. *Modeling the growth and impact of the wood-decay fungus *Physisporinus vitreus**. PhD thesis, Swiss Federal Institute of Technology in Zurich (ETH Zurich), 2012.
- [44] KJ Czymmek, JH Whallon, and KL Klomparens. Confocal microscopy in mycological research. *Exp. Mycol.*, 18(4) :275–293, 1994.
- [45] PS Maddox, B Moree, JC Canman, ED Salmon, and JR Swedlow. Spinning disk confocal microscope system for rapid high-resolution, multimode, fluorescence speckle microscopy and green fluorescent protein imaging in living cells. In Greenfield Sluder and David E Wolf, editors, *Digit. Microsc.*, volume 114 of *Methods in Enzymology*, pages 597–617. Academic Press, 2013.
- [46] JA Feijó and N Moreno. Imaging plant cells by two-photon excitation. *Protoplasma*, 223(1) :1–32, 2004.
- [47] S Refshauge, M Watt, ME McCully, and CX Huang. Frozen in time : a new method using cryo-scanning electron microscopy to visualize root-fungal interactions. *New Phytol.*, 172(2) :369–374, 2006.
- [48] NM Jaafar, PL Clode, and LK Abbott. Microscopy observations of habitable space in biochar for colonization by fungal hyphae from soil. *J. Integr. Agric.*, 13(3) :483–490, 2014.
- [49] M Minsky. Memoir on inventing the confocal scanning microscope. *Scanning*, 10(4) :128–138, 1988.
- [50] Pf Schweiger, H Rouhier, and B Söderström. Visualisation of ectomycorrhizal rhizomorph structure using laser scanning confocal microscopy. *Mycol. Res.*,

- 106(March) :349–354, 2002.
- [51] PC Hickey, SR Swift, MG Roca, and ND Read. Live-cell imaging of filamentous fungi using vital fluorescent dyes and confocal microscopy. *Methods Microbiol.*, 34(March 2015) :63–87, 2004.
- [52] J Dijksterhuis. Confocal microscopy of Spitzenkörper dynamics during growth and differentiation of rust fungi. *Protoplasma*, 222(1-2) :53–59, 2003.
- [53] S Fischer-Parton, RM Parton, PC Hickey, J Dijksterhuis, HA Atkinson, and ND Read. Confocal microscopy of FM4-64 as a tool for analysing endocytosis and vesicle trafficking in living fungal hyphae. *J. Microsc.*, 198(3) :246–259, 2000.
- [54] PC Hickey, DJ Jacobson, ND Read, and NL Glass. Live-cell imaging of vegetative hyphal fusion in *Neurospora crassa*. *Fungal Genet. Biol.*, 37(1) :109–119, 2002.
- [55] RR Mouriño-Pérez, RW Roberson, and S Bartnicki-García. Microtubule dynamics and organization during hyphal growth and branching in *Neurospora crassa*. *Fungal Genet. Biol.*, 43(6) :389–400, 2006.
- [56] DL Delgado-Álvarez, OA Callejas-Negrete, N Gómez, M Freitag, RW Roberson, LG Smith, and RR Mouriño-Pérez. Visualization of F-actin localization and dynamics with live cell markers in *Neurospora crassa*. *Fungal Genet. Biol.*, 47(7) :573–586, 2010.
- [57] M Schubert, C Stührk, MJ Fuhr, and FWMR Schwarze. Imaging hyphal growth of *Physisporinus vitreus* in Norway spruce wood by means of confocal laser scanning microscopy (CLSM). *Holzforschung*, 68(6) :727–730, 2014.
- [58] S Dickson and P Kolesik. Visualisation of mycorrhizal fungal structures and quantification of their surface area and volume using laser scanning confocal microscopy. *Mycorrhiza*, 9(4) :205–213, 1999.
- [59] H Vierheilig, M Knoblauch, K Juergensen, AJE Van Bel, FMW Grundler, and Y Piché. Imaging arbuscular mycorrhizal structures in living roots of *Nicotiana tabacum* by light, epifluorescence, and confocal laser scanning microscopy. *Can. J. Bot.*, 79(2) :231–237, 2001.
- [60] ML Smith, JN Bruhn, and JB Anderson. The fungus *Armillaria bulbosa* is among the largest and oldest living organisms. *Nature*, 356 :428–431, 1992.
- [61] G Gierz and S Bartnicki-Garcia. A three-dimensional model of fungal morphogenesis based on the vesicle supply center concept. *J. Theor. Biol.*, 208(2) :151–64, 2001.
- [62] A Goriely, G Károlyi, and M Tabor. Growth induced curve dynamics for filamen-

- tary micro-organisms. *J. Math. Biol.*, 51(3) :355–366, 2005.
- [63] A Goriely and M Tabor. Mathematical modeling of hyphal tip growth. *Fungal Biol. Rev.*, 22(2) :77–83, 2008.
- [64] GB Ermentrout and L Edelstein-Keshet. Cellular automata approaches to biological modeling. *J. theor. Biol.*, 160 :97–133, 1993.
- [65] GP Boswell, H Jacobs, K Ritz, GM Gadd, and FA Davidson. The development of fungal networks in complex environments. *Bull. Math. Biol.*, 69 :605–634, 2007.
- [66] JH Coradin, A Braun, G Viccini, LF de Lima Luz, N Krieger, and DA Mitchell. A three-dimensional discrete lattice-based system for modeling the growth of aerial hyphae of filamentous fungi on solid surfaces : a tool for investigating micro-scale phenomena in solid-state fermentation. *Biochem. Eng. J.*, 54(3) :164–171, 2011.
- [67] A Meskauskas, LJ McNulty, and D Moore. Concerted regulation of all hyphal tips generates fungal fruit body structures : experiments with computer visualizations produced by a new mathematical model of hyphal growth. *Mycol. Res.*, 108(April) :341–353, 2004.
- [68] S Hopkins and GP Boswell. Mycelial response to spatiotemporal nutrient heterogeneity : a velocity-jump mathematical model. *Fungal Ecol.*, 5(2) :124–136, 2012.
- [69] L Edelstein. The propagation of fungal colonies : a model for tissue growth, 1982.
- [70] FA Davidson. Modelling the qualitative response of fungal mycelia to heterogeneous environments. *J. Theor. Biol.*, 195(3) :281–92, 1998.
- [71] GP Boswell, H Jacobs, FA Davidson, GM Gadd, and K Ritz. Growth and function of fungal mycelia in heterogeneous environments. *Bull. Math. Biol.*, 65 :447–477, 2003.
- [72] S Parnell, F Van den Bosch, and CA Gilligan. Large-scale fungicide spray heterogeneity and the regional spread of resistant pathogen strains. *Phytopathology*, 96(5) :549–555, 2006.
- [73] S Parnell, CA Gilligan, JA Lucas, CH Bock, and F Van Den Bosch. Changes in fungicide sensitivity and relative species abundance in *Oculimacula yallundae* and *O. aciformis* populations (eyespot disease of cereals) in Western Europe. *Plant Pathol.*, 57(3) :509–517, 2008.
- [74] A Lamour, F Van den Bosch, AJ Termorshuizen, and MJ Jeger. Modelling the growth of soil-borne fungi in response to carbon and nitrogen. *IMA J Math Appl Med Biol*, 18(2) :329–346, 2000.
- [75] NJ Cunniffe and CA Gilligan. Scaling from mycelial growth to infection dyna-

- mics : a reaction diffusion approach. *Fungal Ecol.*, 1(4) :133–142, 2008.
- [76] C Brischke and S Thelandersson. Modelling the outdoor performance of wood products - A review on existing approaches. *Constr. Build. Mater.*, 66 :384–397, 2014.
- [77] A Meskauskas, MD Fricker, and D Moore. Simulating colonial growth of fungi with the Neighbour-Sensing model of hyphal growth. *Mycol. Res.*, 108(November) :1241–1256, 2004.
- [78] David MD Smith, JP Onnela, CF Lee, M Fricker, and NF Johnson. Network Automata : coupling structure and function in dynamic networks. *Adv. Complex Syst.*, 14(3) :317–339, 2011.
- [79] GP Boswell. Modelling mycelial networks in structured environments. *Mycol. Res.*, 112 :1015–1025, 2008.
- [80] D Cohen. Computer simulation of biological pattern generation processes. *Nature*, 216 :246–248, 1967.
- [81] H Yang, R King, U Reichl, and ED Gilles. Mathematical model for apical growth, septation, and branching of mycelial microorganisms. *Biotechnol. Bioeng.*, 39(1) :49–58, 1992.
- [82] H Yang, U Reichl, R King, and ED Gilles. Measurement and simulation of the morphological development of filamentous microorganisms. *Biotechnol. Bioeng.*, 39(1) :44–48, 1992.
- [83] I Carver and GP Boswell. A Lattice-Free Model Of Translocation-Induced Outgrowth In Fungal Mycelia. *IAENG Int. J. Appl. Math.*, 38(4), 2008.
- [84] MJ Fuhr, M Schubert, FWMR Schwarze, and HJ Herrmann. Modelling the hyphal growth of the wood-decay fungus *Physisporinus vitreus*. *Fungal Biol.*, 115(9) :919–932, 2011.
- [85] L Edelstein and LA Segel. Growth and metabolism in mycelial fungi. *J. Theor. Biol.*, 104(2) :187–210, 1983.
- [86] L Edelstein-Keshet and B Ermentrout. Models for branching networks in two dimensions. *SIAM J. Appl. Math.*, 49(4) :1136–1157, 1989.
- [87] FA Davidson and S Olsson. Translocation induced outgrowth of fungi in nutrient-free environments. *J. Theor. Biol.*, 205(1) :73–84, 2000.
- [88] GP Boswell, H Jacobs, FA Davidson, GM Gadd, and K Ritz. Functional consequences of nutrient translocation in mycelial fungi. *J. Theor. Biol.*, 217 :459–477, 2002.

- [89] GP Boswell. Modelling combat strategies in fungal mycelia. *J. Theor. Biol.*, 304 :226–234, 2012.
- [90] CH Wang, RH Leicester, and MN Nguyen. Decay above ground. Technical Report Manual NO. 4, CSIRO Sustainable Ecosystems, Urban Systems Program, Highett, Victoria, 2008.
- [91] C Brischke and AO Rapp. Dose-response relationships between wood moisture content, wood temperature and fungal decay determined for 23 European field test sites. *Wood Sci. Technol.*, 42 :507–518, 2008.
- [92] C Brischke and L Meyer-Veltrup. Modelling timber decay caused by brown rot fungi. *Mater. Struct.*, 49(8) :3281–3291, 2015.
- [93] H Viitanen, T Toratti, L Makkonen, R Peuhkuri, T Ojanen, L Ruokolainen, and J Räsänen. Towards modelling of decay risk of wooden materials. *Eur. J. Wood Wood Prod.*, 68 :303–313, 2010.
- [94] H Du, P Lv, M Ayouz, A Besserer, and P Perré. Morphological Characterization and Quantification of the Mycelial Growth of the Brown-Rot Fungus *Postia placenta* for Modeling Purposes. *PLoS One*, 11(9) :e0162469, 2016.
- [95] GP Boswell and FA Davidson. Modelling hyphal networks. *Fungal Biol. Rev.*, 26(1) :30–38, 2012.
- [96] H Jacobs, GP Boswell, K Ritz, FA Davidson, and GM Gadd. Solubilization of calcium phosphate as a consequence of carbon translocation by *Rhizoctonia solani*. *FEMS Microbiol Ecol.*, 40 :65–71, 2002.
- [97] LLM Heaton, E López, PK Maini, MD Fricker, and NS Jones. Growth-induced mass flows in fungal networks. *Proc. Biol. Sci.*, 277(1698) :3265–3274, 2010.
- [98] G Vidal-Diez de Ulzurrun, JM Baetens, J Van den Bulcke, C Lopez-Molina, I De Windt, and B De Baets. Automated image-based analysis of spatio-temporal fungal dynamics. *Fungal Genet. Biol.*, 84 :12–25, 2015.
- [99] SA Hutchinson, P Sharma, KR Clarke, and I MacDonald. Control of hyphal orientation in colonies of *Mucor hiemalis*. *Trans Br Mycol Soc.*, 75 :177–191, 1980.
- [100] GK Villena, T Fujikawa, S Tsuyumu, and M Gutiérrez-Correa. Structural analysis of biofilms and pellets of *Aspergillus niger* by confocal laser scanning microscopy and cryo scanning electron microscopy. *Bioresour Technol.*, 101 :1920–1926, 2010.
- [101] KW Kim, CJ Yoon, PG Kim, MB Lee, and JH Lim. Fine structure and X-ray microanalysis of silicified woods from a Tertiary basin Pohang, Korea by scanning

- electron microscopy. *Micron.*, 40 :519–525, 2009.
- [102] S Bolte, C Talbot, Y Boutte, O Catrice, ND Read, and B Satiat-Jeunemaitre. FM-dyes as experimental probes for dissecting vesicle trafficking in living plant cells. *J. Microsc.*, 214(2) :159–173, 2004.
- [103] M Freitag, PC Hickey, NB Raju, EU Selker, and ND Read. GFP as a tool to analyze the organization, dynamics and function of nuclei and microtubules in *Neurospora crassa*. *Fungal Genet. Biol.*, 41(10) :897–910, 2004.
- [104] BL Jin, TP Schultz, and DD Nicholas. Structural characterization of brown-rotted lignin. *Holzforschung*, 44(2) :133–138, 1990.
- [105] B Goodell, J Jellison, J Liu, G Daniel, A Paszczynski, F Fekete, S Krishnamurthy, L Jun, and G Xu. Low molecular weight chelators and phenolic compounds isolated from wood decay fungi and their role in the fungal biodegradation of wood. *J. Biotechnol.*, 53(2-3) :133–162, 1997.
- [106] DJ Yelle, D Wei, J Ralph, and KE Hammel. Multidimensional NMR analysis reveals truncated lignin structures in wood decayed by the brown rot basidiomycete *Postia placenta*. *Environ Microbiol.*, 13(4) :1091–1100, 2011.
- [107] HC Hoch, CD Galvani, DH Szarowski, and JN Turner. Two new fluorescent dyes applicable for visualization of fungal cell walls. *Mycologia*, 97(3) :580–588, 2005.
- [108] JW Wallis and TR Miller. Volume rendering in three-dimensional display of SPECT images. *J. Nucl. Med.*, 31(8) :1421–1428, 1990.
- [109] K Ritz and J Crawford. Quantification of the fractal nature of colonies of *Trichoderma viride*. *Mycol. Res.*, 94(8) :1138–1141, 1990.
- [110] CL Jones, GT Lonergan, and DE Mainwaring. Mycelial fragment size distribution : an analysis based on fractal geometry. *Appl. Microbiol. Biotechnol.*, 39(2) :242–249, 1993.
- [111] J Meletiadis, JFGM Meis, and JW Mouton. Analysis of growth characteristics of filamentous fungi in different nutrient media. *J. Clin. Microbiol.*, 39(2) :478–484, 2001.
- [112] K Sampson. Time series analysis demonstrates the absence of pulsatile hyphal growth. *Microbiology*, 149(11) :3111–3119, 2003.
- [113] M Nofal and K Kumaran. Biological damage function models for durability assessments of wood and wood-based products in building envelopes. *Eur. J. Wood Wood Prod.*, 69(4) :619–631, 2011.
- [114] RE Falconer, JL Bown, NA White, and JW Crawford. Biomass recycling and the

- origin of phenotype in fungal mycelia. *Proc. Biol. Sci.*, 272(July) :1727–1734, 2005.
- [115] GP Boswell and S Hopkins. Linking hyphal growth to colony dynamics : spatially explicit models of mycelia. *Fungal Ecol.*, 1(4) :143–154, 2008.
- [116] MJ Fuhr, C Stührk, M Schubert, FWMR Schwarze, and HJ Herrmann. Modeling the effect of environmental factors on the hyphal growth of the basidiomycete *Physisporinus vitreus*. *J. Basic Microbiol.*, 52 :523–530, 2012.
- [117] JM Lopez and HJ Jensen. Nonequilibrium roughening transition in a simple model of fungal growth in 1+1 dimensions. *Phys. Rev. Lett.*, 81(8) :1734–1737, 1998.
- [118] M Riquelme, CG Reynaga-Peña, G Gierz, and S Bartnicki-García. What Determines Growth Direction in Fungal Hyphae? *Fungal Genet. Biol.*, 24(1-2) :101–109, 1998.
- [119] M Riquelme and S Bartnicki-Garcia. Key differences between lateral and apical branching in hyphae of *Neurospora crassa*. *Fungal Genet. Biol.*, 41(9) :842–851, 2004.
- [120] CP Semighini and SD Harris. Regulation of apical dominance in *Aspergillus nidulans* hyphae by reactive oxygen species. *Genetics*, 179(4) :1919–1932, 2008.
- [121] M Fomina, K Ritz, and GM Gadd. Nutritional influence on the ability of fungal mycelia to penetrate toxic metal-containing domains. *Mycol. Res.*, 107(July) :861–871, 2003.
- [122] S Whitaker. *The Method of Volume Averaging*, volume 13. Springer Netherlands, 1 edition, 1999.
- [123] L Edelstein and LA Segel. Growth and metabolism in mycelial fungi. *J. Theor. Biol.*, 104(2) :187–210, 1983.
- [124] FA Davidson and AW Park. A mathematical model for fungal development in heterogeneous environments. *Appl. Math. Lett.*, 11(6) :51–56, 1998.
- [125] RE Falconer, JL Bown, NA White, and JW Crawford. Modelling interactions in fungi. *J. R. Soc. Interface*, 5(23) :603–15, 2008.

Table des figures

1.1	Fungal decay on wood in buildings.	18
1.2	Strategy of the thesis work.	20
2.1	Schematic illustration of cellular structure of wood.	25
2.2	Two major categories of wood-based construction products.	27
2.3	Demonstration of mycelium and hyphae.	28
2.4	Schematic showing micro-morphological features of different decay types.	31
2.5	Schematic of principle of CLSM	34
2.6	Examples of the investigation on hyphal growth dynamics in using CLSM with vital fluorescent dyes.	36
2.7	Examples of the 3D reconstruction of hyphae in using CLSM.	37
2.8	Difference between modeling at microscopic and colony scale.	38
2.9	Mycelial networks constructed in uniform growth conditions by Erment- trout and Edelstein-Keshet (1993) [64].	40
2.10	Simulations of mycelial growth in various environments in Boswell <i>et</i> <i>al.</i> (2003) [71].	41
2.11	The evolution of the mycelial network expanded in a soil-like environ- ment with time (Boswell (2008) [79]).	42
2.12	Examples of results simulated by Neighbor-Sensing model developed by Meskauskas <i>et al.</i> (2004,2004a) [67].	43
2.13	Example of planar growth of mycelium in Hopkins and Boswell (2012) [68].	44
2.14	Example of hyphal growth in wood simulated by the model in Fuhr <i>et</i> <i>al.</i> (2011) [84].	45
2.15	Hyphal density distributed in two different tessellations modeled by Boswell <i>et al.</i> (2003) [71]	47
2.16	Progress of fungal decay depth with time used as basic model for timber decay in Wang <i>et al.</i> (2008) [90].	48

2.17	Relationship between dose and mean decay rating fitted by field tests data in Brischke and Meyer-Veltrup(2015) [92].	49
2.18	The evolution of wood mass loss by fungal decay at different ambient air humidity conditions by Viitanen <i>et al.</i> (2010) [93].	49
2.19	1D spatial fungal growth and the probability of fungal infection modeled by Cunniffe and Gilligan (2008) [75].	50
3.1	Method of the measurement of branching characteristics.	60
3.2	Biomass growth of the whole colony as a function of days post inoculation.	62
3.3	Distribution of the extension rate ($R_p(i; x, y)$) of active tips calculated during two consecutive observations.	64
3.4	Spatial distribution of tip extension rate ($R_p(i; x, y)$) during 17 days of observations.	65
3.5	Age of region for R1, R2 and R3.	66
3.6	Distribution of branch angle measured in the observation on the 12th day.	68
3.7	Segment length distribution and the corresponding weighted cumulative distribution $F(l)$	69
3.8	Segment length distributions at different hyphal ages and their fitted curves.	70
S3.1	Schematic showing the measurement of the segment lengths.	73
S3.2	3D reconstruction of one section of the mycelium on the 12th day of observation.	74
S3.3	2D projection confocal images of <i>Postia placenta</i> obtained using the MIP method of the 3D images.	75
S3.4	Tip extension during two consecutive observations.	76
S3.5	Error of branch angle and segment length caused by z -direction growth of hyphae.	76
S3.6	Fitted curve of the tip extension rate distribution.	77
4.1	Main mechanism of hyphal growth	86
4.2	Initial field of the simulation transformed by confocal image of the first observation.	93
4.3	Local mechanism of lateral branching.	96
4.4	The 2D contour (C_2) displays the effect of (P_a, P_b^l) on the segment length distribution (12th day).	97
4.5	Normalized biomass density profiles (ρ) on the 5th and 12th day.	98

4.6	The fitted curve of observations at different ages of region and the distributions of the branching lengths.	99
4.7	Comparison of the simulated mycelial networks to the observed ones.	99
4.8	Mycelial growth in structurally heterogeneous environments.	102
4.9	Different growth strategies of mycelium in response to various environmental factors.	103
S4.1	Test of the elongation mechanism.	104
S4.2	Mycelial networks generated by two different lateral branching mechanisms.	105
5.1	Procedure of development of the continuous model.	110
5.2	Calculation of the normalized radial biomass density from the discrete model.	111
5.3	Optimization result of RD equation compared with the profiles of radial density obtained from the discrete model.	114
5.4	General configuration of a porous medium.	115
5.5	Geometrical models of porous media.	116
5.6	2D simulations of fungal biomass development at two selected times for various contrasted media.	118
5.7	Enlarged calculation domains with the initial field.	119
5.8	2D solutions computed for the extended calculation domains at two different times.	120
5.9	Profiles of the column density calculated from the simulations in extended calculation domains.	121
5.10	Optimized results of the macroscale model compared with the averaged microscopic fields.	124
5.11	Evolution of the macroscopic variables $\langle D \rangle$ and $\langle S \rangle$ with $\langle B \rangle$ for different media.	125

Liste des tableaux

1.1	Graphic summary of the thesis work.	21
2.1	Decay patterns of the three types of wood decay fungi.	32
3.1	Average tip extension rate obtained using Eq. (3.2) and relative increase of branch number per hypha during two consecutive observations.	63
3.2	Description and values of the identified parameters to be applied in the simulation of the mycelial growth.	71
4.1	Illustration of fungal growth behaviors.	83
4.2	Demonstration of the effect of the parameters on fungal growth behaviors.	87
4.3	Description and values of the modeling parameters.	100
4.4	Mathematical functions for modeling hyphal growth behaviors.	106
5.1	Parameter values of the macroscale model.	123

Titre : Observation et modélisation de la croissance de *Postia placenta* : de l'échelle discrète de la colonie à l'échelle macroscopique

Mots clés : mycélium, pourriture brune, microscope confocal, modèle discret, modèle continu, multi-échelles.

Résumé : L'utilisation de matériaux d'origine végétale dans les bâtiments thermiquement performants pose la question de la pérennité des ouvrages principalement à cause de la dégradation fongique. *Postia placenta* est une espèce des champignons provoquant la pourriture brune, qui est la plus destructrice pour les constructions en bois.

Ce travail se concentre sur l'observation et la modélisation de la croissance de *Postia placenta* à trois échelles successives : l'arborescence du mycélium (échelle discrète), la croissance en milieu libre (échelle continue) et la croissance en milieu encombré (échelle macroscopique).

L'observation expérimentale de la croissance de *Postia placenta* utilise un microscope confocal à balayage laser pour quantifier les différents mécanismes et obtenir

les paramètres de croissance. A partir de cette observation, un modèle discret capable de générer un mycélium de forme extrêmement similaire à celle observée a été imaginé, développé et validé. Ensuite, à partir des profils de biomasse moyennés selon le rayon des mycéliums simulés par le modèle discret, un modèle continu basé sur une équation de réaction-diffusion a été identifié pour décrire l'évolution de la concentration de biomasse fongique. Ce modèle continu offre la possibilité de la transition de l'échelle locale vers l'échelle macroscopique. Pour cela, des simulations de la prolifération en environnement encombré sont obtenues à l'aide du modèle continu. Par prise de moyenne, les champs spatio-temporels obtenus permettent de déterminer les paramètres d'un modèle continu similaire, mais valable à l'échelle macroscopique, sur un milieu fictif qui prend en considération la morphologie des obstacles.

Title: Observation and modeling of the growth of the wood-decay fungus *Postia placenta*: scaling from discrete mycelial networks to macroscopic fungal development

Keywords: mycelium, brown rot fungi, confocal microscopy, discrete and continuous model, multi-scale.

Abstract: The use of bio-based materials in thermally efficient buildings raises the question of the sustainability mainly due to fungal degradation. Among the wood-decay fungi, *Postia placenta* is one of the most common brown rot fungi, which are the most destructive due to their rapid decaying mechanisms.

This work focused on the experimental observation and the modeling of fungal growth at three successive scales: the mycelial network (discrete scale), mycelial growth in homogeneous media (continuous scale) and mycelial growth in porous media (macroscopic scale).

The experimental observation of the growth of *Postia placenta* was performed using confocal

laser scanning microscopy to quantify the different growth mechanisms and obtain the growth parameters. A discrete model has been derived from this observation and is capable of generating mycelial networks extremely similar to the observed ones. A continuous formulation based on a reaction diffusion equation was developed from the radial biomass density of a mycelial network obtained in the discrete model. This continuous formulation was then used to derive an equivalent macroscale model able to account for fungal development in porous media. Simulations were performed on various periodic porous media. The parameters of the macroscale model was identified on the macroscopic fields obtained by averaging the local field over one periodic unit cell.

